Ground Based Measurement of Ozone Using Stellar Spectra

A Thesis Submitted to the
College of Graduate Studies and Research
in Partial Fulfillment of the Requirements
for the degree of Master of Science
in the Department of Physics and Engineering Physics
University of Saskatchewan
Saskatoon

By

C. Reid McDonald

Permission to Use

In presenting this thesis in partial fulfilment of the requirements for a Postgraduate degree from the University of Saskatchewan, I agree that the Libraries of this University may make it freely available for inspection. I further agree that permission for copying of this thesis in any manner, in whole or in part, for scholarly purposes may be granted by the professor or professors who supervised my thesis work or, in their absence, by the Head of the Department or the Dean of the College in which my thesis work was done. It is understood that any copying or publication or use of this thesis or parts thereof for financial gain shall not be allowed without my written permission. It is also understood that due recognition shall be given to me and to the University of Saskatchewan in any scholarly use which may be made of any material in my thesis.

Requests for permission to copy or to make other use of material in this thesis in whole or part should be addressed to:

Head of the Department of Physics and Engineering Physics
116 Science Place
University of Saskatchewan
Saskatoon, Saskatchewan
Canada
S7N 5E2

Abstract

The use of stars as a radiation source for ground-based ozone remote-sensing instruments is explored and an automated prototype instrument that measures absorption due to atmospheric ozone in stellar spectra has been designed, implemented and tested.

This work represents the proof-of-concept development of a low-cost, low dispersion slitless imaging spectrometer that measures Chappuis-band absorption in stellar spectra. The work presented here progresses from the initial concept to a functional calibrated prototype that is capable of nightly automated observations of visible-band spectra from mid-magnitude stars. The design and calibration of the prototype and subsequent data collection and analysis are presented.

A slitless imaging spectrometer has been developed and integrated with a commercial self-pointing telescope and an astronomical imager. A relative intensity calibration and the development of a dynamic wavelength calibration scheme, necessitated by the slitless nature of the instrument, is presented. The calibrated prototype has been used to collect several data sets of stellar spectra, and it is shown that the instrument can detect Chappuis absorption in stellar spectra. Several issues with both the concept and design that must be addressed in further development of the prototype are identified.

Acknowledgements

I would like to express my thanks for the opportunity to study at the Institute of Space and Atmospheric Studies and the University of Saskatchewan. I am also grateful for the financial support provided by the Institute and the University of Saskatchewan, without which this work would not have been possible.

My time at the Institute has been both challenging and enjoyable. I would like to thank my fellow students in the Infrared Group for their support and advice over the years, especially Truitt Wiensz, Adam Bourassa, and Mike Stoicescu. I would also like to thank Dr. Nick Lloyd, who always answered my question with another question, for the invaluable advice and insight he provided on everything from software development to optical design. I am grateful to Wade McDonald for his assistance generating AutoCAD drawings of the spectrometer design. Machinists Perry Balon and Blair Chomyshen deserve my thanks for their advice and patience during the manufacture of the instrument. My thanks also go to Stan Shadick, the department astronomer, who enthusiastically provided technical advice and equipment that helped with the operation of the instrument.

A most heartfelt thanks to my faculty supervisors, Dr. Ted Llewellyn and Dr. Doug Degenstein. Dr. Llewellyn's support and quiet encouragement urged me onward to learn new things, and his assistance with the thesis document was invaluable and much appreciated. Dr. Degenstein's commitment to his students and dedication to science provided a refreshing and challenging learning environment. To Doug, I say thank you for inspiring me as a young engineer, for pushing me to do my best, and, most of all, for understanding when I fell short.

Finally, I extend my deepest gratitude to my family, Alfred, Charleen and Wade, for their constant encouragement and support.

To Wade McDonald, my brother.

Contents

List of Tables

List of Figures

List of Abbreviations

AU	Arbitrary Unit. Proportional to the total photons counted by the CCD.
AU/s	Arbitrary Unit per second. Proportional to the photon flux on the CCD.
CCD	Charge-coupled device.
CFC	Chloro-fluoro-carbon, an ozone-depleting compound.
DN	Digital Number.
DU	Dobson Unit.
ECMWF	European Centre for Medium range Weather Forecasting. A meteorological model.
FITS	Flexible Image Transport System. The image format adopted by the astronomical community.
FOV	Field Of View.
GOMOS	Global Ozone Monitoring by Occultation of Stars.
h	Planck's constant.
IGY	International Geophysical Year.
λ	Wavelength [Å].
Lidar	Light Detection And Ranging.
MSIS	Mass Spectrometer Incoherent Scatter. An atmospheric constituent model.
n_j	Number density of extinction species j [cm^{-3}].
seeing	Astronomical term related to the negative effects of atmospheric turbulence on imaging systems. Quantified using the Pickering Scale.
σ_j	Absorption cross-section of extinction species j [cm^2].
SZA	Stellar Zenith Angle.
$\tau(\lambda)$	Optical Depth (dimensionless) at a wavelength λ.
TOMS	Total Ozone Mapping Spectrometer.
UV	Ultraviolet.

Chapter 1

Introduction

1.1 Atmospheric Ozone

Ozone is the trace gas in the Earth's atmosphere that is responsible for the elimination of harmful ultraviolet (UV) solar radiation. Ozone, which is found mainly in the stratospheric ozone layer, has been extensively studied by atmospheric scientists since the 1930s, and a major effort to monitor global ozone columns was initiated during the International Geophysical Year (IGY) in 1957-58. The discovery of the effects of anthropogenic chemicals such as those due to chlorofluorocarbons (CFCs) and their contribution to the seasonal appearance of the "ozone hole" antarctic depletion event has led to a global reduction of CFC emissions. The measurement of ozone with ground-based, balloon-borne and satellite-based instruments continues to be a priority for both atmospheric scientists and governments worldwide as there is a need to monitor long term trends in stratospheric ozone and to characterize the effectiveness of emissions reductions.

1.2 Ground-based Instruments

Ground-based instruments were first used to study ozone in the 1930s, and continue to be the mainstay of global ozone monitoring efforts. The world-wide network of Dobson spectrophotometers established during the IGY has been augmented since that time with more advanced instruments such as the Brewer spectrophotometer and lidars. With the exception of costly lidars, the majority of ground-based ozone instruments use the sun as a radiation source, although the Brewer spectrophotome-

ter can make observations with the moon as a source.

However, solar and lunar observations are often limited at high latitudes due to the restricted daylight during the polar winter and the high zenith angles presented by the moon. Even with a lunar capability there is a need for a low-cost instrument that can provide nighttime measurements of ozone columns on a regular basis. Bright stars provide an obvious radiation source for nighttime measurements, and several attempts have been made to use stars for the purpose of ozone measurement. The line-of-sight path length through the atmosphere varies as the star rises or sets. A variation in the absorption due to atmospheric constituents is produced by the variation in path length, and this variation is used to determine the ozone column along the line of sight.

1.3 Prototype Development

The primary objective of the present work is the development of a prototype low-cost instrument that can measure ozone columns through the detection of ozone absorption in stellar spectra. The prototype is a slitless imaging spectrometer that measures the Chappuis absorption band of ozone, in the wavelength region between 5000 and 7000 Å. The development of the prototype included various aspects of instrument design. Initial specifications were used to guide the design process, and an atmospheric absorption model was developed to provide an evaluation of the observation concept. The prototype development required the design of a custom imaging prism spectrometer, which required both optical and mechanical design. A commercial self-pointing telescope and an astronomical charge-coupled device (CCD) camera were used for light collection and imaging, and custom software was developed both to automate data collection and to interface with the telescope and CCD. Preliminary testing of the prototype instrument involved both a wavelength calibration and relative intensity calibration. The calibrated instrument was used to collect several data sets and an analysis of these data was made in order to determine the effectiveness of the instrument.

1.4 Outline

A history of the study of ozone and an overview of ground-based ozone measurement techniques are presented in Chapter 2. The relevant theory and the proposed measurement scheme for the instrument are also discussed. The design of the instrument is presented in Chapter 3. The development and results of an atmospheric absorption model used for preliminary analysis are discussed. The instrument specifications, the optical and mechanical design and budgetary considerations are presented. The solution of various imaging issues identified in the initial testing of the instrument are also discussed. The calibration of the instrument including a dynamic wavelength calibration scheme and the relative intensity calibration is presented in Chapter 4. A discussion of the collection and analysis of several data sets and a qualitative discussion of the effectiveness of the prototype is given in Chapter 5. A summary of the present work and recommendations for future development of the prototype are given in Chapter 6.

Chapter 2

Background

2.1 Introduction

This chapter explores the history of ozone measurement and provides an overview of the ground-based instruments used to monitor ozone. Pertinent atmospheric and optical theory is presented and a basic measurement scheme is proposed for the prototype developed in the present work.

2.2 A Brief History of Ozone Measurement

In the late 1800s, many spectroscopic researchers focused their efforts on the absorption and emission spectra of various molecules and elements as well as investigations of the solar spectrum. The sharp attenuation in the ultra-violet (UV) end of the solar spectrum was well known at the time, and it was suggested by *Cornu* [1881] that atmospheric absorption was responsible for this effect. Shortly thereafter, it was suggested by *Hartley* [1880] that ozone was the absorbing constituent; Hartley had made a low spectral resolution measurement of the UV absorption spectrum of ozone. Measurements of the ozone absorption spectrum were refined by *Chappuis* [1882] in the visual band and later by *Fabry and Buisson* [1913] in the UV. The higher-resolution ozone absorption spectra produced by Fabry and Buisson allowed them to derive the first estimate of the total atmospheric ozone column by comparing absorption spectra with solar spectra; the total column estimate was 5 mm at standard temperature and pressure, this is equivalent to 500 Dobson units [*Fabry and Buisson*, 1913]. The first instrument designed to measure atmospheric ozone was

developed by Fabry and Buisson and was used for a two week period in May-June of 1920 to measure ozone over Marseilles, France. Initial data from the Fabry-Buisson spectrophotometer refined previous estimates of total column ozone from 5 mm to 3 mm [*Fabry and Buisson*, 1921; *Dobson*, 1968].

The late 1920s saw the early development of quantitative theories relating to atmospheric ozone. Rayleigh and Göts showed that there was very little ozone near the surface of the Earth from observations of the UV lines from an Hg lamp over a distance of several kilometers [*Dobson*, 1968]. Preliminary monitoring of ozone columns showed both seasonal and latitudinal variations. There was much debate among theoreticians at the time as to whether solar UV or "corpuscular" radiation was the source of atmospheric ozone, and indeed whether the UV cutoff in the solar spectrum was due to ozone in the Earth's atmosphere or in the Sun's atmosphere [*Chapman*, 1931]. Questions were also being raised about the effects of stratospheric ozone on other geophysical parameters such as temperature [*Dobson and Harrison*, 1926; *Gowan*, 1928]. The mounting experimental evidence posed many questions and demanded a quantitative theory for the formation and distribution of atmospheric ozone. The demand was answered by Sidney Chapman's seminal paper, "A theory of upper atmospheric ozone" [*Chapman*, 1930]. This theory provided the foundations of ozone theory as it is understood today and is based on the concept that atmospheric ozone is generated through the dissociation of O_2 molecules by solar UV radiation and the subsequent recombination of the atomic oxygen with other O_2 molecules, Equations 2.1 and 2.2,

$$O_2 + h\nu \rightarrow O + O \tag{2.1}$$

$$O + O_2 + M \rightarrow O_3 + M, \tag{2.2}$$

where M is a third body. Other reactions (Equations 2.3 and 2.4) were also required to account for the re-combination of the atomic oxygen not consumed in the formation of ozone,

$$O + O \rightarrow O_2 \tag{2.3}$$

$$O + O_3 \rightarrow 2O_2. \tag{2.4}$$

Dissociation of the ozone molecule, either spontaneously or by absorption of solar radiation, was proposed as the mechanism for ozone loss (Equation 2.5), in addition to a recombination loss (Equation 2.6)

$$O_3 + h\nu \rightarrow O_2 + O \tag{2.5}$$

$$2O_3 \rightarrow 3O_2. \tag{2.6}$$

The inclusion of the density profile for molecular oxygen and the profile of solar flux absorption in Chapman's theory of ozone formation and destruction also accounts for the general vertical distribution of ozone, theoretically predicting the observed peak ozone density at an altitude of 25 km to 40 km. However, a lack of experimental data concerning transport at stratospheric altitudes meant that the early theories could not include ozone transport. Seasonal variation in solar radiation was not sufficient to explain the observed seasonal variations in ozone columns, although later study has shown that transport is very significant [*Chapman*, 1930; *Coy et al.*, 1997].

Instrument design and experimental work intensified in the 1930s. At Oxford, G. M. B. Dobson continued the pioneering work of Fabry and Buisson with the development of the Dobson spectrophotometer. The International Geophysical Year in 1957-58 saw the deployment of a world-wide network of ozone monitoring stations using Dobson spectrophotometers, many of which are still in use today [*Dobson*, 1968]. In 1973, A.W. Brewer, a former colleague of Dobson's, proposed a new instrument for ground-based ozone column measurements. The Brewer spectrophotometer is a more complex, automated instrument that is capable of making night-time measurements using the moon [*Brewer*, 1973]. The launch of the Nimbus-7 satellite in 1978 marked the beginning of satellite-based remote sensing of atmospheric ozone. Nimbus-7 carried both the TOMS (Total Ozone Mapping Spectrometer) and SBUV (Solar-Backscatter UV) instruments; these were the first remote sensing instruments to provide global, long term total ozone measurements. TOMS on Nimbus-7 functioned until 1993, and has since been replaced by several other TOMS instruments on other satellites.

Theoretical advances in ozone chemistry in the 1950s to 1970s expanded Chap-

man's original theory by including catalytic processes for ozone loss. *Bates and Nicolet* [1950] first suggested an HO_x catalytic reaction, and further catalysts such as NO_x, ClO_x and BrO_x were identified, all of which follow the same basic reaction cycle.

These theoretical advances led to concern over anthropogenic chemicals such as chlorofluorocarbons (CFCs) and halons, which were widely used until the late 1980s as chemical propellants, solvents and refrigerants, and had the potential to deplete stratospheric ozone. The discovery by *Farman et al.* [1985] of the antarctic ozone hole in 1985 showed experimental evidence of large scale depletion. *Solomon et al.* [1986] subsequently identified the photochemical mechanisms responsible for ozone depletion; these involved heterogeneous reactions on polar stratospheric clouds, NO_x, and anthropogenic ozone depleting compounds. These developments brought the attention of the World's governments, and in 1987 the United Nations Montreal Protocol on Substances that Deplete the Ozone Layer was signed by over 38 nations [*World Meteorological Organization*, 2003]. The Montreal Protocol and its subsequent amendments charged the signatory nations with improved monitoring and scientific understanding of the stratospheric ozone layer, and a reduction of emissions of ozone-depleting chemicals. Chemistry-climate model simulations predict an ozone column minimum prior to 2010, with a return to pre-1980 levels by the mid 21^{st} century [*World Meteorological Organization*, 2003].

2.3 Ground-Based Ozone Measurement

Despite the advances in satellite remote-sensing technology over the past three decades, ground-based observation of ozone remains an integral part of the global ozone monitoring effort. While satellite-based remote-sensing instruments are invaluable due to their wide geographic coverage, ground-based instruments offer a higher temporal resolution and thus provide a consistent, higher-density data set than satellite-based instruments. This section provides an overview of various ground-based ozone measuring instruments.

2.3.1 Dobson Spectrophotometer

The venerable Dobson spectrophotometer has been in service in various forms since the 1930s. Developed by G.M.B. Dobson at Oxford, the Dobson spectrometer is still the most popular ground-based ozone detection instrument, with over 90 operating world-wide [*World Meteorological Organization*, 1998].

The measurement principle of the Dobson spectrometer relies on the UV absorption by ozone. Two narrow wavelength bands are observed, 3110 Å and 3265 Å, the former being absorbed strongly by ozone and the latter only weakly. A double-spectrometer apparatus and an optical chopper are used to isolate the wavelengths of interest and minimize signal degradation from scattered visual-band wavelengths. The wavelength incident on the detector (a photomultiplier in the modern version) is alternated by the optical chopper, and differences in the current from the photoelectric detector are amplified and displayed. A neutral-density optical wedge filter is adjusted until the intensity of the two signals on the detector is equal, resulting in zero amplified output. The position of the optical wedge allows for the determination of the relative intensities of the two wavelengths of interest, and the ratio of the two intensities is then used to calculate the ozone column. The accuracy of the measurement is heavily dependent on the wedge calibration. The Dobson spectrophotometer is capable of making total ozone measurements from direct sunlight, scattered sunlight from the zenith clear sky, or zenith sky observations with light cloud with the observation of two additional wavelengths that are not absorbed by ozone [*Dobson*, 1931].

Automation of the Dobson spectrometer was first proposed by *Raeber* [1973] around the same time as the Brewer spectrophotometer was proposed. Most modern Dobson spectrophotometers have an automated data collection scheme, though calibration still remains a significant issue, especially in developing countries [*United Nations Environment Programme*, 2002].

2.3.2 Brewer Spectrophotometer

The Brewer spectrophotometer was developed in the early 1970s as a replacement for the Dobson spectrophotometer. While the general retrieval mechanisms based on observation of pairs of UV wavelengths remain the same for both instruments, the Brewer spectrometer takes advantage of a completely new design to reduce instrument errors and required observation times. Modern Brewer spectrophotometers are capable of zenith and azimuth tracking of the sun or moon, and can measure the relative intensities of up to four different wavelengths simultaneously [*Brewer*, 1973; *Kipp and Zonen*, 2000].

To achieve a physically robust and compact design, the Brewer spectrophotometer employs an Ebert spectrograph design. This spectrograph uses a grating operating in the 3rd order and a concave mirror. At the focal plane of the spectrograph are 5 slits, four of which are used for ozone retrievals and the fifth for calibration. Each slit is covered by a piezo-electrically operated shutter. A solid-state control system sequentially opens each shutter, and enables a counter specifically for that wavelength. Counting is enabled by electronic control rather than relying on the physical action of the shutters, so increasing instrument accuracy. An entire cycle sampling the four wavelengths takes approximately 128 ms, with 512 sample cycles being completed in approximately 1 min. The speed of the sampling by the Brewer spectrophotometer reduces errors present with the much slower Dobson spectrophotometer due to changes in the state of the sky during measurement [*Brewer*, 1973].

2.3.3 Lidar

Lidar (LIght Detection And Ranging) systems operate similarly to radar systems except that optical wavelengths are used. Lidar systems can provide altitude-resolved ozone profiles in both the troposphere and stratosphere. The selection of the laser wavelength and source intensity depends on the desired altitude of measurement. Tropospheric measurements require strongly absorbed wavelengths in the UV to observe the low ozone number densities, while stratospheric measurements require

high-power lasers that have effective signal strength at high altitudes. [*World Meteorological Organization*, 1998].

A technique called DIAL (DIfferential Absorption Laser) is used to measure the vertical distribution of ozone. This technique relies on two lasers of different wavelengths, which have different ozone absorption cross sections, emitted simultaneously. A separate system of spectrometers and photon counters observes the back-scattered radiation from the two lasers.

The lidar DIAL technique offers vertical resolutions of approximately 0.5 km at 20 km altitude decreasing to between 4 to 7 km at 50 km. As of the late 1990s there were 12 lidar stations established for long-term monitoring of stratospheric ozone. These stations provide data for satellite validation, and, due to their self-calibrating nature, are especially useful for long-term monitoring of trends [*World Meteorological Organization*, 1998].

2.3.4 Ozone Measurement Using Stellar Spectra

While most ground-based ozone instruments use the Sun as a source, the Brewer spectrophotometer can also use the moon, and lidars generate their own signal, the idea of using stars to measure atmospheric ozone is almost as old as the experimental science itself. The early failed attempts have given rise to several successful efforts in the last twenty years. Ground-based prototyping led to the European Space Agency's GOMOS (Global Ozone Monitoring by Occultation of Stars) remote-sensing instrument that uses stars exclusively as a method of measuring ozone profiles from orbit. Recent research has also successfully developed a method of extracting ozone columns from historical astronomical spectra.

The first attempt at an instrument to study ozone by observing stars was made by G.M.B. Dobson at Oxford. A "prismatic camera" was constructed in an attempt to detect diurnal variations in ozone columns by observing the pole star Polaris. Dobson noted that this initial attempt would only have been able to detect the existence of variations at night-time, but not measure the magnitude of any changes. Unfortunately the signal from Polaris was too small and the camera was a failure.

A second attempt was made in 1934 when a Féry spectrograph and the prismatic camera were transported to Spitzbergen, but this attempt also met with failure due to the insufficient light-collection capability of the prismatic camera, and transport damage to the spectrograph [*Dobson*, 1968].

After many years of little interest in using stars for the measurement of atmospheric ozone, the GOMOS Startrek instrument was developed in the mid 1990s as a ground-based method to validate the GOMOS retrieval algorithms and to test the GOMOS spectrometer design. This instrument was a star-tracking slitless imaging spectrometer that used a development model of the GOMOS instrument as the detector, and attempted to retrieve ozone columns from observations of Chappuis band absorption in the wavelength range 530 to 630 nm, with a spectral resolution of 1 nm. Initial retrievals were unsuccessful, with only a 13% ozone retrieval precision, and an ozone column half that measured concurrently by TOMS on METEOR-3. It should be noted that there was little optimization of the instrument for ground-based applications other than the addition of star-pointing capability, and there was a limited data collection period [*Oikarinen*, 1996].

Some recent work has focused on retrieving ozone columns from archived spectra measured for astronomical purposes in an effort to characterize long-term trends [*Griffin*, 2005]. Preliminary results using spectra from the bright stars Vega and Sirius collected between the years 1978 and 1985 show a maximum difference of only 7.5% when compared with spatially coincident ozone columns measured by TOMS. This promising new technique may allow for an expansion of the historic record of atmospheric ozone back to the early 1900s, if the challenges of such an interdisciplinary endeavour can be overcome.

Ground-based measurement of ozone using stellar spectra is a challenging field, but a successful instrument would be of great benefit. An instrument capable of making consistent night-time measurements could characterize diurnal variations and would be especially valuable at high latitudes in the polar winter, where ozone depletion is maximized. While some instruments are capable of using the moon to make night-time observations, the observable zenith angles are severely limited,

and in the polar winter this can lead to a limited amount of data [*Oikarinen*, 1996; *Fioletov et al.*, 1997].

2.4 Theory

This section presents the relevant background theory on ozone, the optical depth associated with the processes of scattering and absorption, the determination of path lengths through the atmosphere, a brief examination of the proposed measurement scheme for the instrument, and an overview of the optical theory related to aberrations.

2.4.1 Ozone

Ozone is an important atmospheric constituent; it participates in many of the fundamental chemical reactions that cycle molecules through our atmosphere. Ozone is the molecule primarily responsible for the absorption of ultra-violet radiation from the Sun. Ultraviolet radiation is associated with many adverse biological effects, including skin cancer, immune system suppression and cataracts in human beings, as well as agricultural crop damage. In addition, stratospheric ozone contributes to lower stratospheric heating, thus reductions in ozone levels could affect climate change [*IPCC*, 2001]. As a consequence, global monitoring of geographic and temporal trends in the ozone profile have become a focus for atmospheric scientists.

Ozone is precursor to oxidants such as OH and NO_3, that makes it an important component in tropospheric chemistry. Aside from anthropogenic sources of surface ozone, tropospheric production is minimal [*Zellner*, 1999]. Atmospheric ozone is found mainly in the stratosphere at altitudes between 15 km and 40 km, where it is maintained in a balance between production by photodissociation of molecular oxygen and subsequent destruction by chemical processes and the absorption of solar radiation. Figure 2.1 shows vertical ozone profiles obtained by two different satellite instruments, the American SAGE II and the Canadian built OSIRIS.

The basis of ozone production in the atmosphere is the photodissociation of

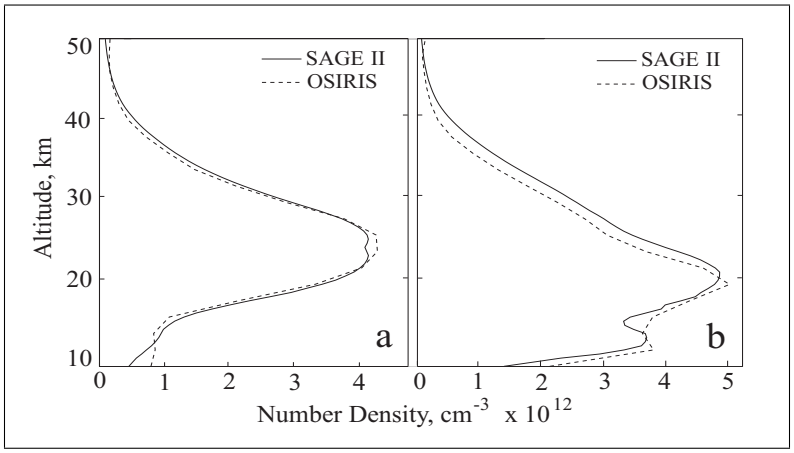

Figure 2.1: Zonally averaged ozone profiles for (a) January, 2002 and (b) May, 2002 from the OSIRIS and SAGE II satellite instruments [*Petelina et al.*, 2004].

molecular oxygen,

$$O_2 + h\nu(\lambda < 242\text{nm}) \rightarrow 2O \tag{2.7}$$

and recombination of the atomic oxygen with molecular oxygen,

$$O + O_2 + M \rightarrow O_3 + M, \tag{2.8}$$

where M is a third body that is necessary for energy and momentum balance.

In a non-chemically-perturbed atmosphere ozone destruction is dominated by solar photo-dissociation. Different wavelengths carry different energies, according to $E = \frac{hc}{\lambda}$, where E is the energy of a photon at wavelength λ, h is Plank's constant and c is the speed of light. Depending on the energy of an incident photon, the ozone molecule may or may not be dissociated. The potential for dissociation is characterized by the absorption cross section, which is determined by the allowed electronic, rotational and vibrational transitions of the molecule. The absorption cross section of ozone is shown in Figure 2.2. The photodissociation of ozone can occur for wavelengths below approximately 850 nm, beginning with the relatively weak absorption in the Chappuis band, which is the band of interest for the current work. The Chappuis band is a broad feature that extends from approximately 440 to 850 nm. The absorption here is relatively weak because the dissociation is a *spin*

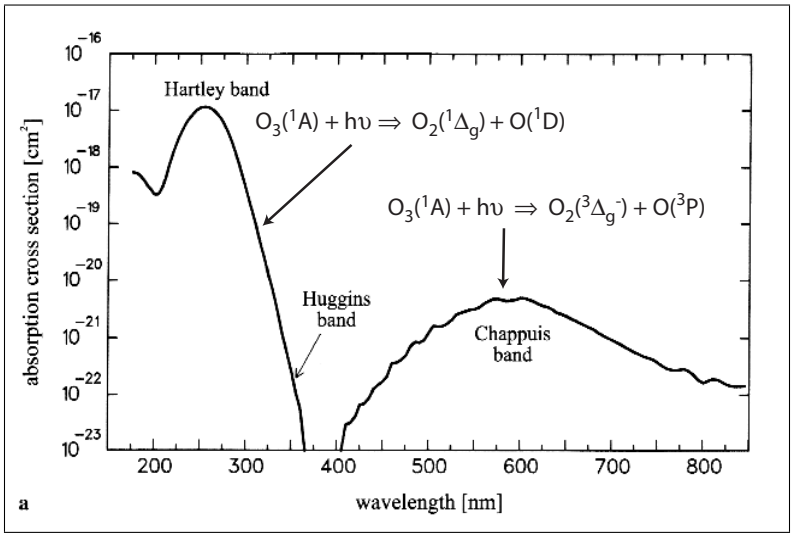

Figure 2.2: Absorption spectrum of ozone [*Zellner*, 1999].

forbidden process [*Zellner*, 1999],

$$O_3(^1A) + h\nu(440 - 850 \text{ nm}) \rightarrow O_2(^3\Sigma\ ^-_g) + O(^3P). \tag{2.9}$$

A much more powerful absorption band is the Hartley band, from 200 to 310 nm. This is the band that is responsible for the absorption of harmful UV radiation. The process that occurs in the Hartley band (Equation 2.10) is fully spin-allowed, hence the large ozone absorption cross section in this band [*Zellner*, 1999],

$$O_3(^1A) + h\nu(200 - 310 \text{ nm}) \rightarrow O_2(^1\Delta_g) + O(^1D). \tag{2.10}$$

While solar or lunar measurements of ozone number density can be based on differential UV absorption due to the large flux from these sources, the large absorption cross-section in the Hartley band eliminates the majortiy of the weak UV flux from stars. The smaller absorption cross-section of the Chappuis band is ideal for stellar measurements.

In addition to photolysis as a destruction process, various chemical catalysts are very efficient at destroying ozone. Chemicals such as NO_x, ClO_x and BrO_x are all catalysts that follow a similar reaction cycle to destroy ozone,

$$\begin{aligned} \mathrm{X} + \mathrm{O_3} &\rightarrow \mathrm{XO} + \mathrm{O_2} \\ \mathrm{O} + \mathrm{XO} &\rightarrow \mathrm{X} + \mathrm{O_2} \\ \hline \mathrm{O} + \mathrm{O_3} &\rightarrow 2\mathrm{O_2} \quad \text{(Net)} \end{aligned} \tag{2.11}$$

where X is the catalyst molecule [*Zellner*, 1999].

The balance between production and destruction, as well as dynamic transport processes, dictate the stratospheric ozone content at a particular time and place. Maximum production occurs at the equator and decreases with latitude; this is due to increased solar radiation at low latitudes. Depletion in the arctic and antarctic regions occurs mainly in the lower stratosphere due to a combination of low ozone production, cold temperatures and a dynamic process called the polar vortex. Polar stratospheric clouds form due to low temperatures and release ozone destroying catalysts from their "reservoir" compounds. The catalysts remain inert until photolysed by visible or UV radiation from the sun in the polar spring, and destroy ozone at a much greater rate than it is produced, leading to significant depletion and the seasonal appearance of the ozone hole [*World Meteorological Organization*, 2003].

2.4.2 Optical Depth

Transmission of light incident on a homogeneous parcel of atmosphere is characterized by the optical depth of the parcel. Optical depth, denoted by τ, is used to express the transmission of the parcel,

$$\mathrm{I_{final}} = \mathrm{I_{initial}} \mathrm{e}^{-\tau}, \tag{2.12}$$

where I_{initial} is the intensity of light incident on the parcel, and I_{final} is the intensity of light exiting the parcel. The transmission is $\mathrm{e}^{-\tau}$, and τ is the optical depth of the parcel. Optical depth depends on the path length through the parcel, the number density of species present in the parcel, and the extinction cross-sections of those species. Extinction refers to the attenuation of light as it passes through the parcel. Extinction can occur due to scattering or absorption, and is wavelength dependent in both cases.

Consider an entire atmosphere composed of layers, the optical depth τ for a particular layer is defined by

$$\tau_{\text{layer}} = \sum_{\text{j}} \left[\int_s \sigma_j n_j ds \right], \tag{2.13}$$

where σ_j and n_j are the absorption/scattering cross-section and the number density of the j^{th} species, respectively. Species j is any species that causes extinction of the incident light. The integral produces the optical depth for the j^{th} species through the layer along the line of sight, where s is the path length through the layer. A summation of the optical depths due to each species produces the optical depth along the line of sight for a particular layer. Summation of the optical depths due to each species j in each layer k, Equation 2.14,

$$\tau_{\text{total}} = \sum_{\text{k}} \sum_{\text{j}} \left[\int_s \sigma_j n_j ds \right] \tag{2.14}$$

yields the total optical depth for the entire atmosphere along the line of sight.

2.4.2.1 Scattering

Scattering is the form of extinction that occurs when a particle in the path of an electromagnetic wave interacts with the wave and reradiates. The reradiated light follows a solid-angle dependance that is based on the size of the particle relative to the wavelength of the incident light. This "size parameter" is the ratio of the circumference of the particle to the wavelength of the light [*Liou*, 2002]. Rayleigh scattering refers to scattering by a particle with a radius much smaller than the wavelength of light. In this case, light is generally scattered equally in the forward and backward directions (relative to the propagation of the incident wave). The following simple formula may be used to determine the scattering cross-section (in cm^2), of a Rayleigh scattering particle, for a particular wavelength of light [*Brasseur and Solomon*, 1984]:

$$\sigma_{rayleigh} = \frac{4.0 \times 10^{-28}}{\lambda^{3.916+0.074\lambda+0.05\lambda^2}} \qquad [\text{cm}^2], \tag{2.15}$$

where λ is in units of μm. The approximate λ^{-4} dependence means that shorter wavelengths are more easily scattered by Rayleigh particles. Forward scattering

becomes increasingly dominant as the particle size approaches the wavelength of the incident light. For a particle with a radius on the order of the illuminating wavelength, light is scattered almost completely in the forward direction. This is referred to as Mie scattering, which is caused by large aerosol particles, ice crystals, fog, and other airborne particles such as dust.

2.4.2.2 Absorption

Absorption is similar to scattering in that it attenuates light as it passes through a parcel of air. However with absorption, there is no immediate re-radiation. The energy of an incident photon is absorbed and can lead to changes in the energy configuration of the molecule; it may add to the rotational or vibrational kinetic energy of the molecule or change the electronic configuration of the molecule, so changing its potential energy. Depending on the energy of the incident photon, these changes in potential and kinetic energy may lead to photolysis of the molecule or photoionization [*Liou*, 2002]. Absorption depends on temperature and, like scattering, is also a wavelength dependent process.

2.4.2.3 Number Densities

The purpose of an instrument that studies the atmosphere is generally to determine the number densities of different species, typically trace gases. The number densities of the major atmospheric constituents are well known and well modeled; they generally follow an exponential decrease with altitude up to 100 km. The vertical profile of ozone number density peaks in the 15-30 km range. Above the peak, ozone number density decreases rapidly, as shown previously in Figure 2.1. An analysis of the variation in the number densities of different species provides information on the chemistry and transport of those species. The purpose of the instrument designed in the current work is to determine the vertical profile of ozone number density, by observing light that has been attenuated by both absorption and scattering processes as defined by Equation 2.12. If the initial intensity is known, the observation is a measurement of the optical depth, τ. Therefore if the initial intensity, the optical

depth, the cross-sections and path length are known, it is possible to determine the number density of a species.

2.4.3 Determination of Path Length

In order to calculate the transmission of a particular layer in the atmosphere, the line of sight path length through that layer (s in Equation 2.13) is required. The geometry for an instrument observing a star is shown in Figure 2.3. This assumes a circular Earth and an atmosphere composed of m circular homogeneous layers. Using the Sine Law and that the sum of all angles in a triangle is π, the angle ψ is found to be,

$$\psi = \theta - \arcsin \frac{R_0 \sin(\pi - \theta)}{R_m}. \tag{2.16}$$

The Cosine Law is used to determine the path length, at angle θ, from the instrument on the surface of the earth to the radius R_m of layer m,

$$P_{sm} = \sqrt[2]{{R_0}^2 + {R_m}^2 - 2R_0 R_m \cos\psi}, \tag{2.17}$$

where P_{sm} represents the distance to the top of an arbitrary layer. Then subtracting the distance to the top of the previous (lower) layer yields the path length within the current layer of interest:

$$P_m = P_{sm} - P_{sm-1}. \tag{2.18}$$

If the absorption cross-sections of the species and the path length within a layer are known, then measuring the optical depth allows the calculation of species number densities. This is the goal of the present work.

2.4.4 Measurement Scheme

The purpose of the observations is to determine the ozone number density at different altitudes. The measurement scheme must allow the ozone number densities to be derived from the observed intensities. For the assumption of a single wavelength along the line of sight in Figure 2.3 and an atmosphere composed of stacked

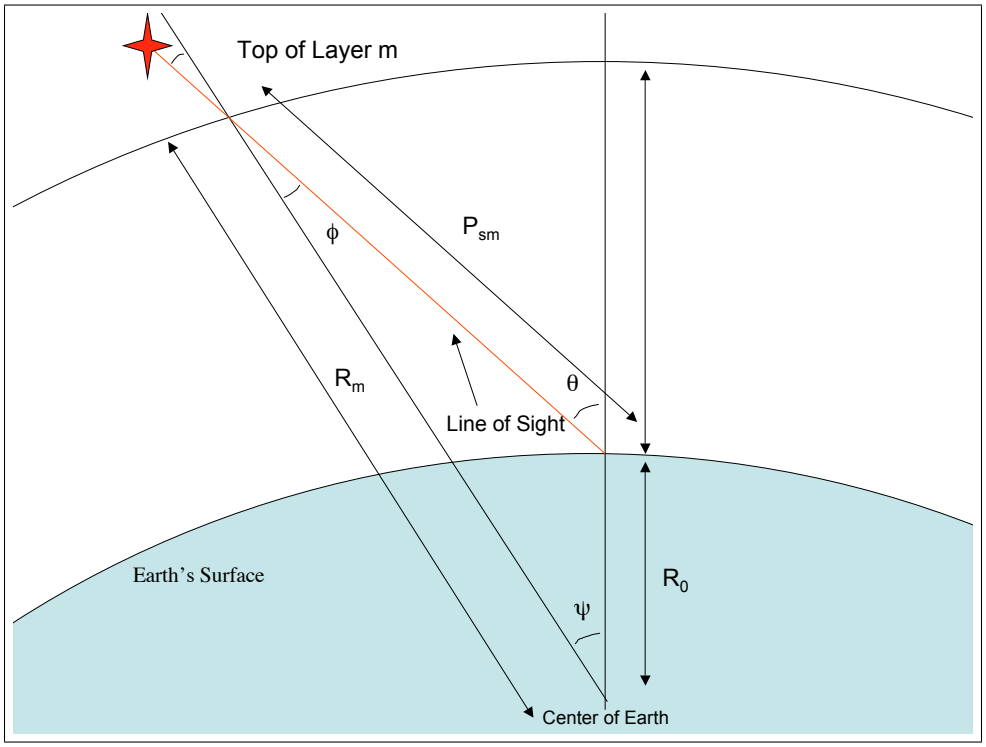

Figure 2.3: Geometry for the determination of the path length through a layer.

homogeneous layers, the i^{th} observation can be represented as,

$$\mathrm{I}_{\theta_\mathrm{i}} = \mathrm{I}_{\mathrm{initial}} \mathrm{e}^{-\tau(\theta_\mathrm{i})}. \tag{2.19}$$

For a reference angle observation $\mathrm{I}_{\theta_{\mathrm{ref}}}$ and another observation I_{θ_1},

$$\mathrm{I}_{\theta_{\mathrm{ref}}} = \mathrm{I}_{\mathrm{initial}} \mathrm{e}^{-\tau(\theta_{\mathrm{ref}})} \tag{2.20}$$

and

$$\mathrm{I}_{\theta_1} = \mathrm{I}_{\mathrm{initial}} \mathrm{e}^{-\tau(\theta_1)}. \tag{2.21}$$

The ratio of the two observed intensities (Equations 2.20 and 2.21) provides the difference in the optical depths for the transmission exponent:

$$\frac{\mathrm{I}_{\theta_1}}{\mathrm{I}_{\theta_{\mathrm{ref}}}} = \mathrm{e}^{-\tau(\theta_1)+\tau(\theta_{\mathrm{ref}})}. \tag{2.22}$$

Taking the natural logarithm of both sides of Equation 2.22 yields an observation O_1,

$$\mathrm{O}_1 \equiv \ln \frac{\mathrm{I}_{\theta_1}}{\mathrm{I}_{\theta_{\mathrm{ref}}}} = \tau(\theta_{\mathrm{ref}}) - \tau(\theta_1). \tag{2.23}$$

If it is assumed that the number densities of neutrals and the absorption cross-section of ozone are well known, the former can be reliably accessed from various models e.g. MSIS, then the optical depth due to ozone can be determined. However, because the absorption cross-section of ozone is temperature dependent, the atmospheric temperature profile must also be known. The European Center for Medium Range Weather Forecasting (ECMWF) model can be used to provide these temperatures with a high degree of accuracy [*Molenti et al.*, 1996].

To retrieve the ozone number density, the optical depths are expanded in each layer,

$$\tau(\theta_i) = \sum_{\mathrm{k}} (\sigma_j [O_3]_j \Delta x_{ij} + \sigma_j n_j \Delta x_{ij}), \tag{2.24}$$

where $\tau(\theta_i)$ defines the optical depth for observing angle θ_i through all layers k, Δx_{ij} is the path length through the $(j)^{th}$ layer at angle θ_i, $[O_3]_j$ is the ozone number density, n_j is the number density of scattering species and and σ_j is the absorption and scattering cross-section of the species. Then substituting Equation 2.24 into Equation 2.23 and simplifying yields

$$\mathrm{O}_1 \equiv \ln \frac{\mathrm{I}_{\theta_1}}{\mathrm{I}_{\theta_{\mathrm{ref}}}} = \sigma \sum_{\mathrm{j}=0}^{\mathrm{m}-1} ([\mathrm{O}_3]_{\mathrm{j}} + \mathrm{n}_{\mathrm{j}})(\Delta \mathrm{x}_{\theta_{\mathrm{refj}}} - \Delta \mathrm{x}_{\theta_{1\mathrm{j}}}) \tag{2.25}$$

for a reference angle observation at zenith distance θ_{ref} and an observation at angle θ_1. Generalizing for m layers, it is evident that *m+1* observations at different angles are required to derive the m-layer profile. If each observation from *0* to *m-1* is ratioed with the $(m)^{th}$ observation, then m equations with m unknowns, $\mathrm{O}_1 ... \mathrm{O}_{\mathrm{m}}$, are obtained. The ozone number densities can be retrieved by solving the system of equations.

The measurement scheme presented above is general but it is essential if the instrument is to provide vertical profiles of ozone number density. Several significant factors that affect the observed optical depth were not considered in the above analysis, such as an increased path length due to atmospheric refraction and increased extinction due to aerosols. While these factors must be considered in an accurate analysis, the comprehensive development of a suitable retrieval algorithm is beyond the scope of the present work.

2.4.5 Aberrations

While coarse optical system design may be made for the assumption of ideal lenses, an examination of the effects of aberrations on system design is essential. Optical aberrations are deviations from ideal lens performance and may be either chromatic or monochromatic. Chromatic aberrations are wavelength dependent, while monochromatic aberrations result from lens design and affect all wavelengths equally.

Neglecting the effects of diffraction, all light from a plane wave incident on the aperture of an ideal thin lens is focused to a perfect point. Such performance is considered "paraxial", in that ray bundles parallel-to and near the optic axis of the lens behave in this fashion. Deviations from paraxial performance of ray bundles are due to aberrations.

Equations for tracing meridional rays are derived from the geometry of a single spherical surface, shown in Figure 2.4, using Snell's Law and the Sine Law [*Jenkins and White*, 1976]:

$$\sin\phi = \frac{r+s}{r}\sin\theta \tag{2.26}$$

$$\sin\phi' = \frac{n}{n'}\sin\phi \tag{2.27}$$

$$\theta' = \phi' + \theta - \phi \tag{2.28}$$

$$s' = r - r\frac{\sin\phi'}{\sin\theta'} \tag{2.29}$$

$$\sin\phi = \frac{h}{r} \tag{2.30}$$

$$\theta' = \phi' - \phi, \tag{2.31}$$

where s and s' are the object and image distances from the vertex of the surface, respectively, n and n' are the indices of refraction for the two materials, r is the radius of the surface of interaction, ϕ is the angle of the incident ray with respect

to a radial vector to the surface at the point of refraction, and ϕ' is the angle of the refracted ray measured counter-clockwise from the radial vector. The height of the point of refraction above the optic axis is represented by h, and θ and θ' are the angles of the incident and refracted rays with respect to the optic axis, respectively.

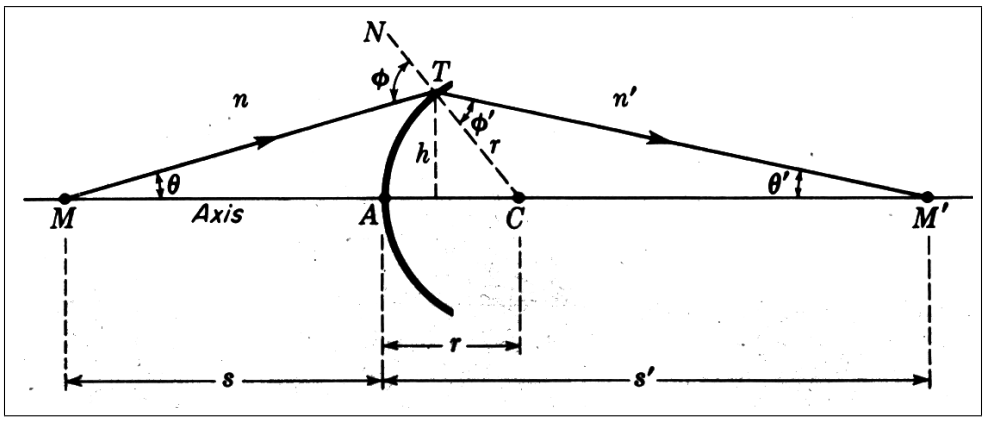

Figure 2.4: Geometry for deriving the basic ray trace equations. From *Jenkins and White* [1976].

The paraxial ray approximation is obtained from an application of Equations 2.26 through 2.31 to a system of lenses with the assumption that θ is a small angle so that $\sin\theta \simeq \theta$. In the case of an ideal lens all rays behave according the paraxial approximation. A quantification of aberrations, which are apparent in real lenses, can be achieved by performing a McLaurin Series expansion of the sine of angles in the above equations [*Hopkins*, 1988]:

$$\sin\theta = \theta - \frac{\theta^3}{3!} + \frac{\theta^5}{5!} - \frac{\theta^7}{7!} + ... \tag{2.32}$$

Truncating the series after the first term and substituting into ray tracing equations 2.26 through 2.31 yields the paraxial approximation. Subsequent terms in the series are quantifications of the lens aberrations. Using the first two terms in the series results in equations that incorporate *3rd order* aberrations. Using the first three terms accounts for *5th order* aberrations, etc.

The magnitude of the aberrations may be quantified by examining the imaging differences between paraxial theory and 3rd order theory. For the assumption of a

rotationally-symmetric optical system as shown in Figure 2.5, a general ray is imaged at a location in the image plane defined using paraxial optics. This is the position where a general ray would be imaged in a system free of aberrations. Deviations from this paraxial position in the y-direction are defined by ϵ_y. Using a power-series expansion for the deviations, one obtains

$$\epsilon_y = \epsilon_{3y} + \epsilon_{5y} + ..., \tag{2.33}$$

where ϵ_{3y} corresponds to deviations associated with 3rd order aberrations, and thus a quantification of their magnitude in the image plane. For the geometry shown in Figure 2.5, the the 3rd order deviations are described by

$$\epsilon_{3y} = \sigma_1\rho^3\cos\theta + \sigma_2\rho^2(2+\cos 2\theta)(FOB) + (3\sigma_3+\sigma_4)\rho\cos\theta(FOB)^2 + \sigma_5(FOB)^3, \tag{2.34}$$

where ρ is the radial distance of the ray from the optic axis, and FOB is the fractional object height in the object plane. From left to right in equation 2.34, the coefficients σ_i represent the five 3rd order aberrations: Spherical, Coma, Astigmatism and Field Curvature, and Distortion [*Hopkins*, 1988].

Spherical aberration results from marginal rays and axial rays having different focal lengths. For a plane wave incident on a positive lens rays are focused into a range of focal lengths determined by the height of the incident ray. Coma aberration affects off-axis rays. The magnification of the object is affected by the height of the incident ray, with the result that a plane wave is imaged as a smear of points. Marginal rays produce a larger spot size, so that a comet shaped image is produced. Astigmatism results from different focal lengths in the saggital and tangential planes, and is significant only for off-axis objects. Field curvature is the fourth 3rd order aberration; off-axis images have a different focal length than paraxial images so that the focal surface of the lens is curved. The result is that the field is never focused on a planar surface. The final 3rd order aberration is distortion, in which magnification varies over the field of the lens. Marginal rays that encounter less magnification than central rays results in *barrel* distortion, while lower magnification for central rays results in *pincushion* distortion.

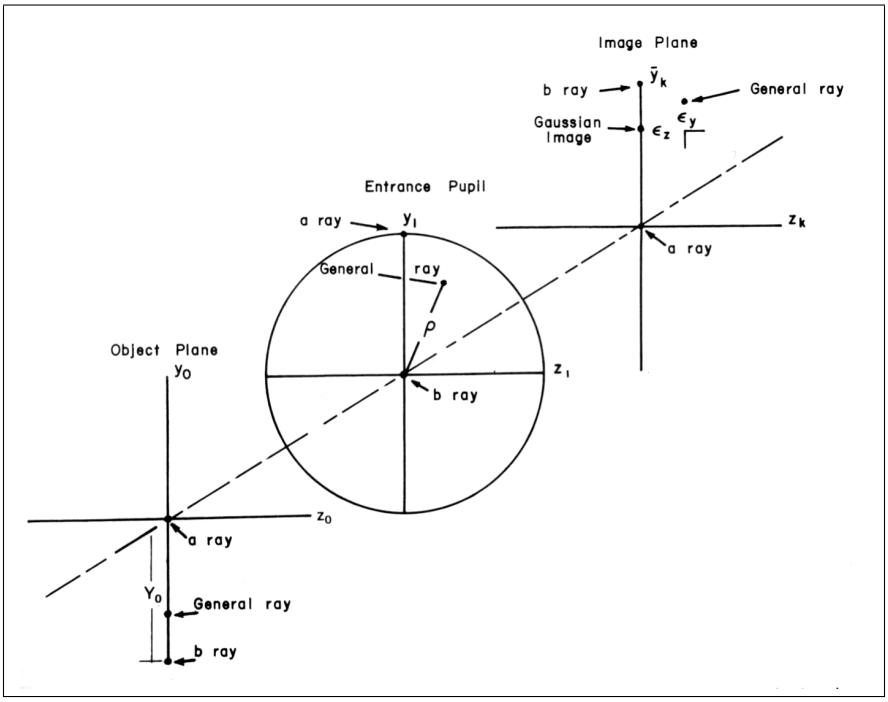

Figure 2.5: Geometry for deriving the aberration coefficients. From *Hopkins* [1988].

An understanding of the effects of aberrations and the required mitigation strategies is essential in any optical design, and the current work is no exception. Details of the optical design of the instrument and the correction of aberrations is given in Sections 3.5 and 3.8.

2.5 Conclusion

Knowledge of the background research and theory gives a solid foundation for the planning and design of a prototype instrument. As an attempt at a new style of ozone-measuring instrument, a clear knowledge of past work and the current state of research in the field of ground-based ozone detection is necessary to proceed without repeating the mistakes of the past. The theory applicable to the design of the instrument and the physical parameters being measured provides the tools required for a successful design.

Chapter 3
Instrument Design, Manufacture, and Testing

3.1 Introduction

The constructed instrument is a prototype that proceeded from specifications through initial design to manufacture and testing. The design process had many aspects, including preliminary modeling, budgetary considerations, optical and mechanical design, and software integration.

Before considering the physical design for the instrument, a basic atmospheric absorption model was developed using the IDL programming language. The model simulates the effects of Rayleigh scattering and ozone absorption on incoming starlight, for a given input spectrum and stellar zenith angle (SZA). This initial analysis was intended to verify the general concept for detecting ozone absorption in stellar spectra, specifically with respect to the signal to noise ratio required in the instrument. The results from the model showed an observable absorption in the Chappuis band, with a good signal to noise ratio, for a 4th magnitude star.

Following the design specifications for the instrument, an initial concept was developed. This conceptual design led to a more detailed analysis of system features. A custom prism spectrometer was designed, and a commercial telescope and CCD camera were purchased for the light collection and imaging components. The optical design of the prism spectrometer was implemented in a physical prototype, together with the mechanical interfaces to the CCD and telescope. The prototype was field tested and several unexpected design flaws were investigated and corrected.

3.2 Specifications

To progress from concept to prototype, the first stage of the design process is to provide the instrument specifications. As an attempt at a low-cost imaging spectrometer, the specifications were left somewhat broad, with an emphasis on synthesis of commercially available equipment to reduce development time and total cost. The initial specifications are listed below.

- Prototype instrument for ground-based optical absorption spectroscopy by observation of stars
- Slitless imaging spectrometer
- Observation of the Chappuis ozone absorption band (500 nm-700 nm)
- Low resolution: approximately 10 nm per-pixel bandpass
- Capable of detecting magnitude 4.0 stars
- Signal to noise ratio of calibrated output $\geq$ 10:1
- Automated data collection, including a self-pointing ability
- Reduced cost and lead times by using commercially available equipment
- Total cost less than $ 10 000.00

As stated above, the general concept of the instrument is a low-cost, ground-based proof-of-concept system that can detect atmospheric absorption due to ozone in stellar spectra. Specifying a limiting magnitude of 4.0 ensures that there are enough observable stars that the instrument is not limited to observing specific azimuth and zenith angles due to seasonally varying star configurations. By capturing an image of a star field, the instrument gathers more information per exposure than it would from the spectrum of a single star, thus the instrument is specified to be a slitless imaging spectrometer; however, single-star tracking and imaging was used as the baseline in the current work. Ozone absorption in the Chappuis band is a broad feature covering approximately 200 nm (as shown previously in Figure 2.2) and does not require high spectral resolution for detection. In addition, a lower resolution spectrometer reduces the potential problem of overlapping spectra in the image of

a starfield. Calibrated output is specified as having a signal to noise ratio $\geq$ 10:1. As with all engineering projects, the specifications are both a guide and a design goal, and the management of inherent design trade-offs is necessary for a balanced outcome in terms of cost and performance.

3.3 Absorption Model

A simple atmospheric model was developed in the IDL programming language, for the initial analysis of the viability of ozone detection using ground-based stellar observations. The model incorporates absorption due to atmospheric ozone and single-scatter extinction due to Rayleigh scattering. Using a two-dimensional atmosphere constructed of circular homogeneous layers containing N_2, O_2 and O_3, the model determines the intensity observed on the ground at wavelengths in the Chappuis band, for a given input spectrum and a range of stellar zenith angles.

3.3.1 Model Structure

The model calculates the observed intensity at a given wavelength and observing angle, for all wavelengths and observing angles specified by the user and for a defined input spectrum. The Earth is assumed to be spherical and the atmosphere composed of homogeneous spherical shells. Atmospheric refraction and aerosol effects are neglected. The wavelength and observation angle limits, top of atmosphere altitude and the number of layers to be used are all specified by the user. The initial stellar spectrum, the ozone absorption cross-sections, and the number density profiles for ozone and neutral air are read from database files. These quantities, which are all either well known or modeled, are acquired from sources such as the MSIS (Mass Spectrometer, Incoherent Scatter) atmospheric constituent model [*Hedin*, 1991], the VizieR stellar catalogue database [*Ochsenbein et al.*, 2000] and the ECMWF centre [*Molenti et al.*, 1996]. A program flow diagram for the absorption model is shown in Figure 3.1. Simulation begins by initializing each layer with the appropriate number densities of each species. The model then determines the path length through each

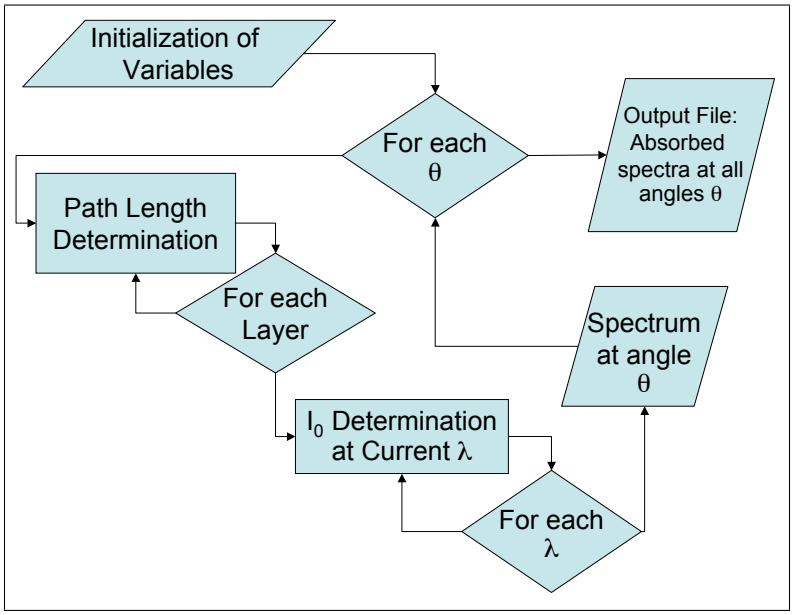

Figure 3.1: Program flow diagram for the absorption model.

layer for the given stellar zenith angle (SZA), using Equations 2.16, 2.17 and 2.18. This allows a determination of the optical depth of each layer along the current line of sight (observing angle) from Equation 2.13. Once τ has been determined for each layer, the optical depths are summed and the transmission of the atmosphere at the current observing angle is calculated for each wavelength in the band of interest. The transmission is then used to calculate the spectrum observed by the instrument according to Equation 2.12. The observing angle can be incremented and the process repeated for the range of user-defined stellar zenith angles.

3.3.2 Absorption Model Results

Initial results from the model were obtained with standard species number density profiles, ozone absorption cross-sections, and a flat spectrum for inputs. These results showed that ozone absorption is separable from Rayleigh scattering at low to mid stellar zenith angles for wavelengths within the Chappuis band. High zenith angles exhibited an enhanced ozone absorption, although extinction from Rayleigh scattering dominates. Figure 3.2 shows the individual and combined contributions

of ozone absorption and Rayleigh scattering for both low and high zenith angles. The results for extinction only due to scattering (no O_3) show a significant difference from the results that include attenuation from both scattering and absorption.

The depth of the Chappuis absorption feature is related to the amount of ozone along the line of sight and the measurement of the depth of the ozone absorption feature is the goal of the proposed instrument. However, the model results shown in Figure 3.2(b) indicate that Rayleigh extinction accounts for an estimated 30% of the observed feature depth at 600 nm and a SZA of 85°, and over 50% at a SZA of 0°. Thus, Rayleigh scattering must be well modeled and properly included into the analysis of observations if there is to be minimum error in the derived ozone column. While ozone was not expected to give significant absorption at low stellar zenith angles, due to the shorter path lengths, the model results indicate significant ozone absorption (approximately 10% of the total signal) for a stellar zenith angle of 0 degrees. Observations at large stellar zenith angles exhibit enhanced Rayleigh scattering because of longer path lengths.

In a further test the known spectrum of the 0^{th} magnitude star Aldebaran (α Tauri) from catalogue III/126 [*Burnashev*, 1985] was used as input to the model. Ozone absorption in the Chappuis band is at a maximum at approximately 600 nm, while both Chappuis absorption and Rayleigh scattering are much less significant at wavelengths beyond 700 nm. With the spectrum of Aldebaran as input, the ratio of modeled intensities at 600 nm and 700 nm was calculated for various stellar zenith angles. This ratio gives an indication of the expected feature depth at 600 nm, and characterizes the contribution of Chappuis absorption and Rayleigh scattering to the total feature depth. The smaller the ratio, the greater the feature depth. As seen in Figure 3.3, at low stellar zenith angles the ratio approaches a maximum which is due to the shape of the stellar spectrum, while at larger zenith angles the ratio decreases rapidly as ozone absorption and Rayleigh scattering increase due to longer path lengths through the atmosphere. It should be noted that atmospheric refraction was not considered in this analysis.

(a)

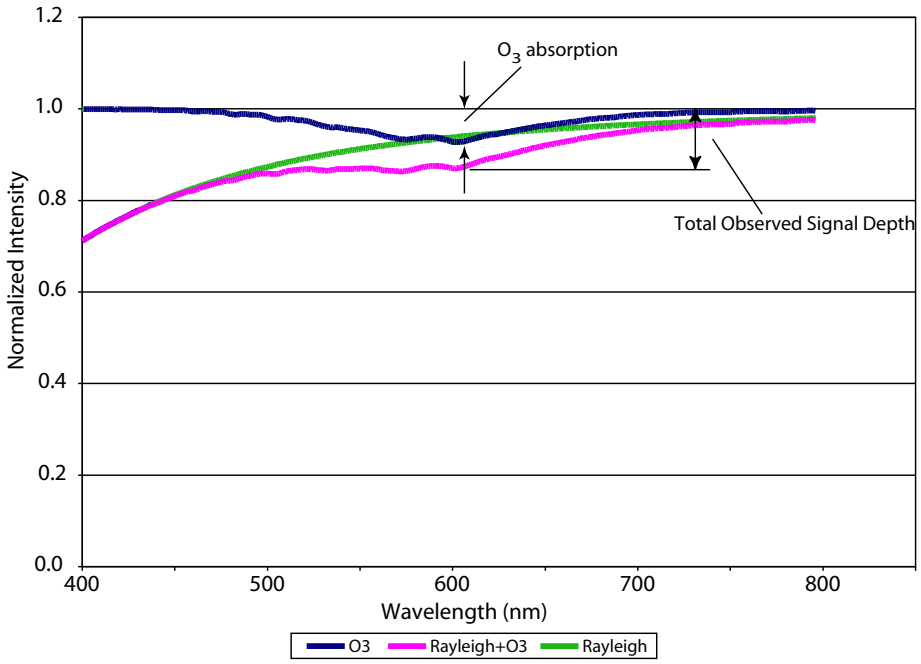

(b)

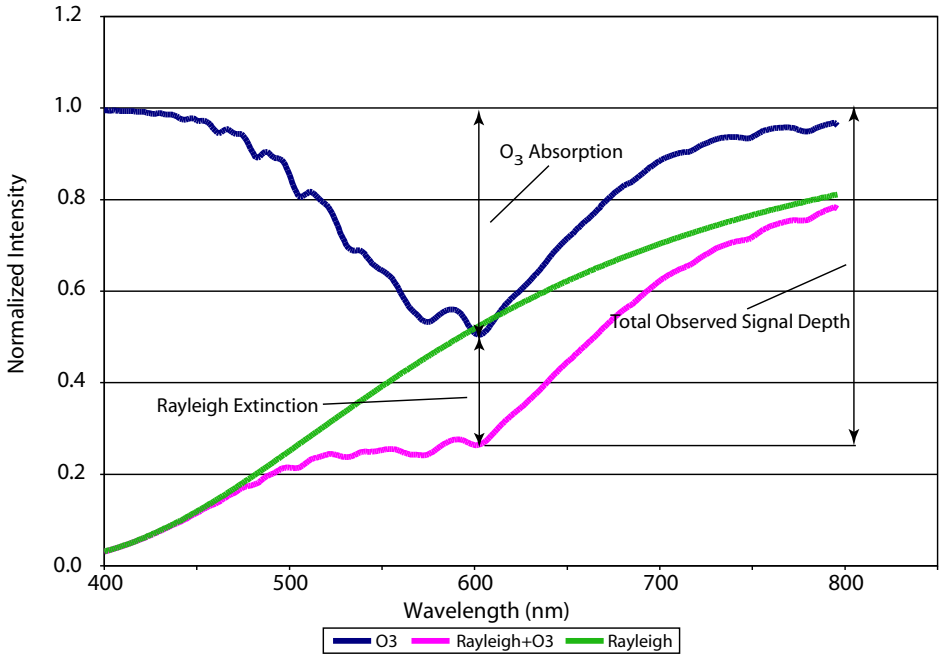

Figure 3.2: Modeled intensities for (a) 0° and (b) 85° stellar zenith angles using a flat spectrum as input. Attenuation due to ozone and Rayleigh scattering are shown separately, in addition to the total attenuation.

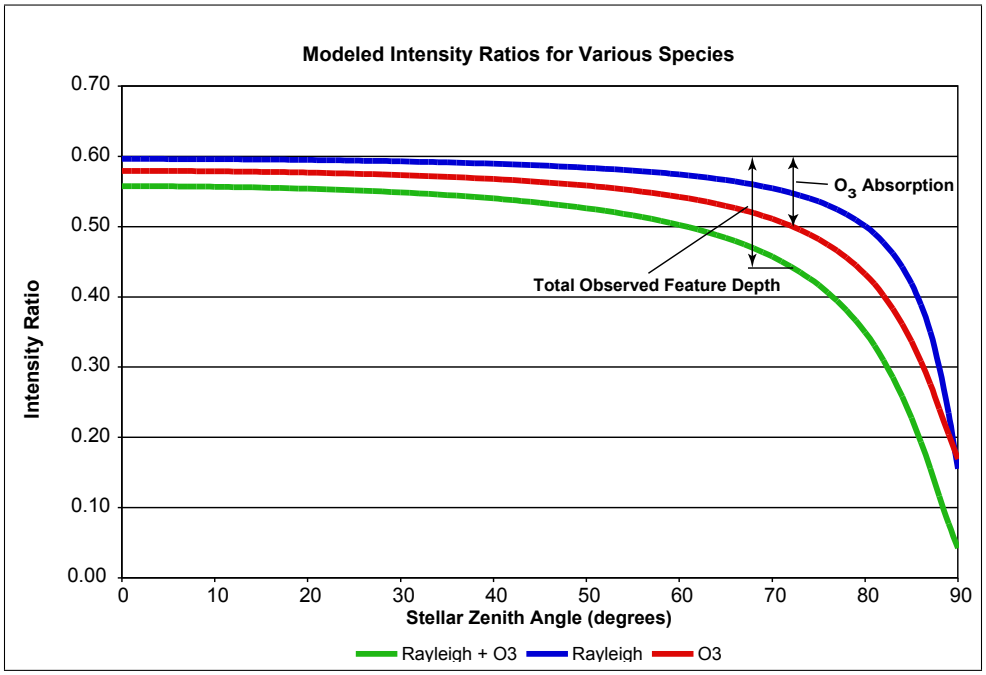

Figure 3.3: Characterization of the Chappuis feature depth as a function of stellar zenith angle, using a catalogue spectrum of Aldebaran as input. The ratio of the modeled intensities at 600 nm and 700 nm provides an estimate of the contributions of Chappuis absorption and Rayleigh extinction to the feature depth at 600 nm.

Figure 3.3 shows that the absorption of the input signal due to ozone at stellar zenith angles of 70° and greater is above 50%. This large absorption validates the concept of observing Chappuis absorption features in the spectra of stars. These data also show that, for 50% absorption due to ozone at 600 nm, the instrument must have a signal to noise ratio of approximately 100:1 to achieve a signal to noise ratio of 50:1 for the depth of the observed feature. For the approximate 10% modeled absorption at small zenith angles seen in Figure 3.2(a), an instrument SNR of 100:1 yields a 10:1 signal to noise ratio in the observed feature depth. Thus, a minimum instrument signal to noise ratio of 100:1 is required to achieve the specification of a signal to noise ratio of 10:1 in the observed feature depth at low zenith angles. This indicates that a detector with high quantum efficiency and low thermal noise generation is required.

3.4 Initial Design Concept

After coarse validation of the observation concept with the model, a preliminary design concept that satisfied the specifications was produced. The nature of the instrument as a stellar spectrometer requires the use of a telescope for light collection and an imaging device for recording spectra. The specification requiring slitless imaging suggested the use of a simple slitless prism spectrometer that relies on the small angular size of stars to serve as a slit.

The initial concept included a commercial astronomical telescope, a dispersing optics package, and a commercial astronomical CCD for imaging. Figure 3.4 is a block diagram of this design. The telescope tracks the star of interest using integrated commercial and custom software. Incoming starlight is collected and focused by the telescope and collimated before passing to the prism. The collimated light is dispersed into its constituent wavelengths by the prism and focused on to the CCD. The CCD records the spectrum and the image is read by the CCD control software.

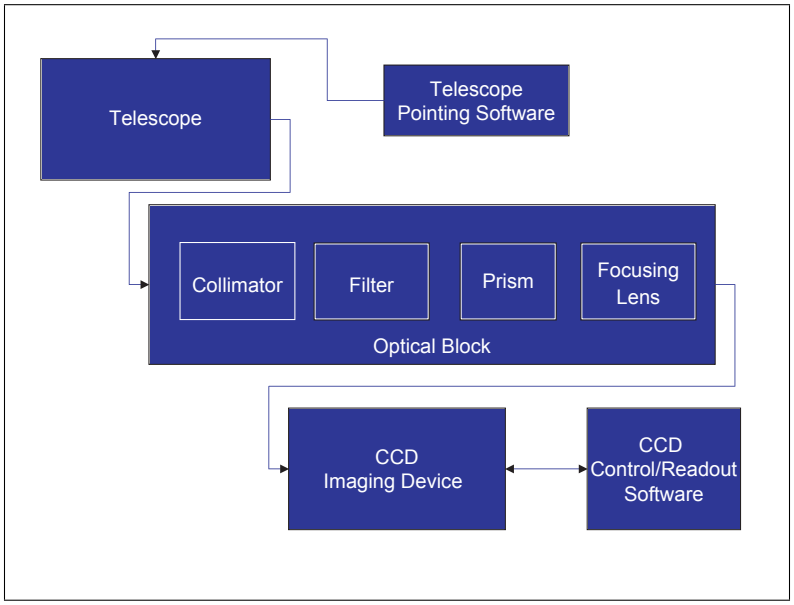

Figure 3.4: Block diagram of the initial design concept.

As the spectrograph is specified to be slitless, the CCD captures an image of a starfield that is dispersed in wavelength. Since the star of interest could appear at any point in the field of view, specific pixels do not map to specific wavelengths. Thus a dynamic wavelength calibration system that characterizes the dispersion of the system and correctly maps pixel to wavelength is required. Such a system relies on Fraunhoffer absorption features in the star itself to serve as a wavelength reference for the acquired data. The accuracy of this calibration method is limited by the low spectral resolution, so a balance is required between the spectral spread in the starfield image and sufficient resolution for accurate measurement of absorption lines in the star. The refinement of the initial concept required the determination of specifications for the three main system components, i.e. the telescope, dispersing optics and CCD. The telescope and CCD must be selected such that exposures of 4^{th} magnitude stars are made in reasonable time ($\sim$ 30 seconds). The design of the dispersing optics requires a balance between the specifications, the calibration method, the physical limitations and component availability.

3.5 Optical Design

The basic optical design used a prism spectrometer to disperse the starfield image prior to imaging on the detector. To avoid, or at least limit, spectrum overlap in the star field image, there must be a relatively small spectral spread on the detector. The spectral resolution of the instrument depends on the spatial size of the spectrum at the detector, the spot size of the star images in the image plane, and physical dimensions of the detector pixels. Large angular magnifications in the system increase the monochromatic spot size and reduce the resolution of the instrument. To avoid spectral overlap in the starfield image while maintaining adequate resolution requires a long focal length collimator. Much of the optical design focused on the development of a long focal length collimator that balances resolution with physical size. A basic ray-tracing model was programmed to aid with the optical design and was used to provide rough-order estimates of the focal lengths and lens separations needed to

achieve the desired collimator focal length while minimizing the physical size of the spectrometer. This model was also used to test the performance of various telescope and spectrometer design combinations and to estimate exposure times. The basic design was optimized with a commercial optics package; this allowed modeling with commercially available components. This process led to minor modifications which allowed the design to use commercially available lenses.

3.5.1 Prism Spectrometer

The optical design is based on the classic concept of a prism spectrometer, consisting of a collimator, a prism for dispersion and an imaging lens that focuses the spectrum onto a detector. It should be noted that the instrument is intended to image several stars per frame, thus the spectrometer design does not include the slit that is commonly found in laboratory and grating-based astronomical spectrometers. In order to achieve a useable spectrum, the optical design must manage its inherent trade-offs. These include,

- Angular magnification (due to the ratio of telescope and collimator focal lengths) vs. monochromatic spot size
- Overall length of the instrument vs. longer focal lengths
- Wavelength per pixel resolution vs. imaging lens focal length and prism apex angle

Angular magnification occurs when the ratio of the telescope and collimator focal lengths is greater than one, Equation 3.1,

$$\mathrm{M} = \frac{\alpha_{\mathrm{col}}}{\alpha_{\mathrm{scope}}} = \frac{\mathrm{f}_{\mathrm{scope}}}{\mathrm{f}_{\mathrm{col}}}, \tag{3.1}$$

where α is the exit angle from the component and f is the focal length of that component. The problem with magnification stems from the fact that diffraction at the telescope aperture and atmospheric turbulence produces a smallest resolvable angle (SRA), which is imaged as a finite spot as opposed to an ideal point, as shown in Figure 3.5. This finite angular size, which is magnified according to Equation 3.1, influences the band-pass of pixels on the imager and, therefore, spectral resolution. To reduce spot size in the image and improve spectral resolution, a longer collimator

focal length, preferably one that approaches the focal length of the telescope is required. However, a 12 inch f/10 telescope has a focal length of approximately 3 m, so a collimator of equivalent focal length is unreasonably long. To accommodate a longer focal length but retain a reasonable instrument length, a compound lens system was designed. The inclusion of diverging lens with a converging lens moves the primary principal planes of the collimator system behind the lenses and reduces the length required between the collimator and the telescope focal plane.

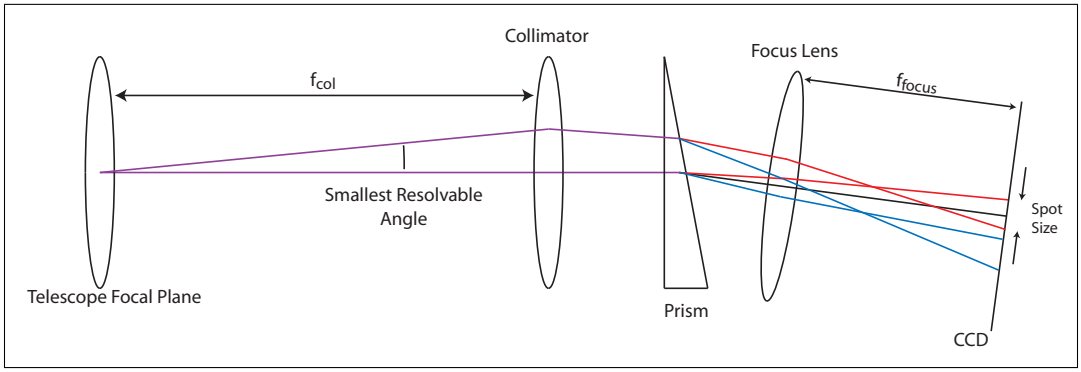

Figure 3.5: Ray diagram showing the prism spectrometer and the effect of SRA on spot size.

The pixel band-pass and spectral resolution are influenced by the monochromatic spot size, prism dispersion and the focus lens focal length. Spot size is directly related to the smallest resolvable angle and the telescope/collimator focal length ratio; this has been optimized through the use of a compound collimator. Prism dispersion affects the angular separation between different wavelengths and the focal length of the imaging lens determines the physical size of the spectrum on the detector. Longer focal lengths, greater angular dispersion and a smaller spot size all contribute to a better resolution. However, longer focal lengths require greater physical size, and greater angular dispersion causes spectral overlap. The spectral resolution must, therefore, be balanced with physical design limitations and other specifications.

3.5.2 Collimator Design

The system was modeled in a general manner using a spreadsheet; this served as a first-pass step in the design process. This custom model allows the different instrument parameters to be varied and the effect on the spectrum recorded. These parameters are:

- Telescope aperture and f/#
- Imaging lens focal length
- Prism apex angle
- Prism orientation angle (relative to optic axis)
- Smallest resolvable angle
- Collimator and integrated diverging lens focal length
- Component diameters
- Wavelength band of interest
- Average incident flux on the telescope aperture

The output from the custom model identifies the optimum configuration for the compound collimator, the estimated exposure times, spectral resolution, and spatial sizes and positions of the 500 nm and 700 nm spots on the detector.

3.5.2.1 Compound Collimator

To minimize magnification and spot size on the detector, a long focal length collimator is required. Single lenses with long focal lengths would necessarily require a very large optical bench. In the interest of minimizing the physical length of the optical bench, the collimator was designed as a two-lens compound system. The concept is shown in Figure 3.6. Focused rays (red) pass from the focal point of the telescope to diverging lens L_1 and converging lens L_2, and emerge parallel. Dashed lines show the focal point. The variable x is the distance from the telescope focal plane to diverging lens L_1. The distance from L_1 to the focal point of converging lens L_2 is v, and the separation between lenses L_1 and L_2 is d.

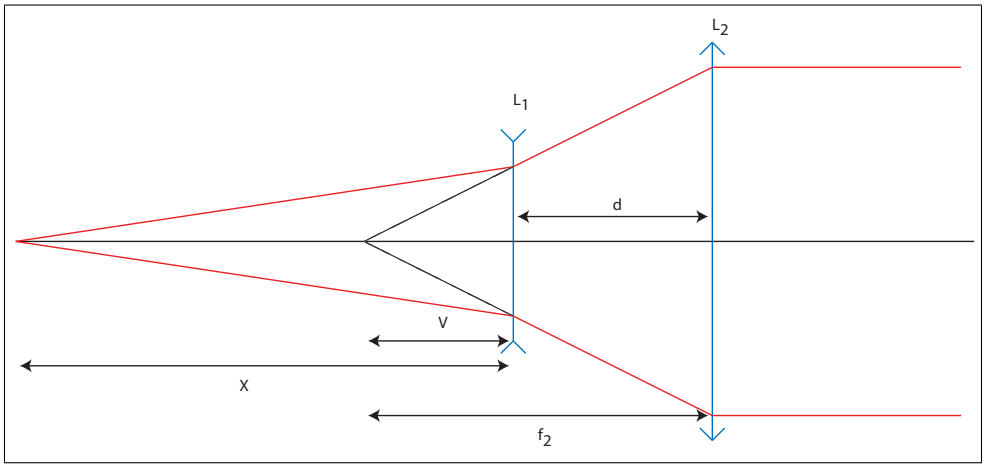

Figure 3.6: Compound lens system used for the collimator, showing the variables used in design.

Gullstrand's Equation (3.2) for the two lens system shown in Figure 3.6,

$$\frac{1}{f_{total}} = \frac{1}{f_1} + \frac{1}{f_2} - \frac{d}{f_1 f_2} \tag{3.2}$$

gives the equivalent focal length of two lenses separated by distance d. Then applying the lensmaker's equation, using the same variables as in Figure 3.6, and constraining the lens separation d such that,

$$d = f_2 + v \tag{3.3}$$

where v is negative, it can be shown that,

$$v = \frac{f_1 x}{x - f_1}. \tag{3.4}$$

Then substituting Equations 3.4 and 3.3 into Equation 3.2 and solving for x and f_2 yields,

$$x = \frac{f_1(d - f)}{d - f_1} \tag{3.5}$$

and

$$f_2 = \frac{-f_{total} f_1}{x - f_1}. \tag{3.6}$$

If the focal length f_1 of the diverging lens and f_{total}, the total focal length of the collimator, are defined the values of x and f_2 can be calculated. The model is used to vary d such that $x + d$ is minimized, thereby minimizing the total length of the

instrument and determining the required focal lengths of the lenses. The relationship between design variables for a 1000mm collimator is shown in Figure 3.7. As the lens separation d is varied, the other variables are calculated such that the specified total focal length is maintained. The focal length f_2 must increase as d increases, however the distance x separating the telescope focal plane from L_2 reaches a minimum. For the case of a 1000 mm collimator, the minimum collimator length, $x + d$, is approximately 27 cm, for a diverging lens of focal length -25.4 mm. The required converging lens focal length is 159 mm and the estimated minimum total instrument length is 52 cm.

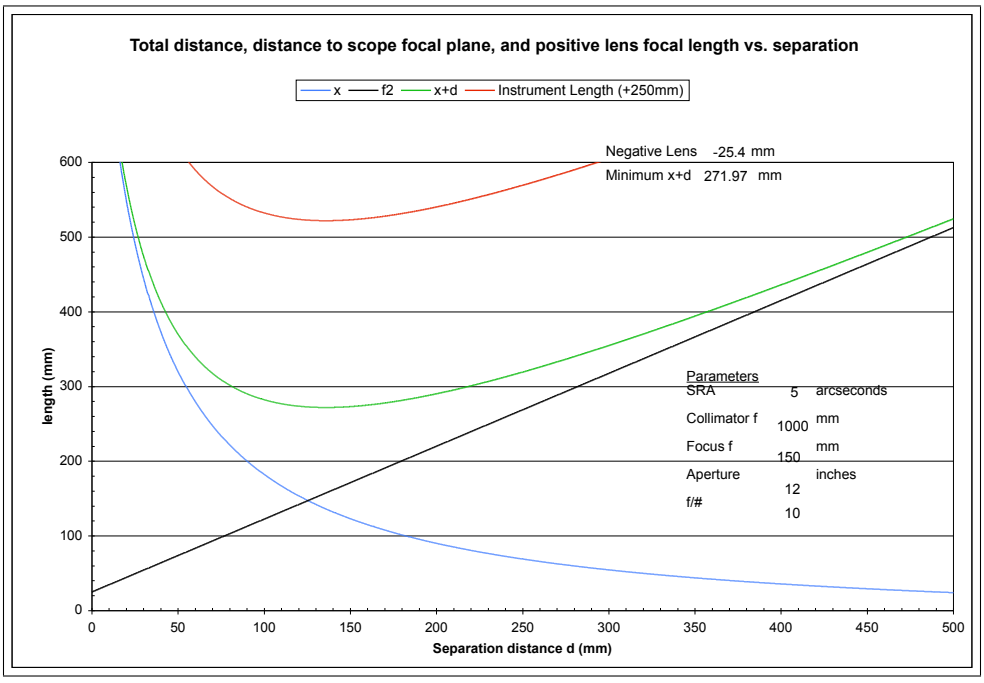

Figure 3.7: Output of the custom model showing the variation of the collimator optical design parameters with respect to lens separation d. The green curve shows the total length of the collimator $x + d$.

3.5.2.2 Pixel Bandpass

Another major feature of the instrument model is the capability to estimate the wavelength band-pass of each pixel in the spectrum, thereby characterizing spectral resolution. This estimate was from the calculation of the proportion of a monochro-

matic spot that is incident on a given pixel. Three assumptions were made to simplify the process:

- The spot is even in intensity across its area
- Every wavelength has an equal spot size
- Only the horizontal width of the spot was considered (1 dimensional calculation)

The pixel size was assumed to be (9 x 9) μm; this matches the Kodak KAF-0400 series CCD that is common in commercial astronomical CCDs. The units of output are the fraction of a pixel covered by the spot. The modeled bandpass of the 500 nm region of the spectrum, for several adjacent pixels, is shown in Figure 3.8. The wavelength dependence of the index of refraction of the prism produces a variable band-pass across the spectrum. At short wavelengths the spectrum is more dispersed and the band-pass is approximately 11 nm/pixel. Conversely for long wavelengths; there is less dispersion and the band-pass increases to approximately 30 nm/pixel.

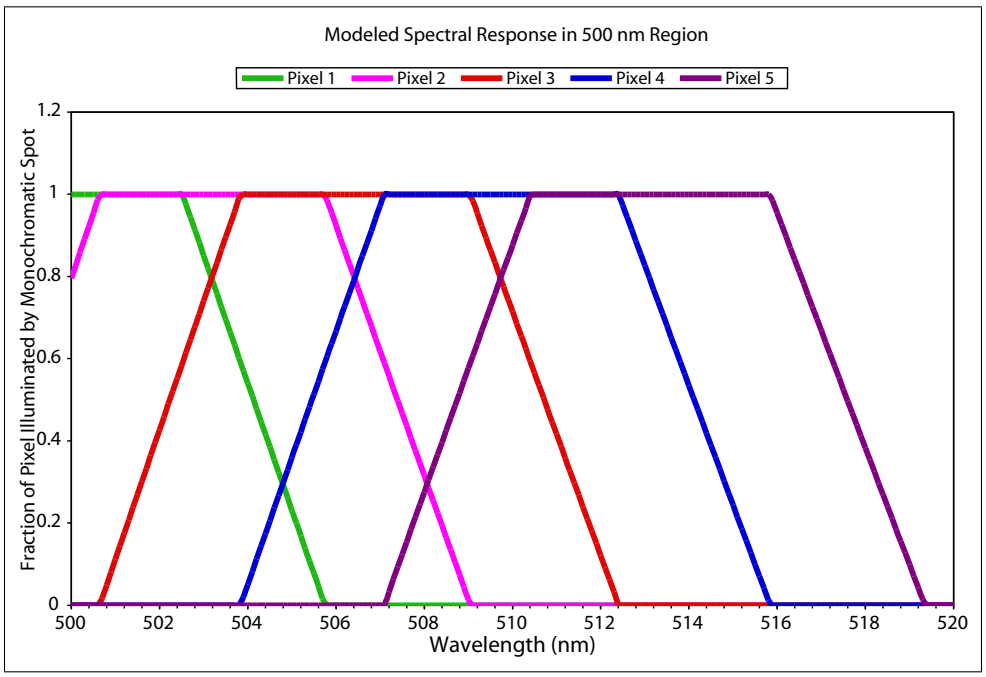

Figure 3.8: Modeled bandpass of pixels in the 500 nm region of the spectrum.

3.5.3 Verification Using a Commercial Optics Package

Verification of the spectrometer design was conducted by modelling the components with a commercial optics package. OSLO-EDU is a ray tracing package produced by Lambda Research Corporation, which includes a comprehensive catalogue of commercially available lenses. In order to examine the effects of aberrations on spot size and resolution, and to verify the lens separations determined with the custom optical model, the prototype optical system design was implemented in OSLO. This modeling showed that minor corrections were required to the lens separations determined with the custom model. Catalogue lenses, which best approximated the focal lengths determined by the custom model, were selected and the design remodeled and optimized using these commercially available lenses.

The effects of chromatic aberration on spot size were also examined. The system was modeled for both singlet lenses and for commercially available achromat lenses of focal length equal to the singlets. It is apparent from the results presented in Figure 3.9 that chromatic aberration has a significant effect on spot size. Therefore achromat lenses were adopted for the final design. The prism dispersion and spectral spread at the CCD chip were in general agreement for the values determined from both the custom and OSLO models. The spot size and spectral spread for several wavelengths in the image plane with achromat lenses is shown in Figure 3.10. The spectral separation from 500 nm to 700 nm is approximately 39 pixels, as compared to 35 pixels as predicted by the custom model. Spherical aberration, which is produced when marginal rays and paraxial rays focus at different distances, was expected to introduce difficulties. For this reason, a lens with an aperture much larger than that of the prism was selected for the focusing lens in an effort to minimize the effects of this aberration.

3.5.4 Final Optical Design

General modelling with the custom optics model and refinement using the commercial optics package led to the final optical design. This design incorporates achromat

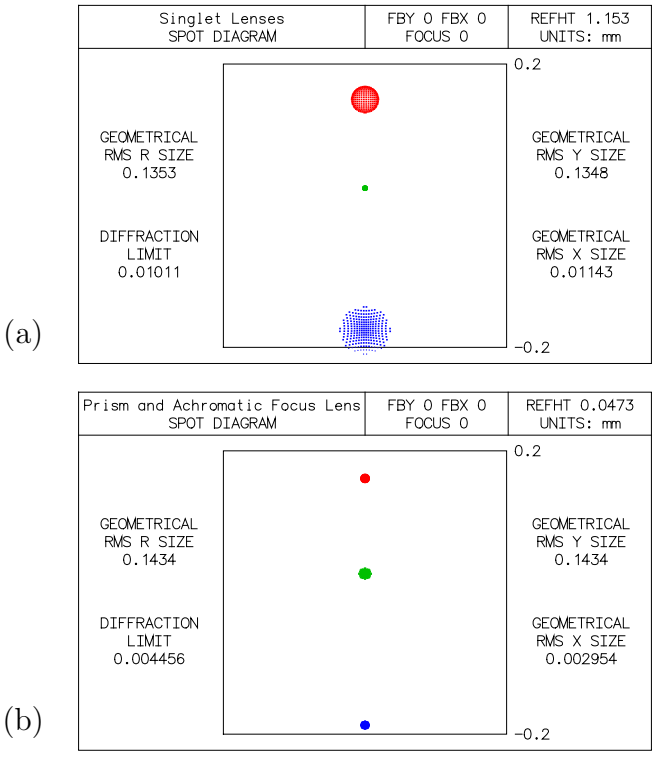

Figure 3.9: Spot diagrams for the instrument produced by OSLO for (a) singlet lenses and (b) achromat lenses. A consistent focus across the wavelength band of interest is achieved using achromatic doublets.

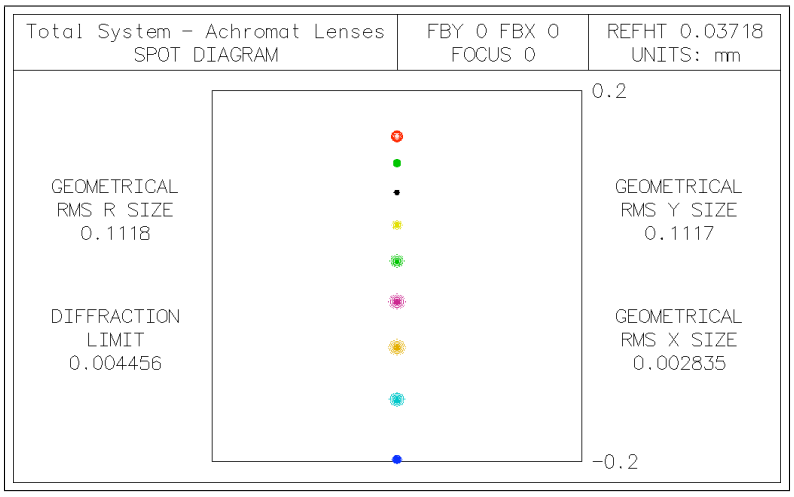

Figure 3.10: Spot diagram showing modeled spectral spread for various wavelengths from 500 nm to 700 nm.

lenses to reduce chromatic aberration, optimized focal lengths and lens separations to minimize the physical length and spot size, and large aperture lenses to minimize vignetting and spherical aberration. The final design is shown in Figure 3.11.

3.5.4.1 Estimated Exposure Times

Once the optical design had been finalized it was possible to determine the telescope best suited to the application. It was found that the average flux in the 500-700 nm band for the spectrum of 4^{th} magnitude star HD032923 [*Burnashev*, 1985] is approximately $110\frac{phots}{s \cdot cm^2 \cdot nm}$. The calculated exposure times for several telescope configurations are listed in Table 3.1. The calculation incorporates the aperture of the telescope, the analogue to digital conversion rate for the common Kodak KAF-0400 CCD chip and assumes a 50% quantum efficiency for all wavelengths. Losses in the optical system due to vignetting and reflection were estimated at 50%. The times indicated are for 85% pixel saturation with a maximum CCD digital number output of 64000.

Table 3.1: Estimated exposure times for a 4^{th} magnitude star and various telescope apertures generated using the custom optics model.

Aperture (inches)	Pixel Area	Exposure Time (s)
12	92.3	23.67
10	82.9	30.62
8	65.7	37.9
7	87.3	65.8

Note: the 7 inch aperture is an f/15 Maksutov-Cassegrain telescope.

3.6 Finalized Design

The final instrument design had to balance the cost of components against the predesign specifications. The telescope must have sufficient throughput, i.e. aperture

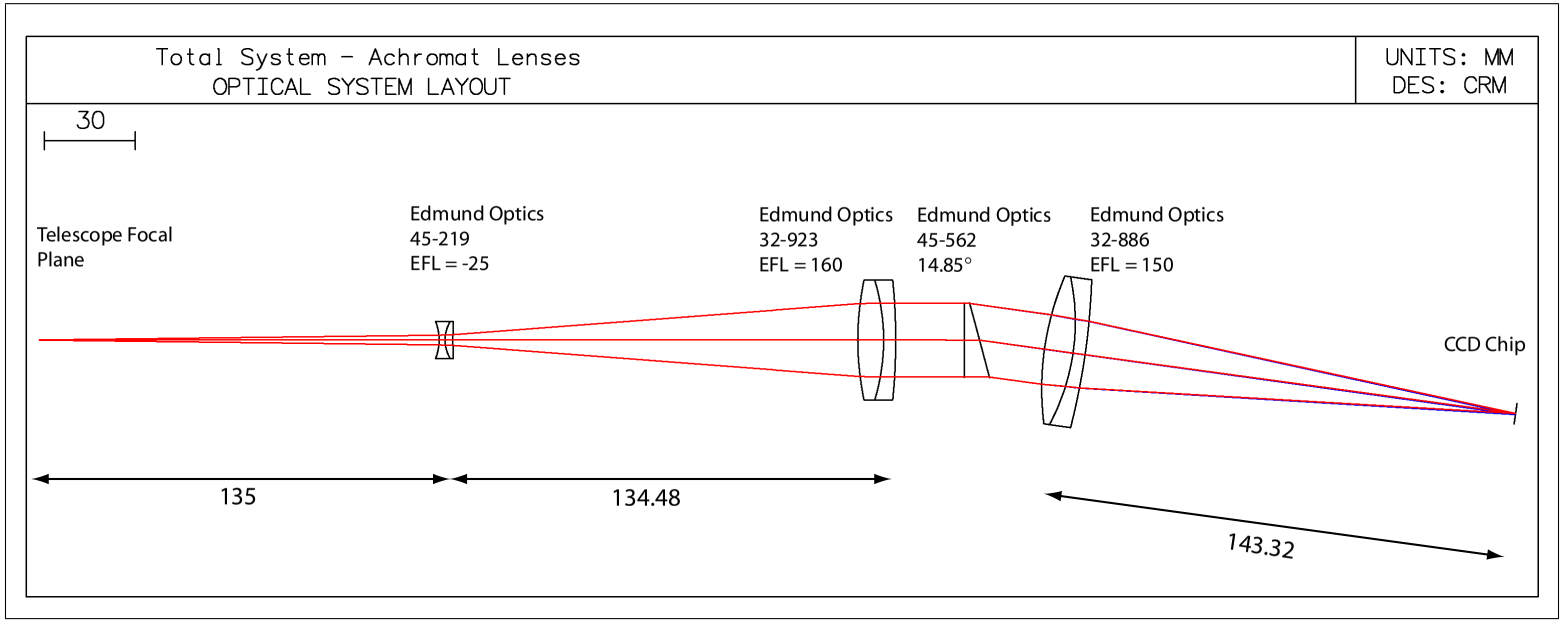

Figure 3.11: Final optical design using achromat lenses.

for light collection, and be sufficiently robust to support the optics and CCD. It must also have automated star tracking ability with a scriptable software interface. The CCD camera selection must consider optical properties, quantum efficiency and software interface. Software interface with commercial products often presents a challenge due to proprietary drivers and widely varying standards. An open-source project called the Astronomy Common Object Model initiative (ASCOM) provides a driver interface between Windows-based scripting languages and a wide variety of astronomical products. ASCOM support was considered a requirement for component selection in order to facilitate software development.

For both ease of use and accurate integrated pointing and tracking ability, the Meade LX-200GPS-SMT series of telescopes is popular with the amateur astronomical community and is supported by ASCOM. This telescope incorporates automated mount calibration and so a permanent pier mount is not a necessity. This makes the instrument portable. In addition, the LX-200GPS-SMT incorporates a feature that removes pointing errors due to mount drive imperfections. This model was, therefore, selected for the prototype. A decision on the aperture is a trade-off between light collection ability (throughput) and price. As shown in Table 3.1, the exposure times are not significantly increased by a reduction in aperture, with a 29% increase in exposure times using a 10 inch model over a 12 inch model. As an added benefit, the lower aperture f/10 telescope has a smaller spot size on the detector due to a more favourable focal length ratio between the telescope and the collimator.

Astronomical CCD cameras are generally used for imaging faint stars and deep field objects. These cameras often integrate two CCD chips into a single detector. One chip is used for exposures while the second is linked to specialized software that is used to auto-guide the telescope and so ensure stable viewing for long exposures of several minutes or more. The Santa Barbara Instrument Group ST-7XMEI CCD package with Kodak KAF-0402ME chip was selected as the imager. The high quantum efficiency, on-chip cooler and microlens technology used in this package improves the signal to noise ratio. As the calculated exposure times are short compared to other astronomical applications, a CCD package without the separate auto-guiding

chip was selected to reduce costs. In addition, the Kodak KAF-0402ME chip is shipped with the MaxIm-DL CCD software package, an industry-standard with a highly scriptable ASCOM compliant interface.

3.6.1 Budgetary Considerations

In addition to the direct costs of equipment purchase, there were costs associated with the design and construction of a physical interface between the telescope and CCD that contains the dispersing optics. The costs for each component are shown in Table 3.2.

Table 3.2: Estimated Costs

Component	Manufacturer	Price($)
Meade LX200GPS-SMT w/UHTC	Meade Instruments	
10”	Corporation	CDN 4150.00
12”		CDN 5700.00
$f_1 = -25.4mm$	Edmund Industrial Optics	CDN 73.25
$f_2 = +159mm$		CDN 129.75
$f_{foc} = 150mm$		CDN 145.38
Prism 14.85°		CDN 34.75
ST-7XMEI CCD Package	Santa Barbara	US 1495.00
	Instrument Group	
Instrument Manufacture	PEP Dept. Machine Shop	CDN 2000.00*
Total (10”)		CDN 8028.12
Total (12”)		CDN 9578.12

* Estimated Price

Assumed 0.75 exchange rate, tax not included

The 10 inch LX200 was the optimum choice. Its smaller aperture is more cost-effective and the shorter focal length allows for a smaller spot size on the imager.

Exposure time benefits were not significant enough to warrant the extra expense associated with the 12 inch model. Actual costs of machining were not significantly different from the estimate, and the total cost of the prototype remained within specifications.

3.7 Mechanical Design and Manufacture

The physical implementation of the optical design required precision alignment and separation of the optical components, minimization of weight, and mechanical interfaces to the telescope and CCD. Physical shape, torque on the telescope, counterbalancing and focusing of the primary telescope mirror and CCD were also design parameters.

The total length of the instrument is approximately 45 cm, from the telescope focal plane to the image plane of the instrument, the CCD chip. A design that extends that distance from the back of the telescope maximizes torque on the telescope drive and limits the minimum observable stellar zenith angle by interfering with the telescope mount. For this reason, a 90° reflecting prism was included, in order to direct the light from the telescope vertically, so that the instrument presents less torque to the telescope. The assembly drawing for the complete mechanical system is shown in Figure 3.12. The design is based upon a solid 1/4 inch aluminum base plate, the optical bench to which the lens mounts were fastened. This solid base plate connected to interfaces to the telescope and CCD. The base plate was contained in an aluminum sheet metal box to protect against external light sources. As the drive motors on the telescope used for automated pointing and tracking cannot sustain the additional torque produced by the optical box and CCD, an adjustable counterbalance system was developed to return the centre of mass of the integrated instrument to the telescope forks (as in Figure 3.12).

A comprehensive weight and balance calculation of the system components in their designed configuration led to a counter-balance mass of approximately 3.2 kg. This weight and balance calculation was based on the position of the centre of mass

of each component in the spectrometer design, which included the base plate, the CCD, the exterior aluminium sheeting, the lens mounts and lenses, the telescope and CCD mechanical interfaces, and the counterbalance system components. The weight and balance calculation was conducted for the telescope tube in both the horizontal and vertical postions, with the counterbalance mass optimally positioned in each case.

The postions of the tap-holes for each lens mount were calculated based on the required separations of the lens vertices in the optical design. This required an accurate characterization of the lens postion within the mount based on the radius of the incident surface of the lens and the aperture of the lens mount. The the heights of the lens mounts required to align each lens vertex with the optic axis were also calculated. A further description of the design drawings used in the manufacture of the mechanical system is presented in Appendix A.

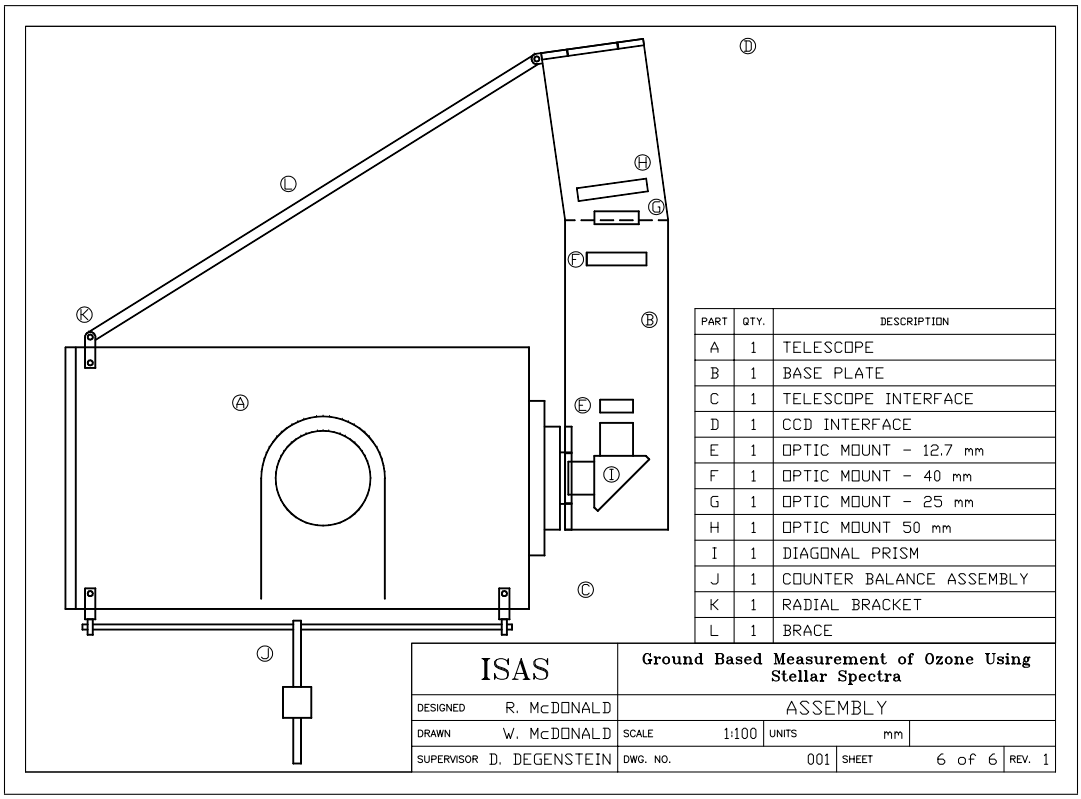

Figure 3.12: Assembly drawing for the mechanical system.

3.8 Instrument Optimization

The completed instrument was field-tested in April 2005. There were several issues evident with the prototype; these included a reduced field-of-view, stray light reflections, aberrations, and noise due to scattered light and dark current. A sample spectrum of Arcturus is shown in Figure 3.13. The grayscale image has been inverted for clarity, the white balance has been adjusted so that pixel values greater than 400 are displayed as black and pixel values of zero are white. The imaging issues are labelled. The relatively small field of view, compared to CCD size, and the high noise value within the field of view are apparent. Thermally generated dark current and bias on the CCD account for the average digital number (DN) value of 100 in unexposed areas of the CCD. Light vignetted by the CCD interface tube is reflected back into the system, and the spectrum itself exhibits aberration.

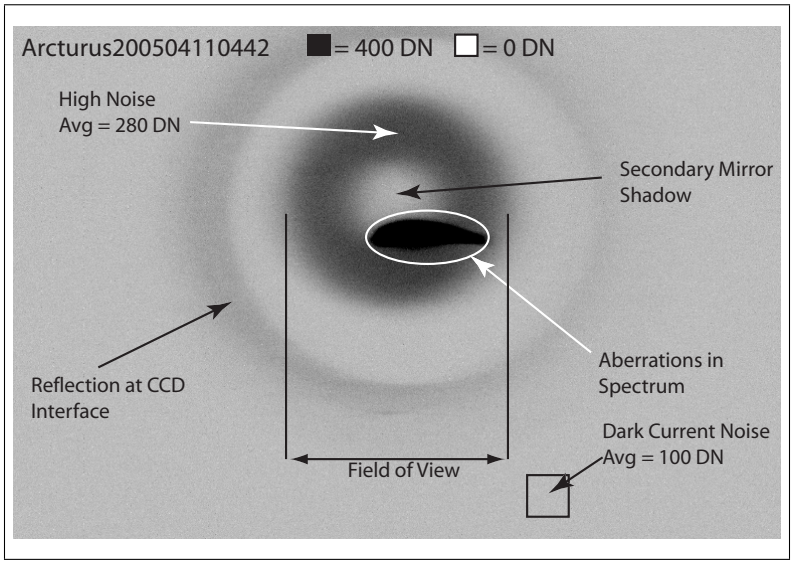

Figure 3.13: Full-frame image of Arcturus showing imaging problems discovered during field-testing. White balance is inverted, and has been adjusted to show stray light. Note the high level of noise within the field of view, the spectrum aberration spectrum and stray light reflections from the CCD interface tube. Typical peak values of spectra are 40000 DN.

Several methods were used to identify and correct the imaging problems shown in Figure 3.13; these included aperture stops, matte black paint, and a software solution for dark current and bias removal. These methods, which are discussed in the following subsections, proved to be very effective and resulted in low-noise spectra without aberrations; an example is shown in Figure 3.14.

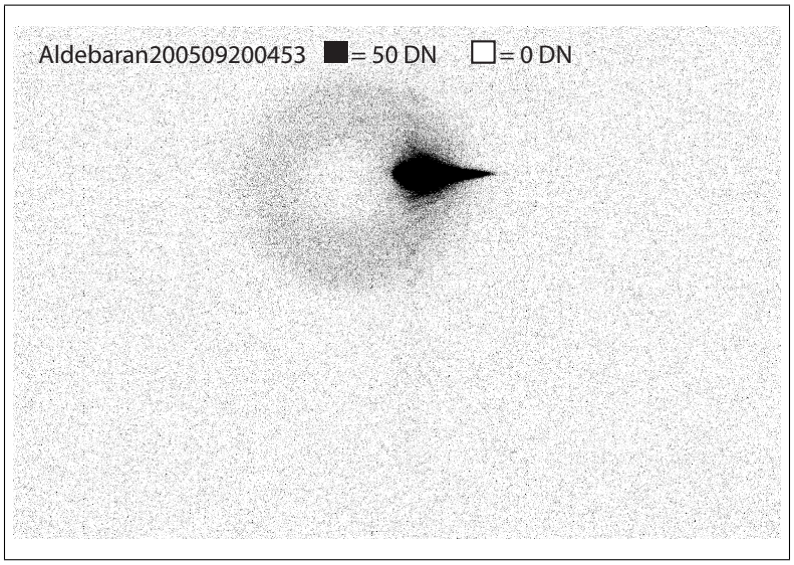

Figure 3.14: Full-frame image of Aldebaran after the correction of imaging problems and dark-current removal. Noise and aberrations are significantly reduced. It should be noted that white balance is reduced to a 50 DN maximum in this image.

3.8.1 Field Of View

The area of the CCD that is exposed to light is much less than the total area of the CCD. As seen in Figure 3.13, the image of the starfield is reduced to a circular shape, with the shadow of the secondary mirror dominating the centre. This effect was unexpected and is due to both the distance separating the telescope focal surface from the physical lenses of the collimator and the telescope interface functioning as a field stop. Confirmation of this interpretation was provided by laboratory-testing the instrument with a laser source. The field stop effect of the telescope can be

seen in Figure 3.15. Off-axis rays are eliminated and so reduce the field of view. A similar stop effect is produced by the diverging lens in the collimator. The small aperture of the diverging lens combined with its distance from the telescope focal plane causes the collimator to intercept mainly parallel rays, while the pupil effect of the telescope interface and right-angle prism reduce the object-height of parallel rays that are allowed to reach the collimator. Thus the shadow of the secondary mirror dominates the image. Because the reduced field of view is inherent to the geometry of the spectrometer design, this problem could not be rectified.

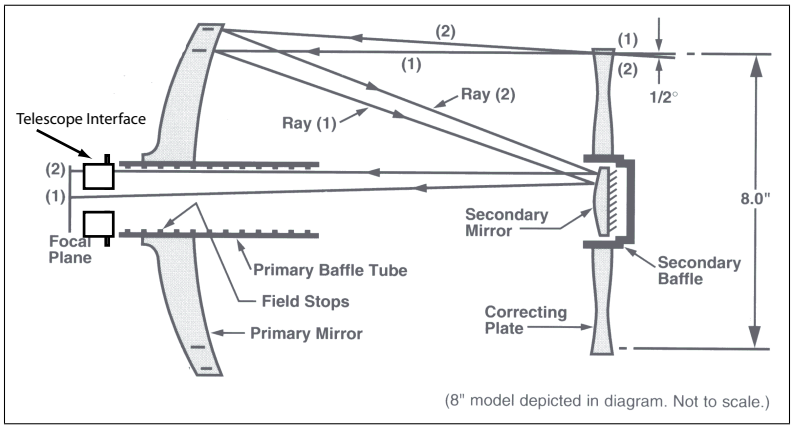

Figure 3.15: The telescope interface acts as a field stop, eliminating off-axis marginal rays. It should be noted that off-axis Ray (2) is stopped by the telescope interface. Light scattered by the telescope interface caused stray light issues by reflecting back into the system from the interior of the interface tube or the secondary mirror. Adapted from *Meade Instruments Corporation* [2003]

3.8.2 Stray Light and Noise Reduction

Field testing of the instrument also revealed significant stray light within the spectrometer. Features such as the large amount of non-thermally-generated noise in the field of view and the vignetted light reflected from the CCD interface tube are indicated in Figure 3.13. The scattered light from the telescope interface that re-enters the system via the secondary mirror or reflections inside the interface tube introduced high noise levels in the field of view. The vignetted light was reflected within the

optical box itself and by the CCD interface tube. This also added noise to the image. To reduce the effect of stray light in the system, the telescope interface, optical box and CCD interface were coated with matte black paint. The "ring effect" produced by the CCD interface, which is evident in Figure 3.13, was reduced. In addition, scattered light reflected from the telescope interface, which accounts for the high noise level in the centre of the frame, was effectively eliminated. There is other noise in the system due to thermally-generated dark current in the CCD itself, as well as the bias applied to the CCD chip for readout purposes. Reduction of dark current effects was accomplished using a software solution. Custom software developed to control CCD exposure times (described in detail in Section 3.9) included a simple dark-current subtraction feature that effectively removes the dark current and bias signals. After each exposure of a stellar spectrum, a "dark frame" was exposed for an equal amount of time with the shutter closed. The dark frame was then subtracted on a per-pixel basis from the stellar spectrum frame, so removing the majority of signal from the bias and dark current. The combination of stray light and dark current removal significantly reduced noise in the image. Thermally-generated noise in unexposed areas of the CCD was reduced from 100 DN to an average of 2.7 DN, while the noise in the field of view was reduced from 280 DN to an average of 10 DN. The reduced noise levels can be seen from a comparison of the high noise areas in Figure 3.16(a) with the corresponding corrected image in Figure 3.16(b).

3.8.3 Aberration Effects

The spectra of stars observed in the field trial exhibited a focus-shift in the direction of dispersion. This effect, which is shown in Figure 3.17, suggests coma aberation or distortion. Since both of these aberrations arise from differences between marginal and central rays, aperture stops were considered as an effective way to reduce the effect. It was determined that the diverging lens in the collimator was the source of the aberration, and 7 mm aperture stops were applied to the converging lens in the collimator as well as to the focusing lens. The results of these aperture stops on a sample spectrum from a mercury gas lamp are shown in Figure 3.18. White balance

(a)

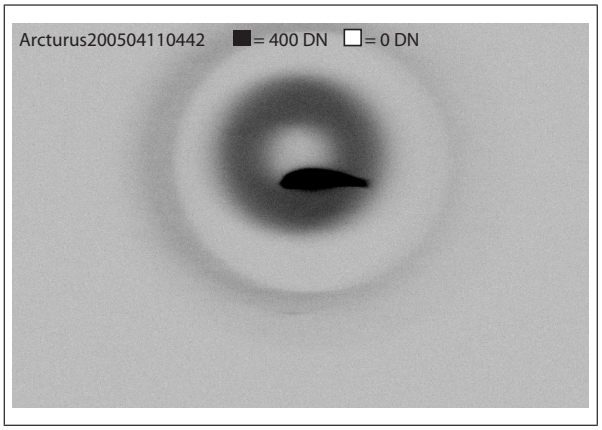

(b)

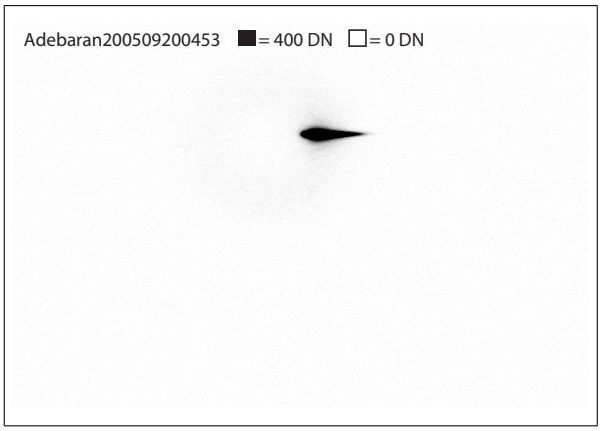

Figure 3.16: (a) A test spectrum of Arcturus showing stray light features. (b) A spectrum of Aldebaran shows reduced stray light and noise features after the application of the matte black interior and dark current removal. Both frames have equivalent white balance.

was adjusted to show all light incident on the CCD. The better focus achieved with the stops is readily apparent.

3.9 Software Development

Software to control both the telescope and the CCD was written using the Python language. This software relies on the Microsoft Windows Common Object Model (COM) interface as well as control methods from the open-source ASCOM initiative to script both the telescope and CCD.

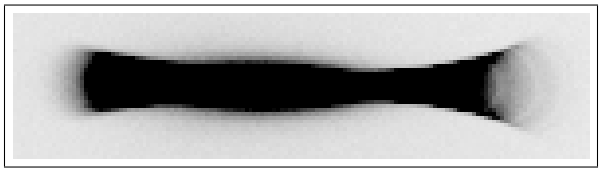

Figure 3.17: Spectrum of Vega showing coma or pincushion distortion.

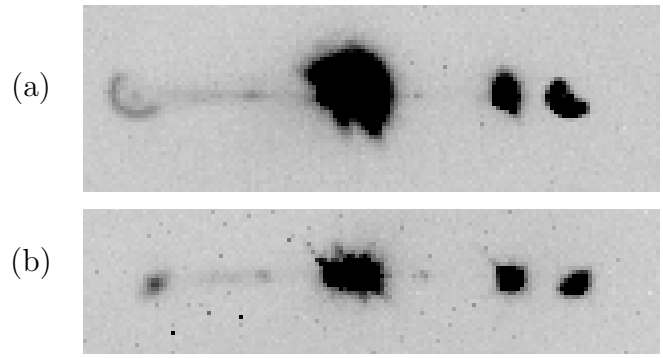

Figure 3.18: (a) Aberrations in an Hg spectrum cause focus-shifting and an increase in spot size. (b) Spot size and uniform focus is achieved with aperture stops. White balance is inverted and adjusted to show all light incident on the CCD.

3.9.1 Telescope Control

Software control of the telescope is achieved through an RS-232 interface between the telescope and a controlling computer. ASCOM methods are used to seamlessly access control functions in the telescope electronics without the need for low-level use of serial port functions and esoteric telescope control commands. In addition, the United States Naval Observatory Astrometrics program NOVAS-COM was used for astrometric calculations. NOVAS-COM is used to calculate altitude and azimuth information for a star of interest, it employs data for both the star and the observing position on the Earth. Given proper manual calibration of the telescope mount, the control program *TelescopeControl* is capable of automatically tracking a single star and making regular exposures for the duration of a user selected time interval, with user defined exposure delays.

3.9.1.1 Program Structure

The structure of *TelescopeControl* is simple but is designed for expandability. A program flow diagram for *TelescopeControl* is shown in Figure 3.19. After manual calibration of the telescope mount, software interfaces with the telescope and CCD are established. A GPS position is acquired from the telescope and entered into a NOVAS-COM *Position* object. User-entered star data are loaded into a NOVAS-COM *Star* object and the altitude-azimuth coordinates of the star are calculated and sent to the telescope. The telescope then tracks the star of interest for the remainder of program operation. While the star of interest is tracked by the telescope, the CCD is exposed at regular, user-selected intervals using routines discussed in Section 3.9.2. The program was designed so that automated star selection would be possible. Given a user defined database of stars of interest, the program could be expanded to observe any number of stars during one night of operation.

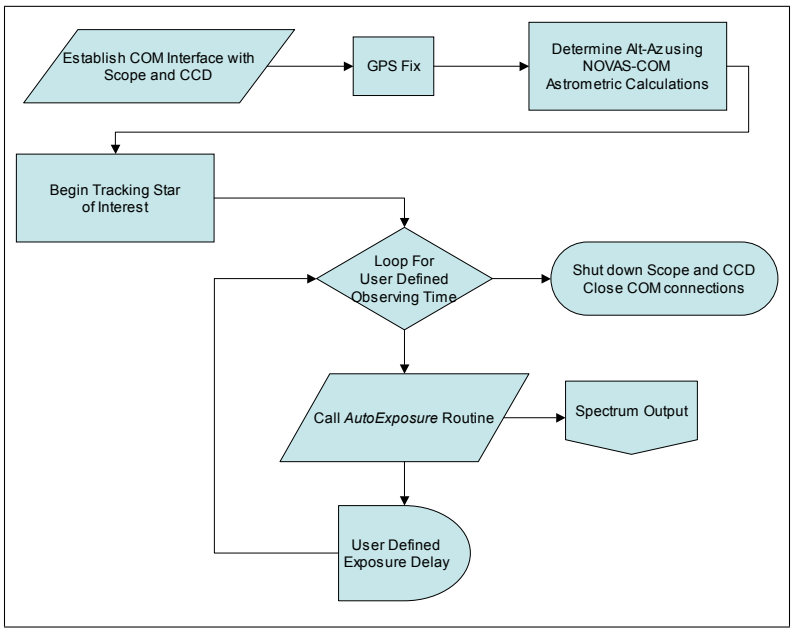

Figure 3.19: Program flow diagram for the telescope control program.

3.9.2 Camera Control

CCD camera control is accomplished by scripting the MaxIm-DL CCD control program. MaxIm-DL is a fully scriptable ASCOM-compliant commercial program for controlling astronomical CCDs as well as for downloading and manipulating images. Custom Python routines are called by the *TelescopeControl* program to acquire light and dark exposures and to remove dark current. Images are saved in astronomy-standard FITS format for later processing. As a first stage in data processing, custom routines were also written to automatically generate orthogonally-binned profiles of acquired spectra.

3.9.2.1 Auto-Exposure Routine

An auto-exposure routine was written that automatically adjusts the exposure time to acquire an image with a maximum pixel digital number value that falls within a user-defined range. This eliminates the need for manually determining the exposure time (t_{exp}) required for a certain star, and also avoids over-exposure. The use of this technique is valuable if *TelescopeControl* is expanded to observe multiple stars in one observing period. A program flow diagram for the auto-exposure routine is shown in Figure 3.20. *AutoExposure* takes a base exposure at the minimum t_{exp} allowed by the camera, and iteratively exposes until the maximum pixel value falls within the user-defined range. A dark frame is then exposed at the same exposure time and subtracted from the light frame for the purposes of removing dark-current and bias from the image. The image is then saved to a FITS file. The filename for the image contains the star name, date, time, and t_{exp}. The entire auto-exposure process takes approximately $2 \cdot (t_{exp}) + 5$ seconds to complete.

In addition to saving the file, a secondary routine *SpectrumToArray* is called by *AutoExposure* as a first stage in data analysis. All light from the star does not necessarily fall on a single row of pixels; this is due to the optics and the alignment of the star on the CCD. Selection of only the brightest row in the spectrum loses information and is prone to errors due to hot pixels or cosmic ray hits. A process

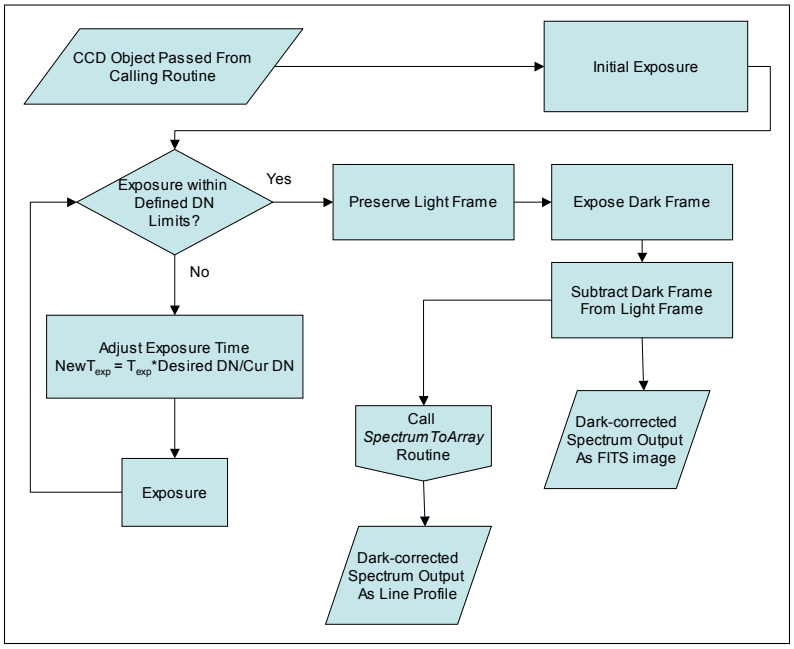

Figure 3.20: Program flow diagram for the *AutoExposure* routine.

called *orthogonal binning* is used compress the spectrum into a line profile without losing information. The spectrum is dispersed along the rows of the CCD. By summing the pixel values orthogonal to the direction of dispersion and using the sum as the line profile, all the information provided by the incident light is collected and the effects of bad pixels are minimized. The concept of orthogonal binning is shown in Figure 3.21. The procedure *SpectrumToArray* is used to produce orthogonally binned line profiles from spectral image frames. *SpectrumToArray* isolates the 10 rows of the CCD image centered on the spectrum, and sums the digital numbers in all columns, this produces a line profile of the spectrum in the direction of dispersion. This line profile is then saved as a text file containing digital number versus pixel number; this file can be accessed for later wavelength and intensity calibration. The *SpectrumToArray* routine currently only functions on the brightest star in the field of view.

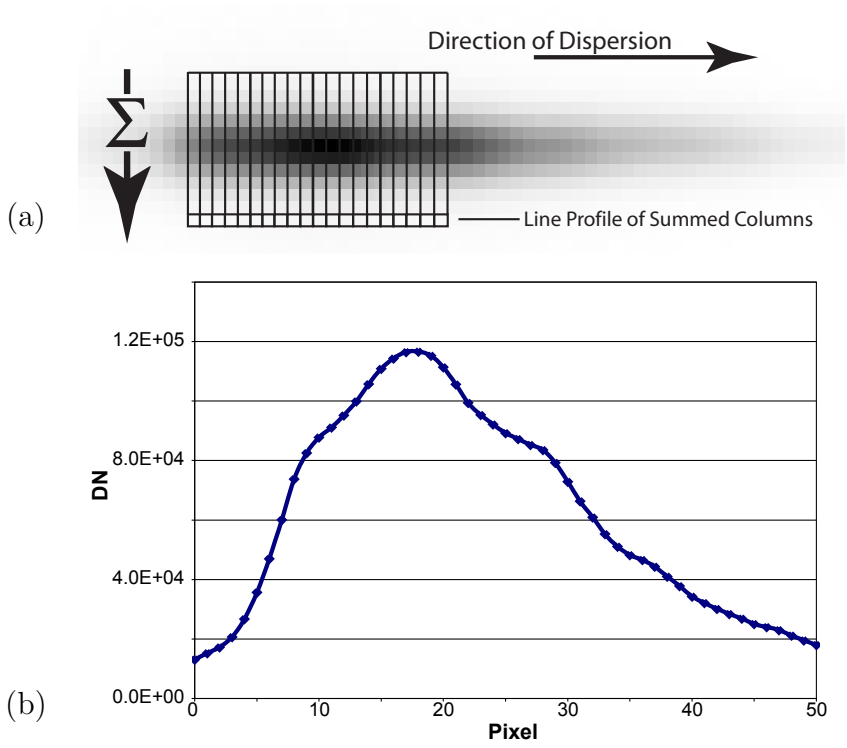

Figure 3.21: Orthogonal binnning. (a) The pixel values of the spectrum are summed perpendicular to the direction of dispersion. (b) The summation produces a single line profile representing the entire spectrum.

3.10 Conclusion

The progression from concept to prototype and initial testing involved many engineering aspects, these included optical design and optimization, management of physical parameters, budget, and software design. After field testing and mitigation of several design problems, the instrument was calibrated and used for data collection. The completed instrument is pictured in Figure 3.22.

Figure 3.22: The completed instrument ready for operation.

Chapter 4

Calibration

4.1 Introduction

Calibration is the characterization of the response of an instrument to the signal that it measures. The general calibration method involves the use of a known quantity as input and the observation of the output from the instrument. The difference between the known input and the instrument output characterizes the instrument response; this can be used to determine an unknown input by removing the instrument response from the observation. Two forms of calibration were required for the present work. As the instrument is a stellar spectrometer, the purpose is to measure the intensity of light at various wavelengths. Therefore, measurements made by the instrument must be calibrated with respect to both *wavelength* and *intensity*. The slitless nature of the instrument requires a dynamic wavelength calibration scheme. The actual analysis technique to determine ozone number densities only uses intensity ratios (Equation 2.25), so it is only necessary to have a relative intensity calibration.

4.2 Star Simulator

Calibration required characterization of both the dispersion properties and intensity response of the spectrometer in a laboratory setting. In both cases, there is a significant problem associated with providing a known input due to the small angular size of stars. An average night of seeing yields stars with an approximate angular size of 5 arcsec. Any laboratory source that did not provide an object size of $\sim$5 arcsec produced an over-sized spot that mixed the spatial data and spectral data and so de-

graded resolution. Several set-ups using various lens configurations were investigated as a possible star simulator. The only successful configuration used a small 0.53 mm aperture placed approximately 25 m from the instrument. This configuration yielded an angular size of 0.00121°, or 4.4 arcsec. Emission gas lamps, interference filters illuminated by a 12 V tungsten-halogen lamp, or a tungsten intensity calibration lamp were used to provide the known inputs. The light from these sources that was transmitted by the 0.53 mm aperture was imaged by the instrument. The actual star simulator apparatus is shown in Figure 4.1. Although the 0.53 mm aperture

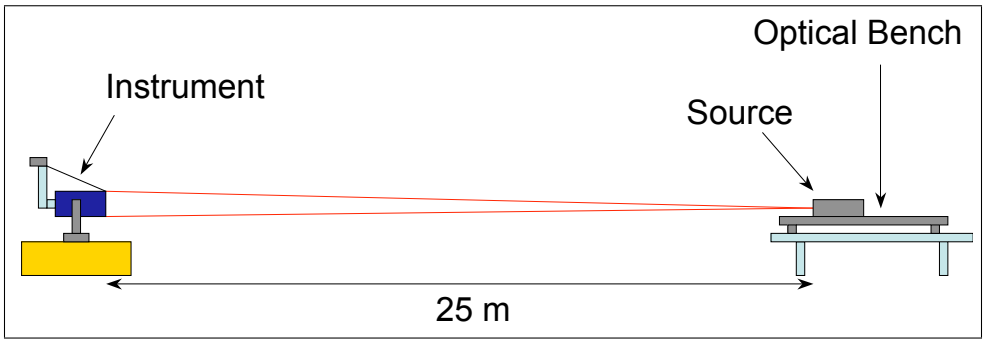

Figure 4.1: The star simulator apparatus used for both wavelength and intensity calibration. Light from emission gas lamps, interference filters illuminated by a 12 V tungsten-halogen lamp, or a tungsten intensity calibration lamp passed through a 0.53 mm aperture and was imaged by the instrument.

used in the star simulator had a nominal angular size that is less the 5 arcsec average star size, the actual spectra produced by the simulator are larger than those produced by stars. This degradation in resolution was due to the geometry of the simulator. A point source at 25 m from the objective of the telescope produces a maximum incident angle of approximately 0.58° at the telescope aperture, which is a poor approximation to the nearly collimated light observed from stars.

4.3 Wavelength Calibration

Wavelength calibration of the instrument is required so that the observed intensities can be associated with specific wavelengths. In many spectroscopic instruments, the geometry of the source, the dispersing element and the imager is constrained so that specific wavelengths map to particular pixels. These instruments include a slit, which transmitted the incident light, effectively producing a point source at a fixed distance from the optics. This technique produces a rigid wavelength-to-pixel map, that is easily characterized. The disadvantage of this technique in stellar spectroscopic applications is that the telescope guiding must be sufficiently accurate to maintain the star image on the slit. The prototype developed in the current work is different; it images a star rather than a slit. While the former design decreases the need for extremely accurate telescope guiding, the variable geometry of the source, dispersing element and imager creates a different wavelength-to-pixel map for each star in the image and for each exposure, if the star field is not accurately followed.

Since the wavelength-to-pixel mapping for a slitless spectrometer is completely variable, the pixels themselves cannot be used as a wavelength reference. Therefore, if the traditional wavelength calibration concept is applied to a slitless spectrograph it is necessary to generate a wavelength-to-pixel map for each exposure. Known spectral sources can be used to characterize the dispersion in the system, but a reference wavelength is still required for each spectrum, in each exposure, to produce a wavelength-to-pixel map for that spectrum. Fraunhoffer absorption lines in stellar spectra provide the necessary spectral references for a dynamic wavelength calibration system.

4.3.1 Wavelength Calibration Procedure

As noted above, a slitless spectrograph requires a dynamic wavelength calibration scheme, where a feature of known wavelength within the spectrum and the instrument dispersion are used in combination to calibrate the entire spectrum. The dynamic wavelength calibration that was implemented with the present instrument

required characterization of the dispersion of the system. This was accomplished using gas lamps and interference filters. The instrument is designed such that the x-axis of the CCD array is aligned in the direction of dispersion; this ensures that the spectrum orientation is constant. A general spectrum imaged by the slitless spectrograph has a constant spectral width, which is defined by the dispersion, but is imaged at an arbitrary x-position on the CCD. The concept is illustrated in Figure 4.2, where a spectrum can have bounding pixels x_n and x_{n-1} depending on its position in the field of view, but the spectral width is always $\Delta x = x_n - x_{n-1}$. With no physical correspondence between specific pixels and wavelengths, the approach was to create a virtual standard wavelength-to-pixel map from a knowledge of the spectrometer dispersion. The virtual standard wavelength-to-pixel map was generated from the laboratory measurements with the star simulator, and is known as *standard pixel space*.

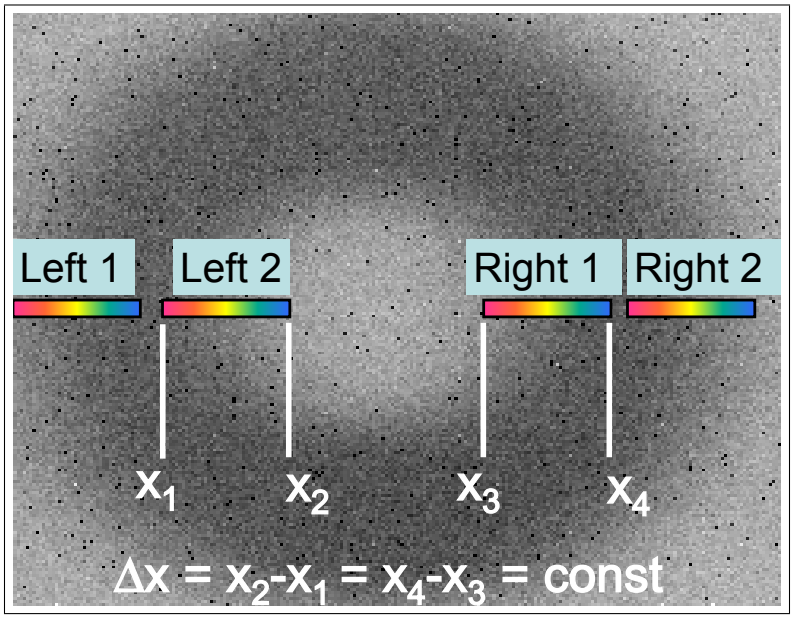

Figure 4.2: The spectral positions of the four trials used to characterize the dispersion. A general spectrum maintains the same spectral width Δx, but the starting pixel x_n is arbitrary.

The process of calibrating a spectrum involves three steps. First, the wavelength

of the known spectral feature is mapped to standard pixel space. The difference between the position of the feature in standard pixel space and its arbitrary pixel position on the CCD is equivalent for all wavelengths in the same spectrum, and allows for the entire spectrum to be linearly shifted into standard pixel space. As a final step, the inverse of the virtual standard wavelength-to-pixel map is used to map the shifted spectrum from standard pixel space back to wavelength. The calibration concept is illustrated in Figure 4.3.

4.3.2 Results

Before collecting calibration data, the Oriel Optics #57200 interference filter was used to focus the telescope and CCD. This filter has a central wavelength of 589 nm and a FWHM of 10 nm and was chosen due to its proximity to the peak absorption in the Chappuis band. The star simulator was then used with emission gas lamps and interference filters to generate images with known spectral features. These data were used to quantify the spectral dispersion on the CCD with a least-squares 3^{rd} order polynomial fit. This polynomial served as a pixel-to-wavelength map, and its inverse as a wavelength-to-pixel map. Errors in the calibration were quantified and error correction was added as a final step in the calibration procedure.

Data collection was primarily conducted with emission gas lamps and by taking successive exposures, for each lamp, without changing the geometry of the star simulator. This combination of exposures effectively produces a broad spectrum with identifiable specific wavelength peaks. The centroid of each peak was calculated in order to determine its fractional pixel position. The spectrum was then analysed to determine the pixel separation between wavelength peaks. The pixel separations from these data were then generalized by fitting a polynomial. Mercury, Zinc, Helium and Neon lamps, that have spectral lines between 4358.3 Å and 7065.2 Å were used to provide data over the region of interest, namely 5000 to 7000 Å. This procedure was followed for several points across the field of view in order to account for any variation in dispersion for off-axis objects. The longest wavelength peak was selected as the arbitrary "zero" pixel for the virtual standard pixel space. The data

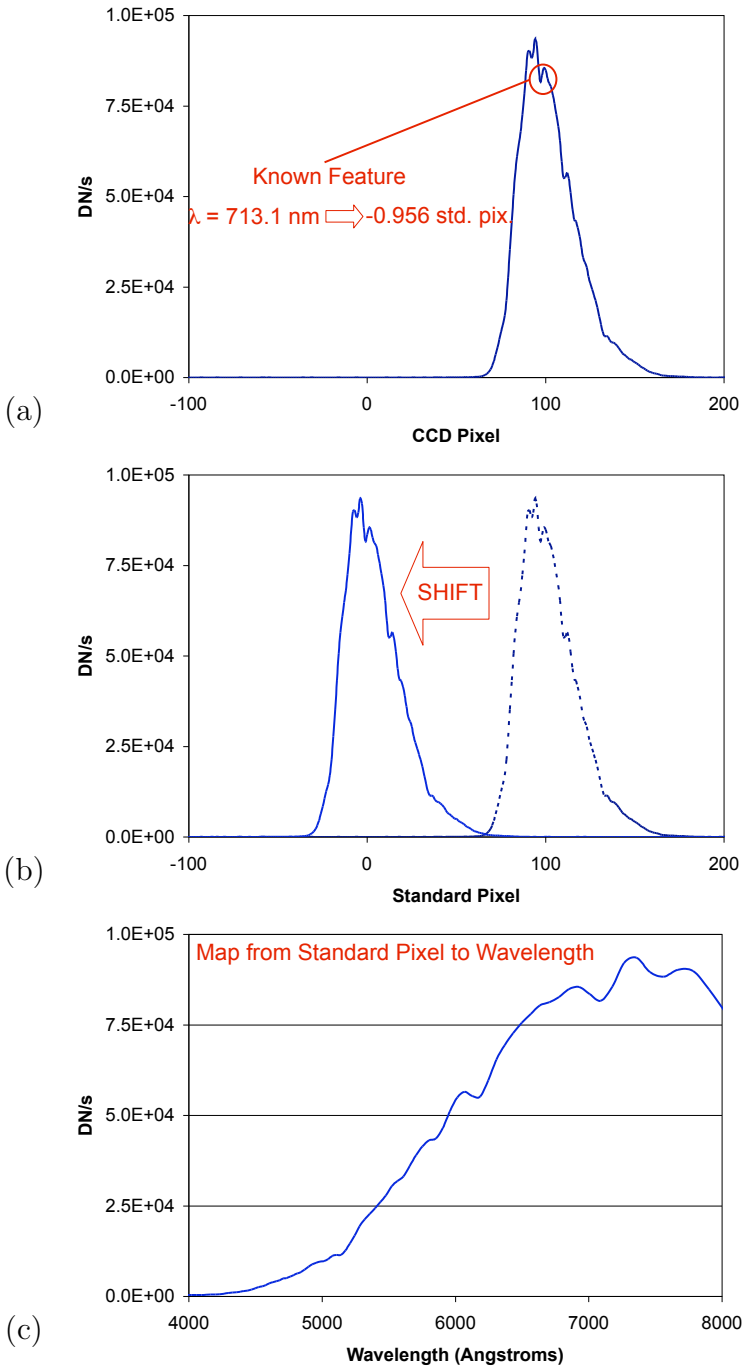

Figure 4.3: The concept of the dynamic wavelength calibration. (a) A known spectral feature is mapped to *standard pixel space*. (b) The spectrum is shifted from its arbitrary pixel location to standard pixel space. (c) The entire spectrum is mapped from standard pixel space to wavelength.

from four sets of measurements, as well as the average dataset, are summarized in Table 4.1.

Table 4.1: Data collected with the star simulator were used to characterize the dispersion of the instrument. Four sets of measurements were made across the field of view of the instrument, with the average being used for the calibration. Standard pixel values of the peak wavelengths are shown for each each trial.

Peak (Å)	Gas	Left 1	Left 2	Right 1	Right 2	Average
4358.33	Hg	64.89	64.94	63.41	64.30	64.38
4722.15	Zn	51.01	50.10	48.16	49.58	49.71
4810.53	Zn	47.88	46.68	44.98	46.48	46.51
5460.74	Hg	27.36	27.62	26.49	26.80	27.07
5780 *	Hg	20.46	20.54	19.57	19.65	20.06
5875.62	He	18.42	18.60	17.79	18.09	18.22
6362.34	Zn	10.73	9.91	8.76	9.89	9.82
6402.25	Ne	9.57	9.57	8.12	8.65	8.98
6678.15	He	4.92	5.05	4.67	4.63	4.82
7065.20	He	0	0	0	0	0

* average of blended line pair at 5770 and 5790 Å

4.3.2.1 Average Calibration

The average of all four measurements across the field of view was used to fit a 3rd order polynomial. This polynomial, and its inverse, were used to calibrate the collected stellar data. A graphical representation of the data and the fit is shown in Figure 4.4. The wavelength-to-pixel polynomial was derived from the acquired data,

$$p = -1.297 \cdot 10^{-9}\lambda^3 + 2.806 \cdot 10^{-5}\lambda^2 - 2.151 \cdot 10^{-1}\lambda + 5.761 \cdot 10^{2}, \tag{4.1}$$

where p is the pixel position and λ is the wavelength (Å). Equation 4.1 is used to transfer the known feature wavelength to the virtual standard pixel space. The

difference between the pixel positions of the known feature in the standard pixel space and on the CCD is then used to shift the entire spectrum into standard pixel space. The shifted spectrum is then converted from standard pixel space to wavelength using the inverse of Equation 4.1, which describes the pixel-to-wavelength conversion,

$$\lambda = -5.478 \cdot 10^{-3}\mathrm{p}^3 + 9.512 \cdot 10^{-1}\mathrm{p}^2 - 8.068 \cdot 10^{1}\mathrm{p} + 7.059 \cdot 10^{3}, \qquad (4.2)$$

where λ is the wavelength and p is the pixel position in standard pixel space. Equation 4.2 was derived by using Equation 4.1 to produce a series of sample data, inverting the data and fitting a polynomial to the inverted data.

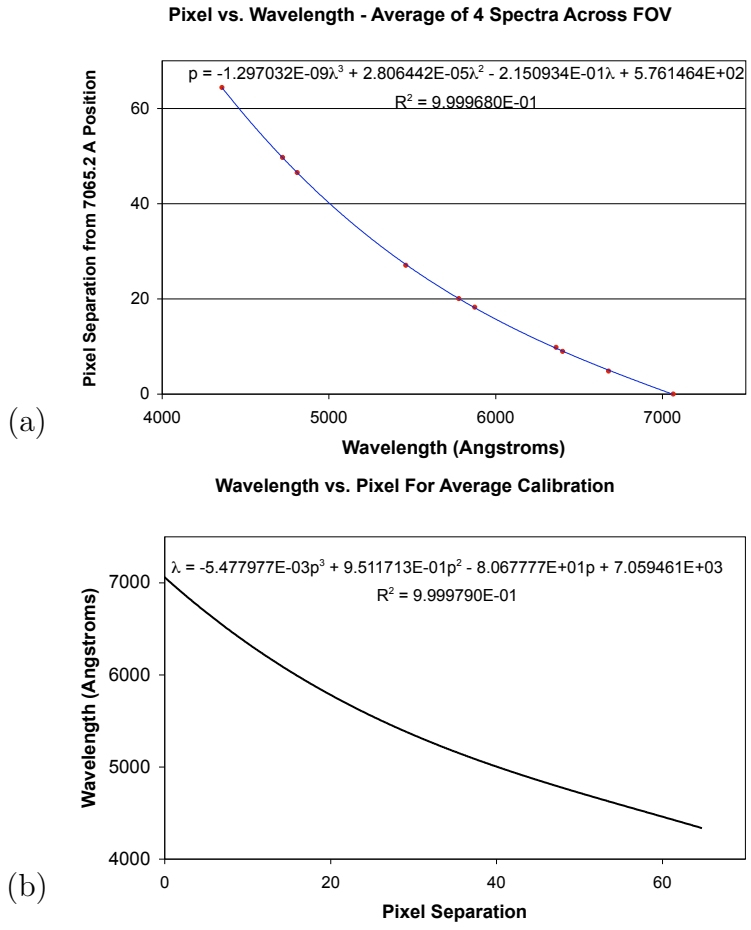

Figure 4.4: The calibration polynomials used to produce the average calibration. (a) The gas lamp data (red) and its least-squares polynomial fit. (b) The empirically derived inverse of Equation 4.1.

The average values derived from the gas lamp data provide only an approximate

calibration, as it is limited to the wavelengths of the gas lamps. A sample calibrated Hg gas lamp spectrum is shown is Figure 4.5(a). The calibrated wavelengths of the peak centroids and the actual feature wavelengths are indicated. It is apparent from this example that there is significant wavelength difference associated with the calibration. This difference is due to the "pixelated" nature of the detector so that the signal from a range of wavelengths is integrated on each pixel. The signal from a particular single-wavelength feature will depend on its position on the pixel and so may have a centroid that is removed from its true position.

The "error" in the calibration polynomials (Equations 4.1 and 4.2) was quantified by using both equations with an assumed set of "known" wavelengths. An assumed known wavelength was transferred to standard pixel space using Equation 4.1 and then converted back to wavelength using Equation 4.2. The difference between the original known wavelength and the calibrated wavelength quantifies the "error". This process was completed for wavelengths between 4000 Å and 8000 Å, and yielded a measure of the calibration "error" by wavelength, which is shown in Figure 4.5(b). Typical values within the region of interest are ± 10 Å. The quantification of the calibration error allowed a correction procedure to be included in the wavelength calibration process; this procedure subtracts the error from the calibrated wavelengths and gives a well calibrated spectrum for wavelengths between 4000 Å to 8000 Å.

The calibration process, including error correction, was implemented in the IDL programming language and used to automate spectral calibration. Orthogonally binned spectra produced by the camera control and readout software are efficiently and accurately calibrated using this process. A wavelength-calibrated measured spectrum of Aldebaran acquired by the instrument is compared to a catalogue spectrum [*Burnashev*, 1985] in Figure 4.6. As expected, the high resolution catalogue spectrum is smoothed by the low resolution instrument. This low resolution smoothing is adequate to observe the Chappuis absorption band, although there is the disadvantage of a decrease in the accuracy of determining the factional pixel location of the Fraunhofer feature used for the calibration shift. However, the calibration is sufficiently accurate in the region of interest, the Chappuis band.

(a)

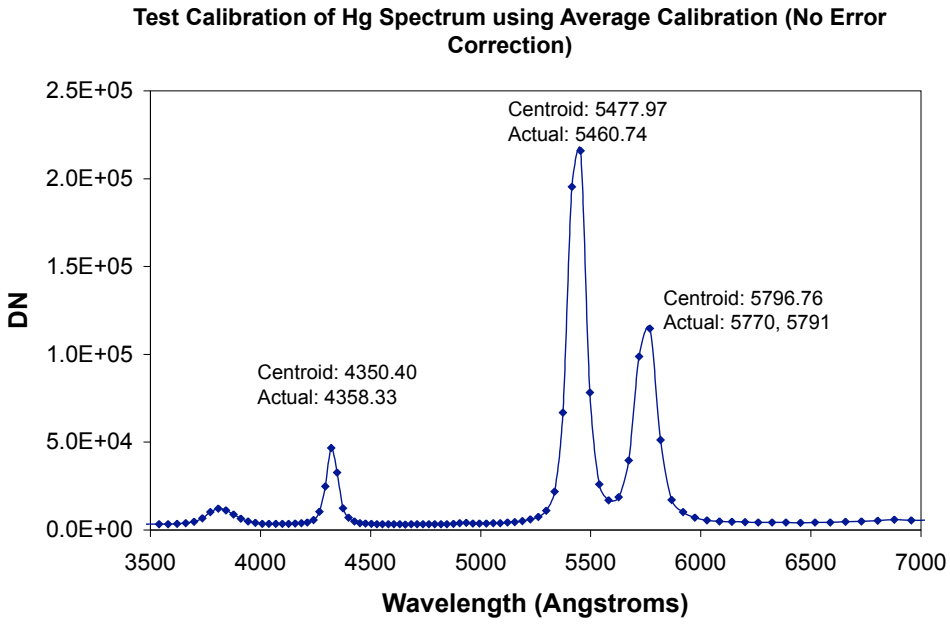

(b)

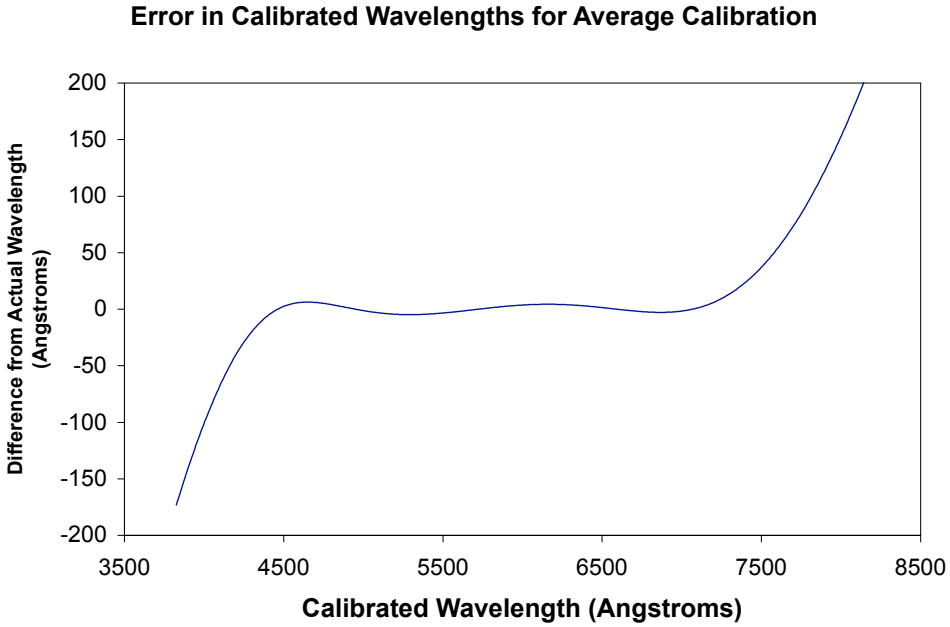

Figure 4.5: The error in the wavelength calibration due to the use of a 3rd order polynomial. (a) Test calibration of an Hg gas lamp spectrum. Note the error between the centroids of the calibrated peaks and the actual wavelengths of the spectral lines. (b) The error in the average wavelength calibration. This error is minor in the region of interest but becomes significant outside the 5000 to 7000 Å band.

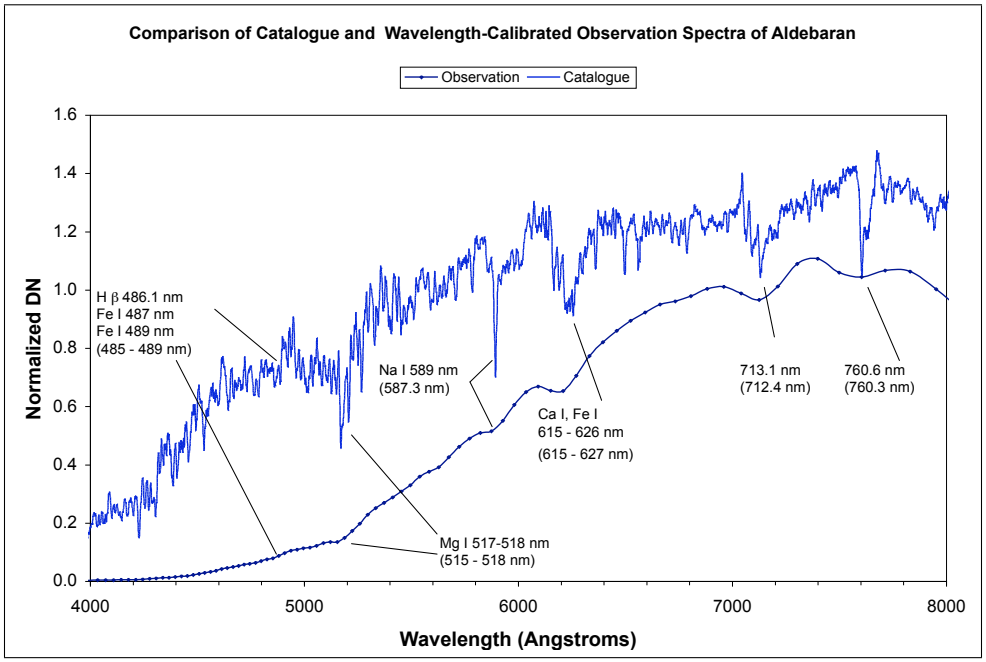

Figure 4.6: A comparison between a catalogue spectrum [*Burnashev*, 1985] and a wavelength-calibrated spectrum acquired by the instrument. Significant features are indicated with the calibrated wavelengths shown in brackets.

4.4 Intensity Calibration

The purpose of an intensity calibration is to characterize the intensity response of the instrument with respect to wavelength. Various wavelength dependent characteristics of the instrument, including the transmission of the optical elements and the quantum efficiency of the CCD, impact the measured intensity at a specific wavelength. The input of a broad-band spectrum of known relative intensity allows for *relative* calibration of the instrument intensity response.

Relative calibration of an instrument differs from the classical concept of an absolute calibration. Absolute calibration provides a transfer function between output from the instrument and the known spectral intensity of the source. A relative intensity calibration yields the ratio of measured intensities at two different bands although the absolute value of the individual measurements is arbitrary.

4.4.1 Intensity Calibration Procedure

An Ocean Optics LS-1 tungsten-halogen calibration source was used with the star simulator apparatus to develop a relative intensity calibration for the instrument. Several trials were conducted across the field of view, these revealed the effects of vignetting and the general trend in the calibration curve for non-vignetted spectra. While there is a small variation in the calibration curves across the field of view, the average of all non-vignetted calibration curves was used as the final measure.

The Ocean Optics LS-1 tungsten-halogen calibration source is nominally a 3100 K black body. The relative intensities of the input signal from the LS-1 source were calculated for a 3100 K black body and the tungsten emissivities. For a given temperature and wavelength, the Planck blackbody function gives the brightness in $\frac{W}{m^2 \cdot ster \cdot m}$,

$$B_\lambda(T) = \frac{2hc^2}{\lambda^5} \frac{1}{e^{\frac{hc}{\lambda kT}} - 1}, \tag{4.3}$$

where k is Boltzmann's constant, h is Planck's constant, T is the temperature in K, and c is the speed of light. The brightness can be converted into a photon flux,

$\frac{phots}{s \cdot cm^2 \cdot ster \cdot nm}$, using the appropriate constants and the definition of photon energy, $E_{phot} = \frac{hc}{\lambda}$. The wavelength and temperature dependent emissivity of tungsten and the Planck function (Equation 4.3) were used to determine the star simulator output. The emissivity of tungsten was taken from *Lide* [2004] for the temperature of 2800 K. There were no data available for 3100 K, although the error associated with the lower-temperature emissivity is minimal [*Degenstein*, 2005].

It should be noted that the LS-1 provides a broad-band source with no significant absorption features that can be used for calibration. To obtain proper wavelength calibration, the Oriel Optics #57200 589 nm interference filter was used to provide an artificial feature in the spectrum. The broad-band unfiltered spectrum and the spectrum with the interference filter in place were both recorded, for the same geometry of the star simulator. The shift information required for the wavelength calibration was taken from the filtered exposure and applied to the broad-band spectrum.

Several laboratory trials were made with the LS-1 lamp as the source for the star simulator apparatus. Various spectral positions across the field of view were attempted in an effort to characterize the effects of vignetting and any angular dependence to the intensity calibration coefficients. The approximate positions of the trials within the field of view are shown in Figure 4.7.

In order to define an intensity calibration coefficient for all wavelengths within the range of interest, the coefficient $C(\lambda)$ is defined as,

$$C(\lambda) = \frac{I_{known}(\lambda)}{I_{instrument}(\lambda)}, \tag{4.4}$$

where $I_{known}(\lambda)$ is the calculated brightness of the lamp as defined by Planck Law and $I_{insturment}(\lambda)$ is the output measured by the instrument. The calibration associated with a sample trial is shown in Figure 4.8. The 3100 K black body curve corrected for the emissivity of tungsten (red), the measured instrument output (green) and the calibration coefficient (blue) are shown.

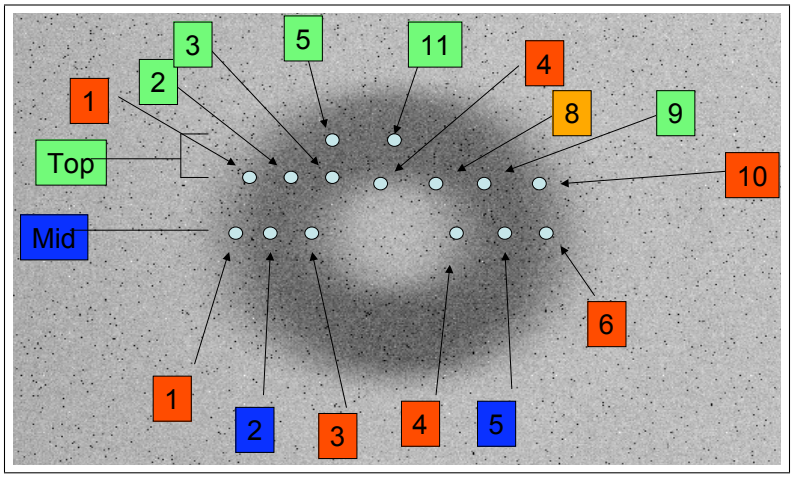

Figure 4.7: Approximate positions of the 5890 Å filter peaks used for the intensity calibration. Two sets of trials were conducted, one in the centre of the field of view (the "Mid" trials in blue), and the other at the top of the field of view (the "Top" trials in green). Vignetted spectra are indicated in red (heavy) and orange (light).

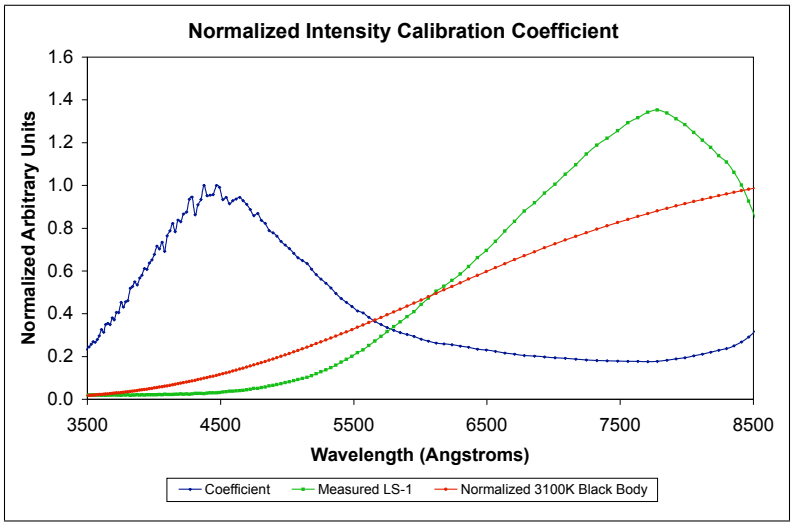

Figure 4.8: Intensity calibration of a sample spectrum. The theoretical curve is divided by the uncalibrated spectrum to produce the calibration coefficient.

4.4.2 Results

The results showed large variations in the measured intensity for those trials where there is vignetting and small variations for those trials within non-vignetted areas of the field of view. The non-normalized calibration coefficients $C(\lambda)$ for the "top" trials are shown in Figure 4.9. Vignetted spectra near the outer edge of the field of view and near the shadow of the secondary mirror exhibited significantly different calibration coefficients. Non-vignetted spectra were generally uniform, although there was some variation at shorter wavelengths. This variation is due to the spectrum from the LS-1

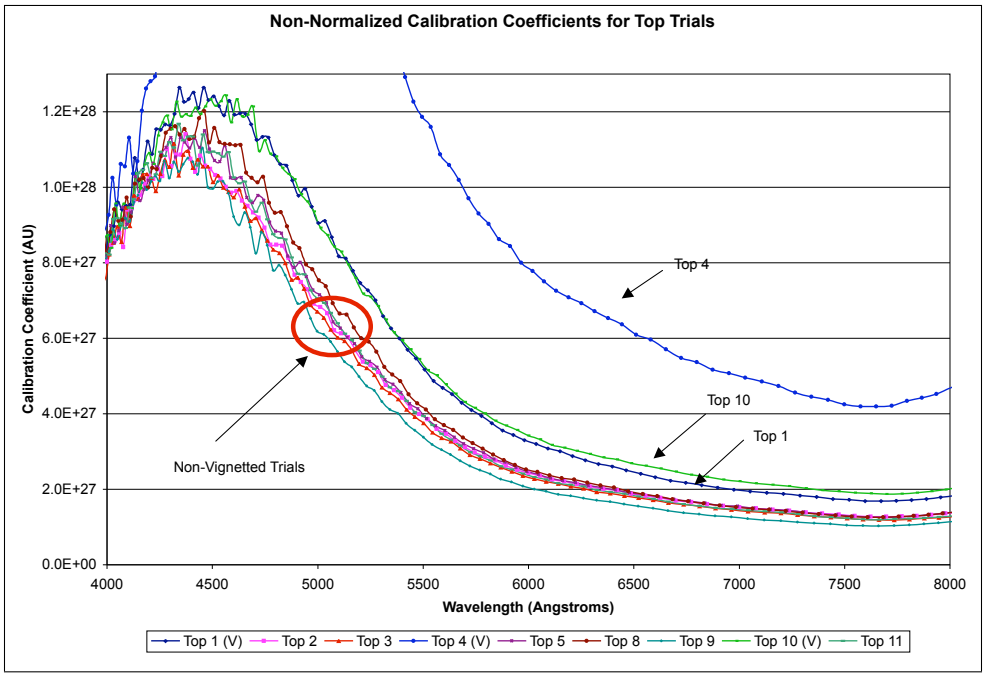

Figure 4.9: Non-normalized calibration coefficients for the "top" trials. Vignetted spectra show inflated calibration coefficients, while non-vignetted spectra are qualitatively uniform.

lamp, which, because of its lower temperature, does not have a high intensity output at shorter wavelengths. This introduces a higher noise for the region $\lambda < 5000$Å, and so the observed structure in the calibration coefficient curve. Structure in the wavelength dependent quantum efficiency of the CCD is responsible for the non-

random structure observed across all trials in particular wavelength bands.

Relative calibration depends only on the shape of the coefficient curves. To examine the trends in the non-vignetted trials, all trials were divided by the Mid5 trial, which is a typical trial. The division produced flat (horizontal) curves, this indicates a uniform shape for all coefficient curves. Trials from the left side of the field of view exhibited a small, negative slope while those from the right side showed a slightly positive slope. This effect is probably due to variations in dispersion across the field of view that were not properly accounted for in the average wavelength calibration. The results of this analysis are shown in Figure 4.10.

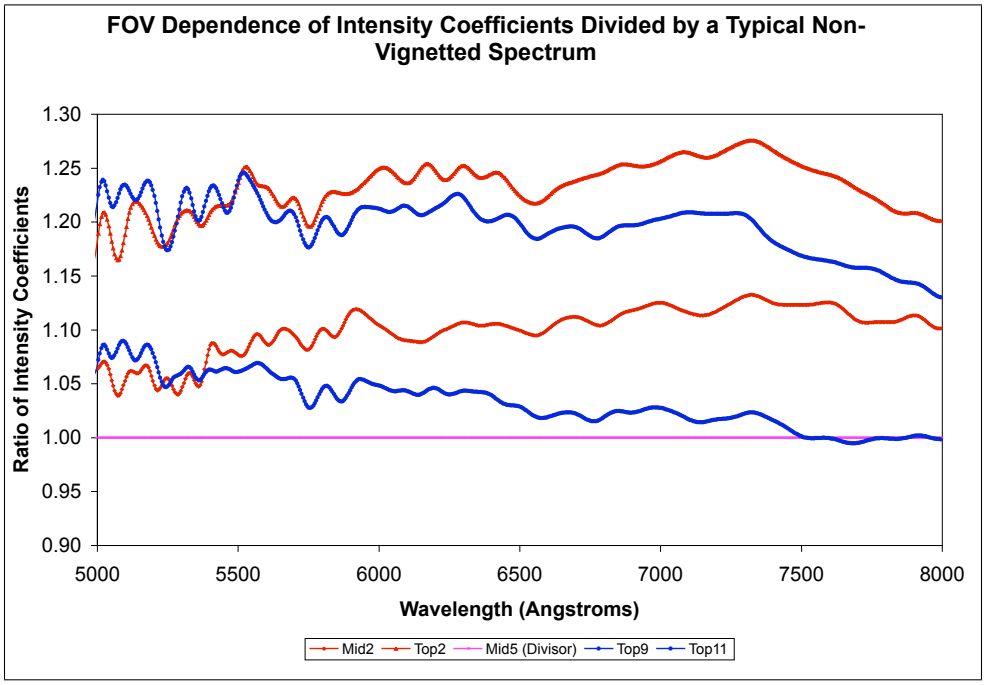

Figure 4.10: Selected typical non-vignetted trials divided by the Mid5 trial. While the results are generally flat, indicating a qualitatively uniform shape, trials from the left side of the FOV (blue) showed a slightly negative slope, conversely the right side trials (red) show a slightly positive slope.

For the purposes of a proof-of-concept prototype, the small differences in the shape of the intensity calibration coefficient curves in the non-vignetted trials were

neglected and the normalized average was used to calibrate the collected stellar spectra. The normalized average intensity calibration coefficient used in the present work is shown in Figure 4.11.

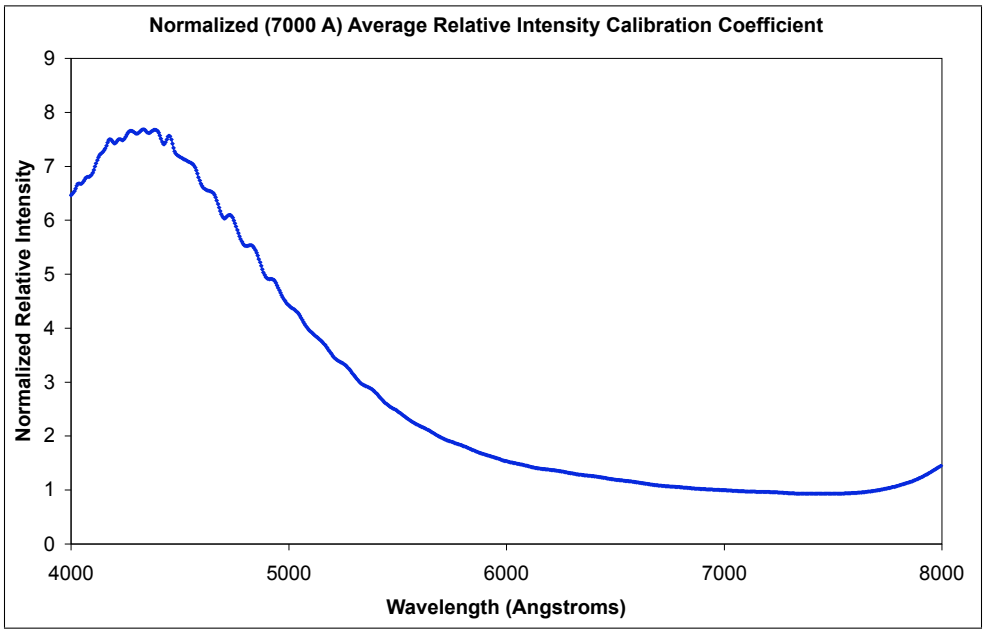

Figure 4.11: The average intensity calibration coefficient used to calibrate stellar observations.

4.5 Conclusion

The characterization of both the dispersion of the spectrometer and its intensity response was successful. While both the wavelength and intensity calibrations exhibited variations, associated with the spectral position within the field of view, these variations were small so that an average value could be used for calibration. The comparison of a wavelength- and intensity-calibrated observation spectrum of Aldebaran and a catalogue spectrum is shown in Figure 4.12. The intensity difference in shorter wavelengths is due to Rayleigh scattering and the difference in stellar zenith angles for the catalogue and observation spectra.

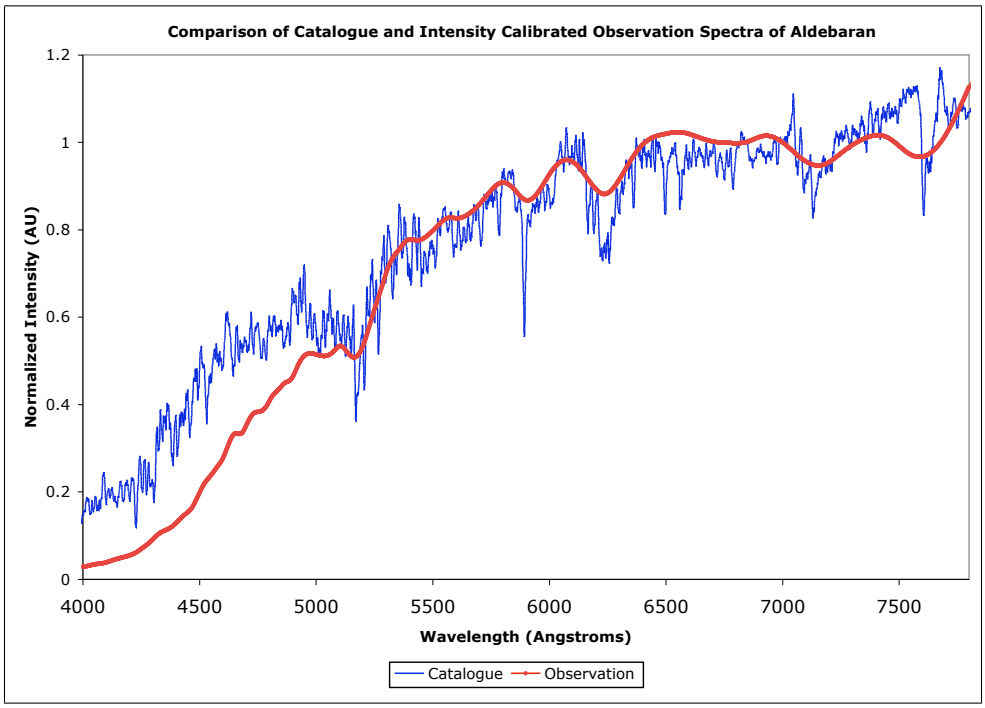

Figure 4.12: Comparison between a catalogue spectrum of Aldebaran [*Burnashev*, 1985] and a calibrated spectrum collected by the instrument.

Chapter 5

Data Collection and Analysis

5.1 Introduction

The spectrograph was set up on the roof of the Physics Building at the University of Saskatchewan to collect stellar spectra. The data were then analysed to evaluate the performance of the design. Observations were made on a single star each night, with a preset time delay between exposures. The observation sessions were completely automated except for the manual telescope mount calibration and a periodic manual correction of telescope pointing.

Analysis of the collected data was initiated immediately after each spectrum was obtained. The spectra were orthogonally binned and the data were saved as both an astronomical standard FITS image of the spectrum and an orthogonally-binned line profile. The line profile was subsequently calibrated with respect to wavelength and intensity, and an analysis performed to determine if the Chappuis ozone absorption feature was detectable. The stellar spectrum and the effects of Rayleigh scattering were both removed from the data, and the variation of the Chappuis feature with stellar zenith angle characterized. This approach determined the observability of the Chappuis absorption feature and identified several major concerns with the operation and design of the prototype spectrograph.

5.2 Observation Protocol

While the prototype could be easily modified to observe several stars during each observing session, for test purposes observations were limited to a single star each

night. The instrument setup followed a strict routine, and the telescope then tracked the star of interest for the observing period. The camera control software determined the exposure time for each spectrum and saved both the raw CCD frame images and orthogonally-binned line spectra for further analysis.

The instrument is pictured in Figure 5.1. The procedure followed for each observation was:

- Mount the spectrometer on the telescope
- Establish complete connections between the control computer, the CCD and the telescope
- Calibrate the telescope mount
- Begin tracking the star of interest
- Engage the camera control routine for regular exposures
- Make periodic manual adjustments to the telescope pointing

Each step in this procedure is discussed in some detail below.

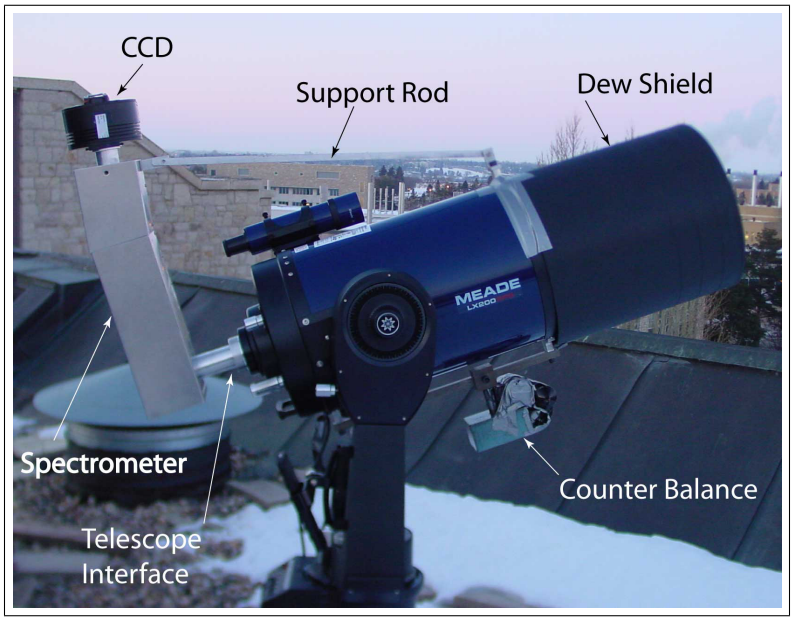

Figure 5.1: The prototype instrument with subsystems indicated.

5.2.1 Mounting the spectrometer on the telescope

The telescope and spectrometer are stored separately to minimize dust accumulation and long-term mechanical stress on the components. The spectrometer (with CCD attached) was mounted on the rear of the telescope tube, using the threaded ring of the spectrometer-telescope mechanical interface, and the support rod, which runs from the spectrometer-CCD mechanical interface to the front of the telescope, was also attached. The counterweight was added to the rail and balaced for the average altitude (zenith distance) of the star during the observing period. Once the spectrometer was attached and balanced, the physical system was ready for operation.

5.2.2 Establish complete connections between the control computer, the CCD and the telescope

Control and power cables were attached to the telescope and CCD. The telescope requires power from an external 12V 2.5 A power supply or from internal batteries. An RS-232 cable provided the connection between the control computer and the telescope mount. The CCD is powered from an external 12V DC supply that is temporarily mounted on one of the fork arms of the telescope. A USB cable is used to connect the CCD to the control computer. The required software interfaces between the control computer and the CCD and telescope were automatically established when the appropriate custom programs were launched.

5.2.3 Calibrate the telescope mount

The Meade LX200GPS-SMT telescope used for the prototype spectrograph has a fully automated mount that, after calibration, is able to track the star of interest throughout the observing period. The telescope mount includes an integrated tilt sensor, magnetometer and GPS system that is used to automatically determine the position, the altitude, the orientation with respect to true north, and the tilt and tip of the mount. Once the auto-calibration feature of the telescope is engaged

the telescope mount automatically calibrates. The user is required to center the telescope on two automatically, or manually, selected stars, in order to complete the basic mount calibration. As the telescope is stored indoors and must be moved for each observing session, this coarse calibration is required each time.

To achieve improved pointing accuracy the telescope could be mounted on a permanent pier mounting. Permanent mounting will allow improved calibration of the telescope pointing software and so eliminate periodic pointing errors due to the telescope drive motors and imperfect counterbalancing.

5.2.4 Begin tracking the star of interest

Star tracking was established automatically using the control computer and the custom program *TelescopeControl*, which performs its own astrometric calculations using the NOVAS package. Optionally, star pointing and tracking may be initiated through manual control of the telescope using the LX200 Autostar II handset, this approach relies on the astrometric calculations of the telescope mount itself. In practice the custom program *TelescopeControl* was generally used to point the telescope at the star of interest and initiate tracking, however either method was acceptable.

5.2.5 Engage the camera control routine for regular exposures

After the telescope was properly calibrated and was tracking the star of interest, the CCD was exposed to collect spectra. Camera control was accomplished through the *AutoExposure* custom routine. This routine was called at regular user-defined intervals by *TelescopeControl*. For those occasions where direct tracking by the telescope mount was used, a separate program *CameraControl* controlled the regular CCD exposures. *CameraControl* was developed for testing purposes and is a subprogram of *TelescopeControl* that was used to interface with the CCD, however it lacks the functions necessary to control the telescope. The spectra collection continued for a user-defined period or for a pre-defined number of exposures, in

either case there is a user-defined delay between exposures.

5.2.6 Perform periodic adjustments to telescope pointing

The coarse telescope mount calibration required that the instrument be supervised and periodic adjustments made to telescope pointing during the observing period. In general a pointing correction was required every 20 minutes. Periodic errors in telescope pointing caused the position of the spectrum in the field of view to oscillate both vertically and horizontally. These periodic errors were due to imperfections in the telescope drive motors, but could be corrected using the Periodic Error Correction feature in the telescope mount software. The vertical oscillation appeared to depend on the stellar zenith angle; this additional drift component was probably due to the variation in counterbalance as the star rises (or sets). A permanent pier mounting and periodic error calibration of the telescope mount would eliminate most of these pointing errors.

5.3 Stellar Observations

The majority of the collected spectra were for the star Aldebaran, which is shown in Figure 5.2. This star was selected due to the time of year of the observations, its brightness and the many Fraunhofer features in its spectrum. These features were required for wavelength calibration. Several nights of observations were made during the period September-December 2005. Cloud conditions and complications due to factors such as temperature, dew or frost and wind often reduced the available observing time. The purpose of these observations was to collect spectra from a star at various zenith angles and demonstrate that the prototype spectrograph could observe the Chappuis absorption feature. A successful ozone measurement would provide the proof of concept for ground-based ozone detection from stellar spectra.

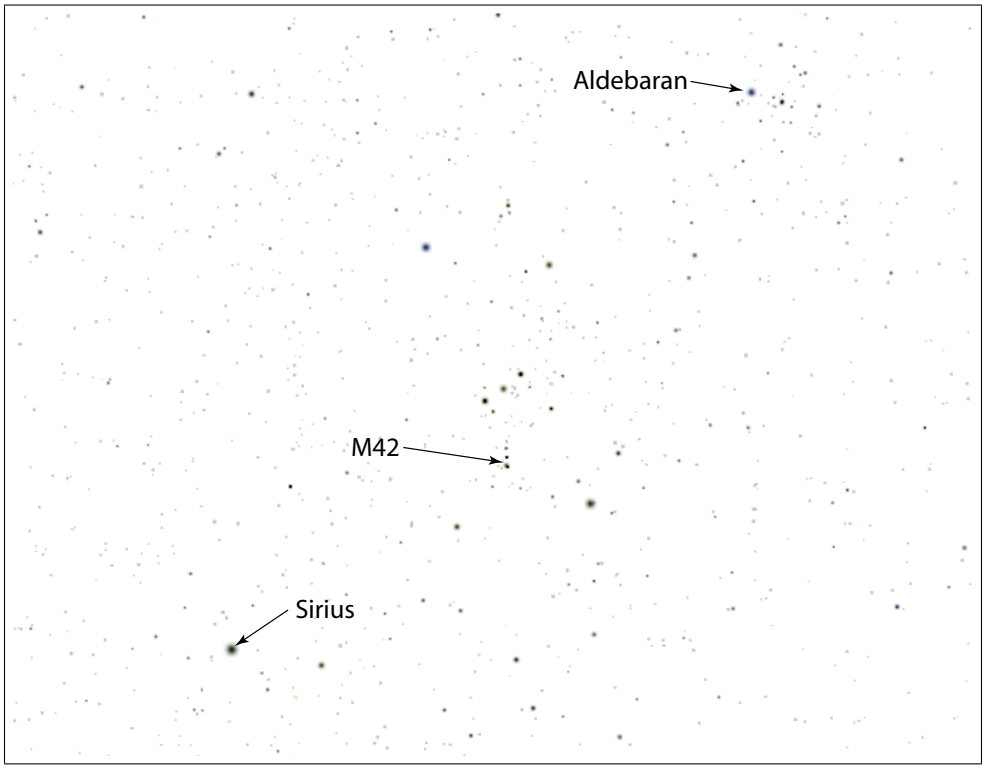

Figure 5.2: Aldebaran as viewed looking South from Saskatoon at 00:00 hrs 01 January 2006. Magnitude 4.0 stars and brighter are shown. The constellation Orion, the Orion Nebula (M42) and the bright star Sirius are also visible.

5.3.1 Aldebaran

Aldebaran (α Tauri) is located 65.17 light years away in the constellation Taurus (Figure 5.2) and is the 13^{th} brightest star in Earth's sky, it has an apparent magnitude of 0.84 Mag. It is an irregularly variable star with a maximum variation of $<$0.06 Mag. Aldebaran is a red giant star with a spectral classification of K5-III. This type of star has exhausted its supply of hydrogen and has progressed to fusing helium into carbon and oxygen at its core. This process produces a star that exhibits a high "metallicity", meaning that higher metal elements such as magnesium and iron are prevalent in its atmosphere and results in a highly structured spectrum. In addition, the surface temperature of Aldebaran is approximately 4000 K with a consequent orange-red hue in the visual band [*Ochsenbein et al.*, 2000].

5.3.2 Data

Observations of Aldebaran were conducted for several nights from September to December 2005. On each occasion the observing procedure followed that outlined above. The instrument was positioned on the roof of the Physics Building at the University of Saskatchewan. As previously noted, cloud cover, precipitation and dew or frost often compromised the observing sessions, so that only six useful data sets were collected. High quality spectra at large zenith angles ($> 80°$) proved difficult to obtain due to cloud on the horizon, dust and strong scintillation effects. The data sets are summarized in Table 5.1.

Table 5.1: Summary of the observational trials conducted.

Date	No. of Spectra	Range of Zenith Angles (°)
01 Sept	17	84 - 75
19 Sept	30	86 - 58
21 Sept	95	79 - 43
05 Oct	15	84 - 75
14 Oct	40	83 - 57
11 Dec	130	75 - 36

The data set obtained on 21 September 2005 is shown in Figure 5.3. Each spectrum has been calibrated and normalized to the intensity at 7800 Å. Due to the relative nature of the intensity calibration, these data are represented in *arbitrary units per second* (AU/s), which are proportional to the photon flux at a particular wavelength incident on the CCD chip. Fraunhofer absorption features in the stellar spectrum are readily evident, as are the effects of Rayleigh scattering. An attenuation that varies with zenith angle is accentuated in the 5000 to 7000 Å band by the combined effects of Rayleigh scattering and Chappuis absorption. Errors in the wavelength calibration are also seen in Figure 5.3. Small zenith distance spectra generally show absorption features with a deep relative attenuation that results

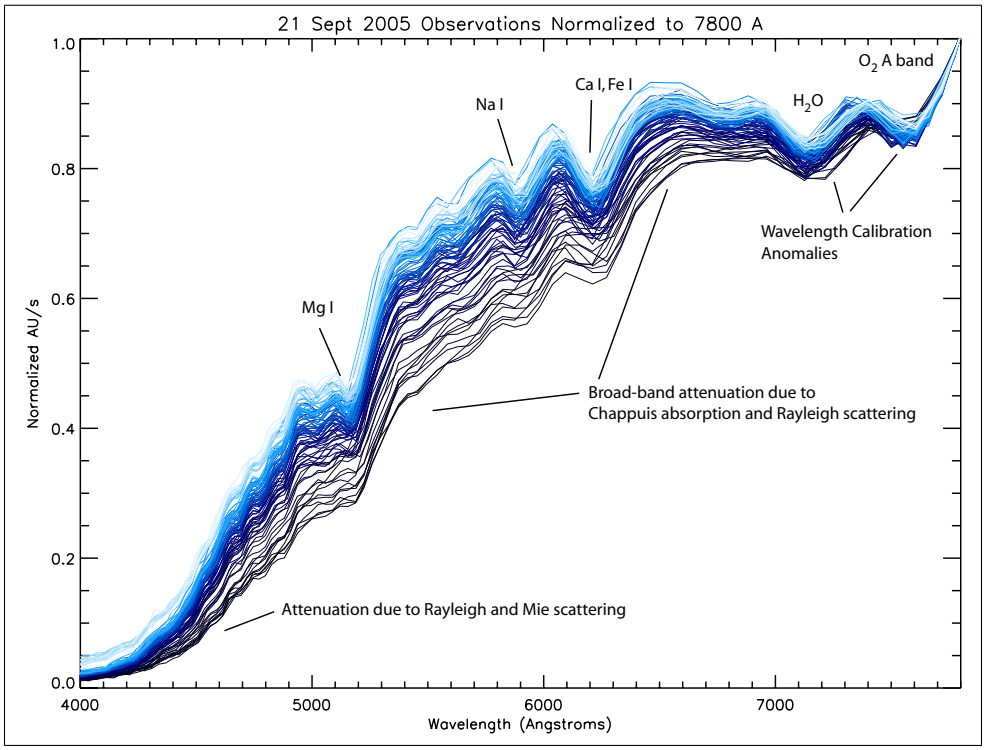

Figure 5.3: The entire data set from the 21 September 2005 observing session. Spectra with higher stellar zenith angles are dark blue, fading to light blue for spectra with lower zenith angles. Significant narrow-band absorption features are indicated. Rayleigh scattering and Chappuis absorption combine to provide zenith angle dependent attenuation in the 5000 to 7000 Å band. All spectra are calibrated and normalized to 7800 Å.

in a well-defined wavelength calibration. Conversely, Fraunhofer features in large zenith distance spectra appear "washed out" and produce broader absorption features. These broad features result in an uncertainty in the wavelength calibration. This problem is compounded by the fact that the adopted wavelength calibration used a feature in the lower-resolution area of the spectrum, thus small errors in the fractional pixel location of the calibrated feature introduced large errors in the wavelength calibration. Additional factors that may have degraded the reliability of large zenith distance spectra included strong scintillation effects from atmospheric distortion, light pollution and high aerosol concentrations due to the urban location of the observations.

5.4 Analysis

The goal of the prototype is to demonstrate a proof-of-concept, low-cost, low resolution stellar spectrometer that can detect Chappuis absorption. A qualitative analysis was used to determine the effectiveness of the instrument.

The spectra acquired by the prototype are a convolution of instrument effects, broad-band atmospheric extinction due to Rayleigh scattering and ozone absorption, together with specific absorption features due to other trace gases. The analysis of the collected data began with wavelength and intensity calibration in order to eliminate instrument effects. The calibrated data were then normalized and several techniques were used to isolate the Chappuis absorption feature and show its variation with stellar zenith angle.

5.4.1 Division by a Reference Spectrum

The normalized data in Figure 5.3 show a combination of atmospheric and stellar features. Rayleigh and Mie scattering attenuate across the band of interest, and there are several obvious narrow-band absorption features due to Fraunhofer absorption in the stellar atmosphere and absorption by gases in the terrestrial atmosphere. The broad-band Chappuis absorption feature is not readily identified.

In an attempt to eliminate the effects of the stellar spectrum, the data were divided by a small zenith distance spectrum that was designated as the reference spectrum. This technique removes the features of the stellar spectrum, which are common to all spectra, and clearly shows the zenith angle-dependent atmospheric absorption features. The division of spectra results in a curve that represents the differences in optical depths, as shown in Equation 5.1,

$$\frac{\mathrm{I}_0(\lambda)\mathrm{e}^{-\tau_\theta(\lambda)}}{\mathrm{I}_0(\lambda)\mathrm{e}^{-\tau_{\mathrm{ref}}(\lambda)}} = \mathrm{e}^{\tau_{\mathrm{ref}}(\lambda)-\tau_\theta(\lambda)}, \tag{5.1}$$

where $\tau_\theta(\lambda)$ is the optical depth of the atmosphere for a particular observation, and $\tau_{\mathrm{ref}}(\lambda)$ is the optical depth of the atmosphere for the reference spectrum.

After division by the reference spectrum, low zenith distance spectra are qualitatively flat, while high zenith distance spectra display the combined effect of Rayleigh scattering and Chappuis absorption. Atmospheric absorption features, which were not significant in the low zenith distance spectra, now appear as relative attenuation. The results of the division analysis for the data set collected on 19 September, 2005, are shown in Figure 5.4.

The divided spectra exhibit atmospheric features due to both Rayleigh scattering and absorption by trace gases such H_2O and O_2. However, the significant Fraunhofer features due to Mg I, Na I, and Ca I/Fe I are still apparent in the divided spectra, and sometimes appear as peaks. The possibility of atmospheric emissions in the night sky as a source of the peaks appearing at the Fraunhofer feature wavelengths was examined, but eventually discounted. Though both calcium and iron are deposited by meteorites at 80-100 km, and sodium emissions and backscatter from street lamps are all possible sources of emission for the peaks seen in Figure 5.4, the design of the instrument precludes the measurement of atmospheric emissions. Any emissions produced by the atmosphere fill the entire field of view of the instrument, so completely mixing the spatial and spectral information. The result is a higher noise level that effectively introduces a DC offset to the CCD frame. Variations in airglow brightness across the field of view would produce a variable offset that produces "phantom" low frequency structure. However, the signal introduced by

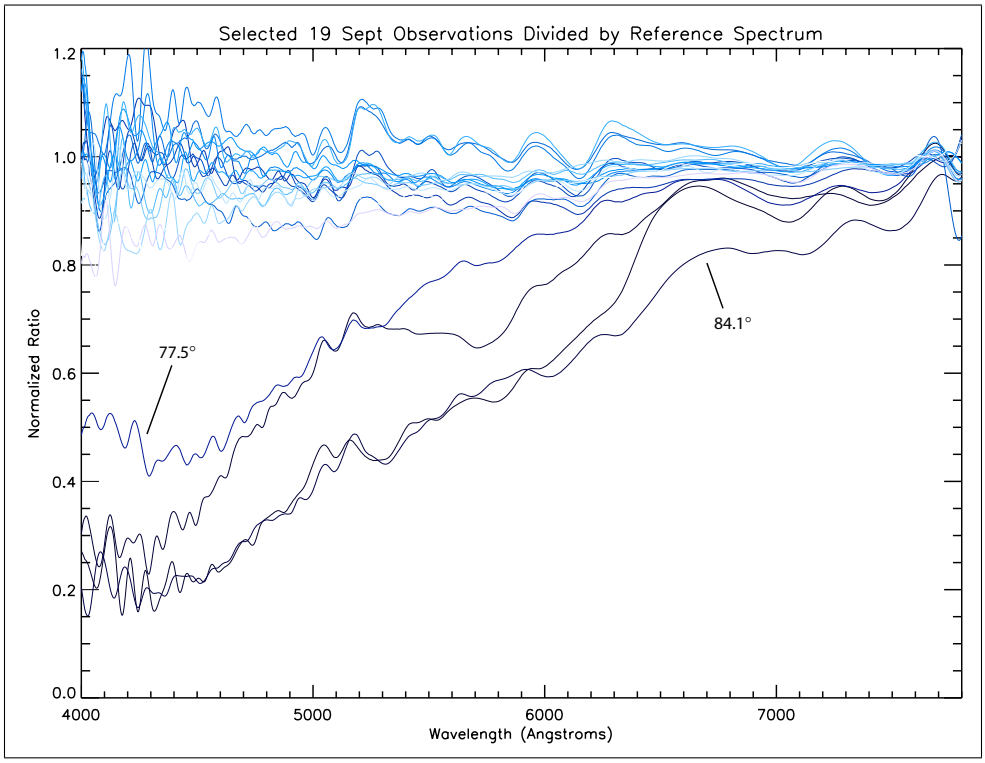

Figure 5.4: Divsion of each spectrum in the 19 Sept 2005 data set by a low zenith distance reference spectrum. Low zenith distance spectra (light blue) are relatively flat. High zenith angle spectra are strongly attenuated by Rayleigh extinction, and Chappuis absorption is apparent between 5000 and 7000 Å.

airglow is small compared to the stellar signal, and the result is a slight degradation in the signal-to-noise ratio of the instrument. It was determined that the variation of Fraunhofer feature depth with SZA, due to the instrument-induced feature broadening discussed above, was responsible for the observed peaks. The division of the data by a low zenith angle reference spectrum removed most of the stellar features, and shows qualitative evidence that the instrument does observe Chappuis absorption, although Rayleigh scattering dominates the curve at high stellar zenith distances.

Further analysis was attempted in order to remove the extinction due to Rayleigh scattering. Consider an expansion of Equation 5.1 that includes the contribution of broad-band extinction species,

$$\frac{I_0(\lambda)e^{-\tau_\theta(\lambda)}}{I_0(\lambda)e^{-\tau_{\rm ref}(\lambda)}} = e^{\tau_{\rm ref}(\lambda)-\tau_\theta(\lambda)} = e^{\Delta\tau} = e^{\Delta\tau_{\rm Rayleigh}} \cdot e^{\Delta\tau_{O_3}} \cdot e^{\Delta\tau_{\rm Mie}} \cdot e^{\Delta\tau_{\rm other}}, \qquad (5.2)$$

where the contributions of Rayleigh and Mie scattering, ozone absorption in the Chappuis band and a summary term representing absorption from other trace gases have been isolated. The optical depth of the atmosphere due to non-Rayleigh scattering species can be found by dividing Equation 5.2 with the theoretical contribution from Rayleigh scattering and taking the natural logarithm. This is shown in Equation 5.3.

$$\Delta\tau = \ln\left(\frac{e^{\Delta\tau_{\text{Rayleigh}}} \cdot e^{\Delta\tau_{O_3}} \cdot e^{\Delta\tau_{\text{Mie}}} \cdot e^{\Delta\tau_{\text{other}}}}{e^{\Delta\tau_{\text{Rayleigh}}}}\right) = (\Delta\tau_{O_3} + \Delta\tau_{\text{Mie}} + \Delta\tau_{\text{other}}) \qquad (5.3)$$

This analysis was applied to the observations using the theoretical optical depth due to Rayleigh scattering at the SZA of each observation, which was calculated by the atmospheric absorption model. The results of this removal of the Rayleigh scattering signal are shown in Figure 5.5. Chappuis absorption decreases with zenith angle and is undetectable in the small zenith distance spectra. The general trend visible in the low zenith distance spectra is probably a residual arising from the difference between the theoretical and observed Rayleigh optical depths.

To show the variation of Chappuis absorption with zenith distance, the residual trend was removed from the four highest zenith angle spectra, shown in red, green, blue and light blue in Figure 5.6. These spectra exhibit Chappuis absorption between 5000 and 7000 Å and a potential Mie scattering component below 5000 Å. The Chappuis absorption decreases as the stellar zenith distance decreases, this shows that Chappuis band absorption is detected in the stellar spectra.

The red curve shown in Figure 5.6 represents the difference between the optical depth due to Chappuis absorption at zenith distances of 84.1° (observation) and 36.2° (reference). To verify the accuracy of the measurement, the ozone profile for Saskatoon on 19 September, 2005 was acquired from the Labow climatology. This profile, and path lengths calculated with the absorption model, were used to calculate the expected slant columns at 84.1° and 36.2°. The difference in optical depth between the expected slant columns at 6000 Å is 0.287, which is comparable to the experimental value of 0.261 from the data presented in Figure 5.6. Expressed as a vertical ozone column, the experimental data yield a value of 341.5 Dobson

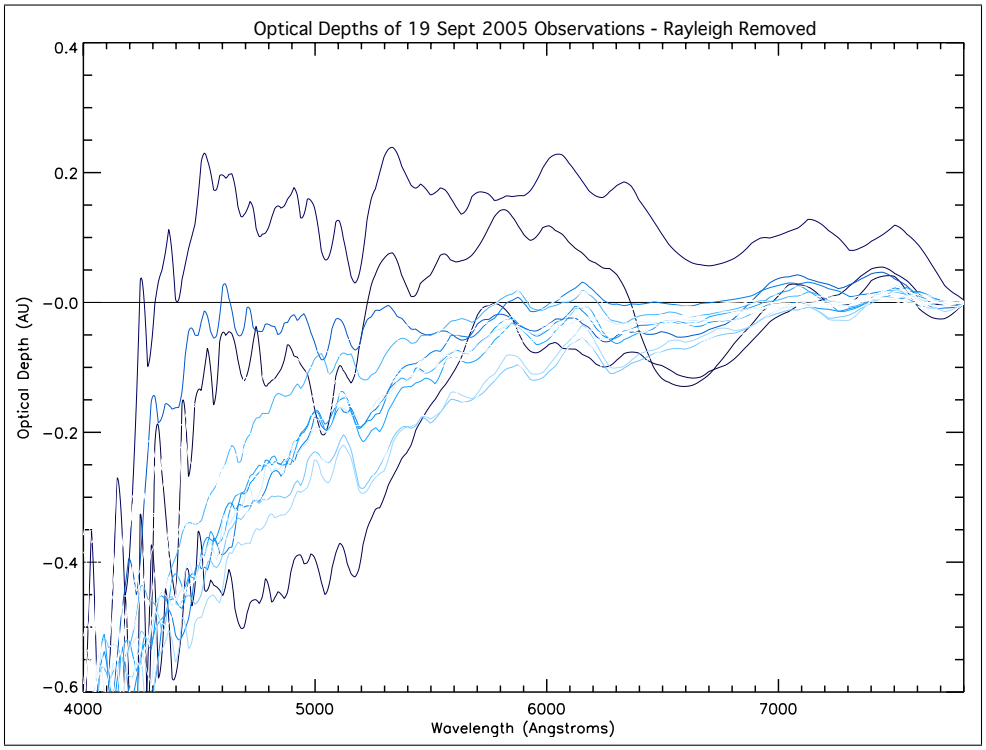

Figure 5.5: Optical depths of the 19 Sept 2005 observations after removal of the Rayleigh scattered signal. The atmospheric absorption model was used to calculate the theoretical Rayleigh scattering optical depths that were removed from the data. The removal of the Rayleigh signal resulted in a residual trend.

units, which is in agreement with the Labow climatology column of 375.5 Dobson units. These data show conclusively that the instrument has detected Chappuis band absorption.

The analysis presented above was a simple assessment of the prototype performance and is subject to many systematic errors. These errors, combined with the generally low quality of the high zenith angle spectra, mean that the analysis did not produce the familiar shape of the absorption cross section of ozone in the Chappuis band. The analysis does show, however, that the instrument can observe the Chappuis absorption feature and its variation with stellar zenith distance. A determination of the precision of the Chappuis observations requires a more accurate and detailed analysis and is left for future work.

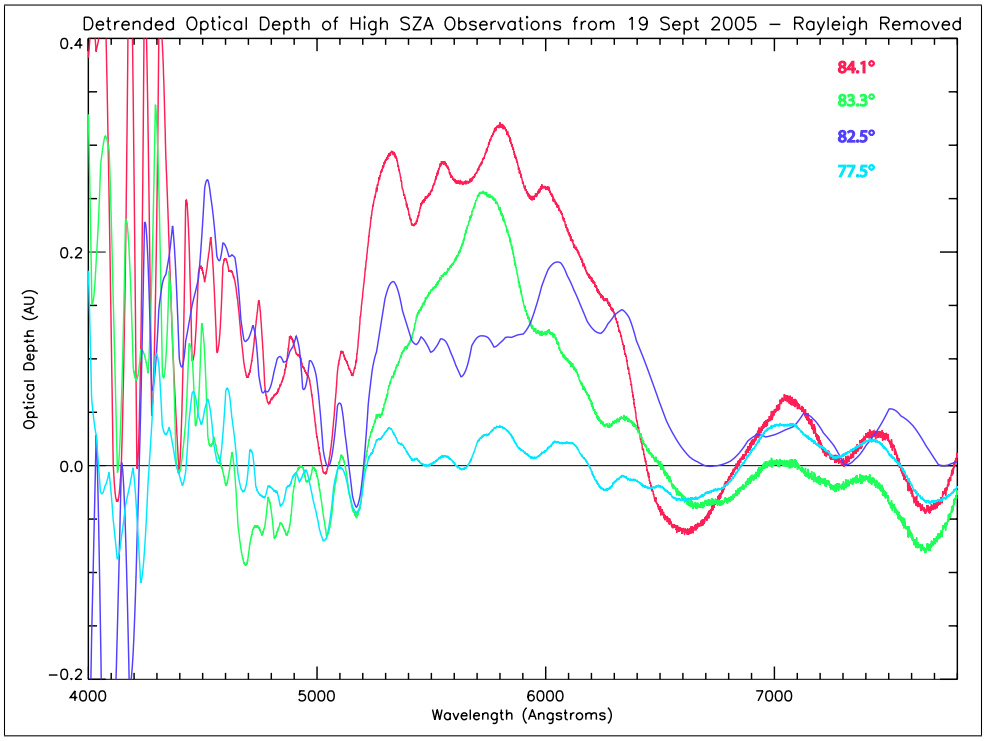

Figure 5.6: Detrended optical depths of high zenith angle observations after removal of the Rayleigh scattering signal. The residual trend due to inaccuracies in the modeled Rayeigh extinction was removed to demonstrate the variation of Chappuis absorption with SZA. High zenith distance spectra show accentuated absorption that decreases as the star rises. These spectra show that the insturment can observe variations of optical depth in the Chappuis band.

5.4.2 Wavelength Ratios

To analyse the variation of the Chappuis absorption feature depth with respect to stellar zenith angle, a ratio of wavelengths was performed for each spectrum. The signal at a strongly absorbed wavelength was divided by the signal at a wavelength that is not absorbed by ozone. This ratio decreases as the optical depth due to ozone along the instrument line of sight increases, and is an indication of the Chappuis absorption feature depth. The atmospheric absorption model developed for the present work was used to provide a preliminary theoretical baseline for this qualitative evaluation of the effectiveness of the instrument. As shown previously in Section 3.3,

the model can be used to estimate the variation of intensity ratios due to Rayleigh extinction and Chappuis absorption at various stellar zenith distances. Using a catalogue spectrum of Aldebaran [*Burnashev*, 1985] as input, the variation of the ratio of intensities at 6000 Å to 7800 Å calculated with the model is shown in Figure 5.7.

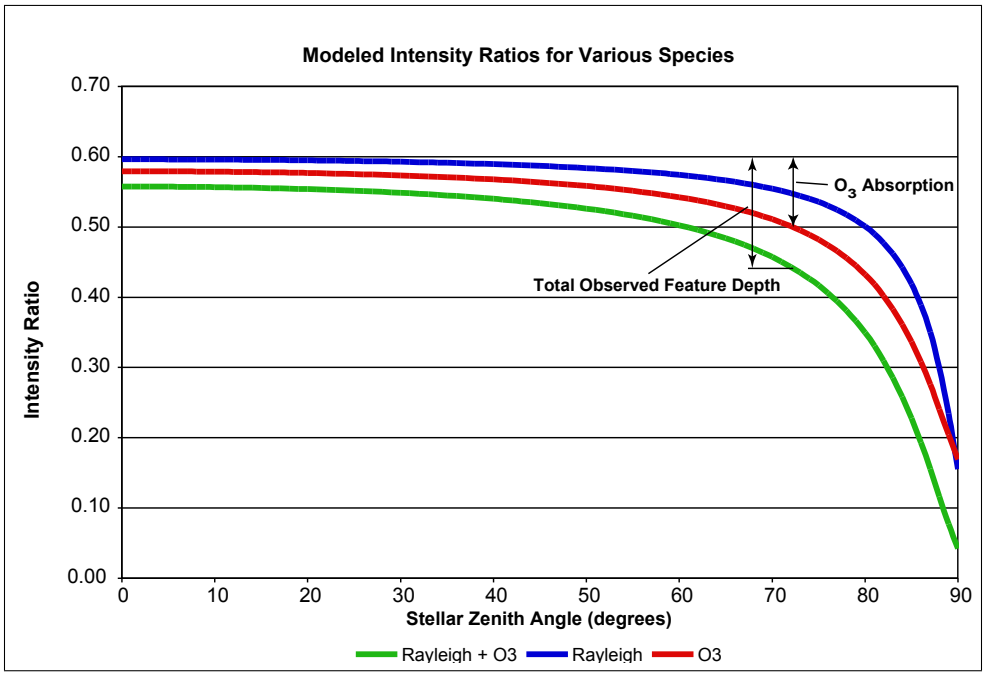

Figure 5.7: Modeled wavelength ratios produced by the atmospheric absorption model. The modeled ratios were used as a rough order validation of the data acquired by the instrument.

The analysis of the collected data sets shows a general trend that displays the same shape as the modeled results. Examples from several observing sessions are shown in Figure 5.8. There is significant noise in the results, this is due to imperfections in the wavelength calibration. The highly structured spectrum of Aldebaran causes the ratio of intensities to be sensitive to small errors in the wavelength calibration. As errors in the wavelength calibration increase with increasing zenith angle due to broader Fraunhofer features, so does the magnitude of the noise in the data. Two different wavelength pairs were used to create the ratios shown in Figure 5.8. The intensity at 7000 Å was used for the Oct 14 observations, while the intensity at 7800 Å was used for the other data sets; in each case the intensity at 6000 Å was

the numerator. The modeled ratio is for the intensity at 7800 Å. The results from different ratio pairs showed that the selection of the unabsorbed wavelength had little effect on the noise in the data, it only shifted the general trend to an increased or decreased average ratio. This supports the hypothesis that the noise in the data is due mainly to issues with the wavelength calibration.

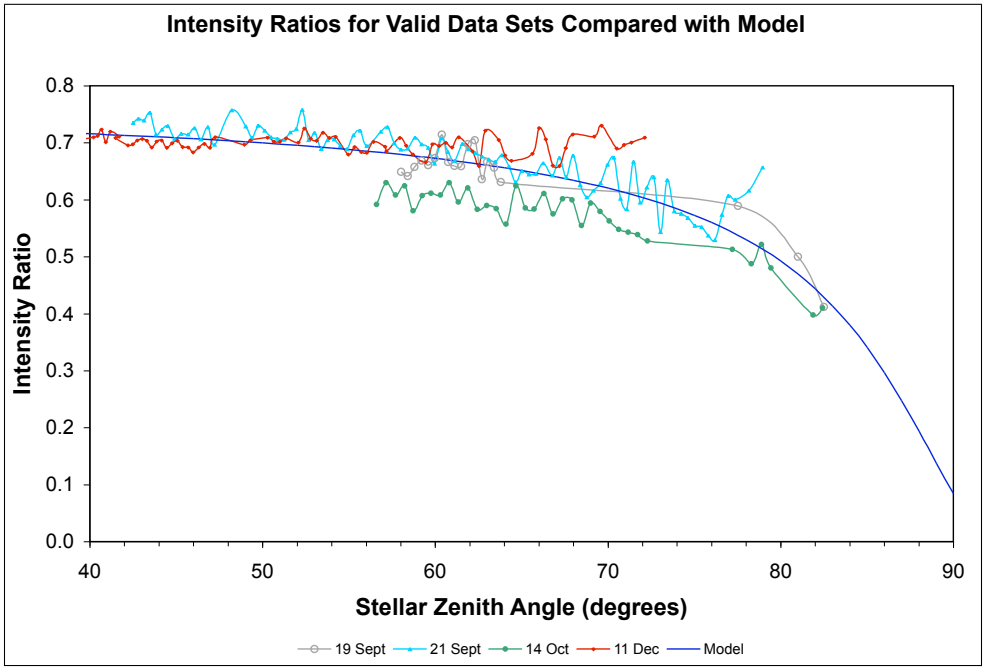

Figure 5.8: Intensity ratios (6000 - 7800 Å) of spectra from several observing sessions compared with modeled ratios. The model results show the increased attenuation at higher zenith angles due to Rayleigh scattering and Chappius absorption, which qualitatively validates the trend exhibited by the data.

Small zenith distance spectra from observations on 11 December, 2005 show good agreement with the model, but the higher zenith distance observations did not exhibit the expected attenuation. The 21 September 2005 data set shows the expected attenuation at high zenith distances. In agreement with the model, the data show significant absorption only for zenith distances greater than 80°, this is seen in the 19 Sept and 14 Oct observations. In addition, the data analysis with the line pairs shows that there are significant issues with noise that increases with stellar zenith distance. The intensity ratio analysis has demonstrated the successful

detection of Chappuis band ozone absorption.

5.4.3 Instrument Performance

The instrument performed according to the design specifications. The Chappuis band absorption feature has been measured by the prototype instrument. Observations were automated and the developed software infrastructure was designed to facilitate the expansion of automation features. The total cost of the prototype was approximately CDN$ 8000, which complies with the budget specification. Fourth magnitude stars were observed and the exposure time required for 75% full well is ∼30 seconds. The field of view of the instrument has been estimated from an image of the Orion Nebula (M42) as ∼8 arcmin.

The spectral response of pixels has been calculated based on gas lamp spectra, with the assumption that a monochromatic spot has a gaussian intensity profile and that changes in dispersion are minimal across a single pixel. The results for pixels with central wavelengths of 5460 Å and 7800 Å are shown in Figure 5.9. At 5460 Å the pixel band-pass is approximately 100 Å, while at 7800 Å the band-pass increases to approximately 440 Å. The band-pass specification is achieved in the centre of the wavelength region of interest, although resolution is degraded at longer wavelengths.

5.5 Conclusion

The operation of the prototype spectrograph and the analysis of experimental data have shown that the instrument does successfully observe ozone absorption in the Chappuis band. However, significant issues with the operation and design of the prototype were identified, as discussed in Sections 5.3.2 and 5.4.1. Difficulties were encountered obtaining valid spectra near the horizon due to environmental effects. The contradiction in design goals produced by using Fraunhofer absorption features as the basis of the wavelength calibration became apparent. This contradiction compromised the performance of the instrument, and a practical redesign of the instrument is recommended to address this problem.

(a)

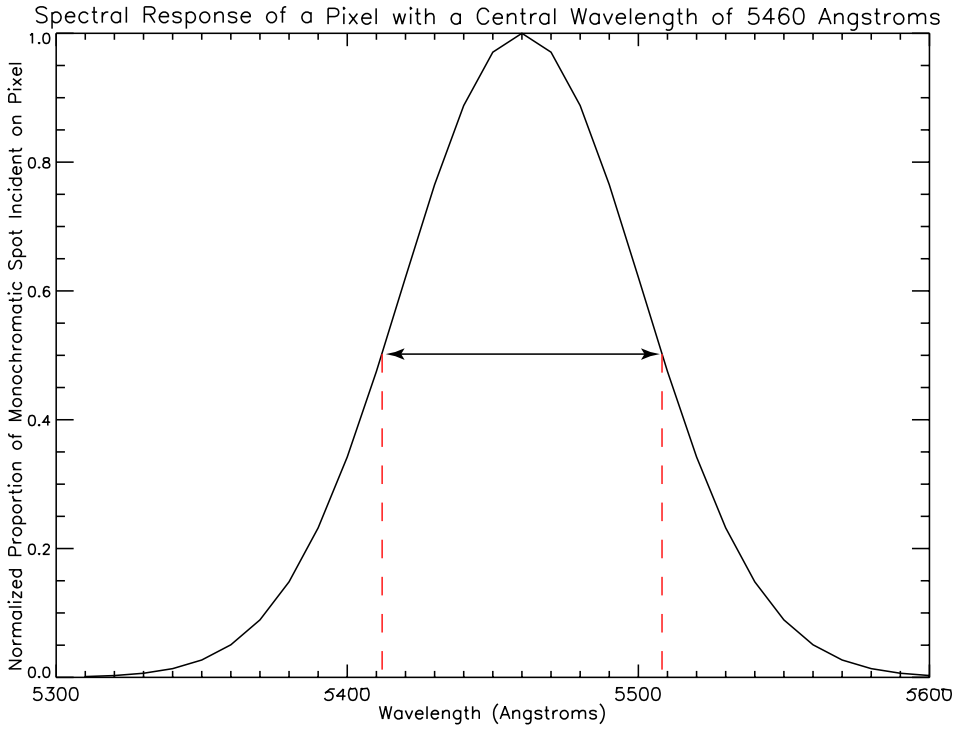

(b)

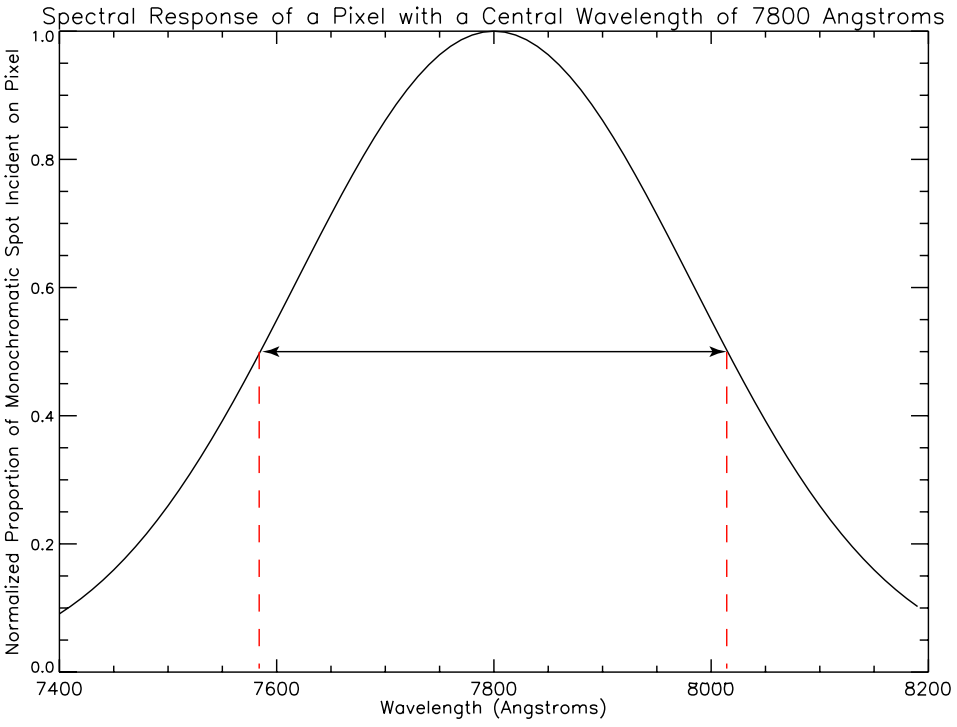

Figure 5.9: The calculated spectral response of two pixels. (a) A pixel with a central wavelength of 5460 Å has an approximate band-pass of 100 Å. (b) At 7800 Å the band-pass increases to ∼440 Å.

Chapter 6

Summary and Conclusions

6.1 Summary of the Present Work

In the present work a prototype ground-based stellar spectrometer was designed and developed as a proof-of-concept ozone-monitoring instrument that uses a slitless spectrograph to measure Chappuis band absorption. As a proof of concept the prototype was a success; it demonstrated the detection of Chappuis band absorption in stellar spectra and allowed the identification of several flaws in the concept and design.

Prototype specifications were identified and the design process began with the development of an atmospheric absorption model, this latter was used to verify the concept of ground-based measurement of absorption in the Chappuis band. Optical and mechanical design of the spectrometer followed the design specifications and initial testing led to several optimizations to correct limitations in the original design. A commercial telescope and CCD camera were used for light collection and imaging, and custom software was developed to provide the necessary automation features for the instrument and the initial analysis. The slitless nature of the prototype required the development of a dynamic wavelength calibration scheme, that relied on Fraunhofer features in the stellar spectrum as a baseline for wavelength calibration. A relative intensity calibration was also made.

The prototype instrument was used to make observations from the roof of the Physics Building at the University of Saskatchewan. Spectra were collected in different weather conditions and the observations emphasized the need for additional components to mitigate against adverse effects such as frost and decreased bat-

tery performance at low temperatures. Minor issues were also identified with the star-tracking capability of the prototype, which required supervision and occasional manual correction.

The analysis of the spectra collected with the prototype revealed several problems in the current design. Spectra from high stellar zenith distances exhibited an increased Chappuis absorption, but were also sensitive to the effects of scintillation and the potential introduction of structure from either a non-constant airglow or scattered light across the field of view. The combination of a low-dispersion prism spectrometer that relies on narrow-band Fraunhofer features for wavelength calibration produced a contradiction in design goals; this introduced errors in the wavelength calibration and compromised the overall performance of the instrument. Despite these identified design problems, the prototype instrument has been used to detect Chappuis band ozone absorption in stellar spectra. Spectra collected with the prototype spectrograph provided an estimated ozone column of 341.5 Dobson units, which is in agreement with the daytime value of 375.5 Dobson units calculated from the Labow climatology.

The present work has provided a first stage in the development of an experimental ground-based stellar spectrometer for the purpose of measuring atmospheric ozone. Progressing from concept to a completed instrument, the present work has provided the foundation of the prototype subsystems, from optical design to automation software and analysis. Refinements to the specifications, based on the findings of the present work, will facilitate further instrument development.

6.2 Recommendations for Future Work

The continued development of the prototype requires the redesign of certain subsystems and an expansion of others, as discussed below. While the present work has shown that the instrument does detect ozone absorption at large stellar zenith distances, the required sensitivity for successful observations at low zenith distances requires further analysis. The development of a comprehensive, quantitative retrieval

system would provide a basis for the refinement of the design specifications.

An extended analysis of the optical system is required. The present work has shown that while the low resolution is sufficient to detect Chappuis band absorption, it has a negative impact on the dynamic wavelength calibration system required for a slitless imaging spectrograph. An improvement of the resolution of the instrument in the wavelength region of interest would improve the accuracy of the wavelength calibration and allow for the identification of finer structure in the collected spectra. In addition to an increase in resolution, a redesign of the collimator system is recommended in order to reduce the effects of aberrations and increase the field of view. An analysis of the possible use of a grating-based slit spectrometer should also be considered, although this will require more accurate telescope pointing.

The reliance on Fraunhofer features in the stellar spectra for wavelength calibration introduced a non-standard factor into the calibration scheme, as not all stars have the same features. The addition of a filter wheel to the CCD assembly should be examined. The use of a narrow-band interference filter to produce an artificial feature in the stellar spectrum may provide a more effective means for wavelength calibration than a dependence on stars with observable Fraunhofer absorption features. A comprehensive analysis of field-of-view dependent variations in the wavelength and intensity calibrations is also recommended. Due to time constraints an average calibration was used in the present work, however it has been shown that variations do exist in the dispersion and intensity response across the field of view. These variations warrant further investigation.

The prototype control software developed for the present work is quite robust, and could be expanded to include multiple-star observations and improved dark current removal. Such expansions are contingent on an improved characterization of the dark current and noise present in the system, and the increased pointing accuracy of the telescope mount.

Some additions to the mechanical systems of the prototype are also necessary, these would increase the pointing accuracy and weather-proof the system. It is believed that the pointing accuracy of the telescope would be enhanced with a per-

manent pier mount. A permanent mount allows the calibration of the telescope mount to remove imperfections in the drive gears and the effects of counterbalancing. Enhanced pointing accuracy is essential for multiple-star observations and the possible use of a slit-based spectrometer. This enhancement would also eliminate the need for manual correction of telescope pointing errors. Weather proofing the instrument with the addition of a dew shield and heating strips would allow the instrument to operate consistently in both high-humidity conditions and at sub-zero temperatures. A reduction of the physical weight of the instrument is also recommended. A reduced instrument and counterbalance weight would reduce the effect of counterbalance-induced pointing errors and minimize the stress on the telescope drive.

Prior to these major design revisions, a more involved characterization of the capabilities of the current prototype is recommended. This may be accomplished by making observations of a star with a less structured spectrum, such as Vega (α Lyrae).

6.3 Conclusion

A proof-of-concept development of a new ground-based ozone-measuring instrument has been produced in the present work. The prototype has detected Chappuis-band ozone absorption, and although the current design exhibits several limitations, the majority of the present work can be carried forward to a second-stage prototype. The knowledge of the required instrument sensitivity based on the present observations and a detailed quantitative analysis of the proposed retrieval algorithms would facilitate the focused development of a second-stage prototype.

References

Bates, D. R., and M. Nicolet, The photochemistry of atmospheric water vapour, *J. Geophys. Res.*, *50*, 301–327, 1950.

Brasseur, G., and S. Solomon, *Aeronomy of the Middle Atmosphere*, D. Reidel Publishing Company, Dordrecht, 1984.

Brewer, A. W., A replacement for the dobson spectrophotometer?, *Pure Appl. Geophys.*, *106*, 919–927, 1973.

Burnashev, V. I., Spectrophotometry of 1588 stars, *Abastumanskaya Astrofiz. Observational Bulletin*, *59*, 83, 1985.

Chapman, S., A theory of upper-atmospheric ozone, *Mem. R. Meteor. Soc.*, *3*, 103–125, 1930.

Chapman, S., Bakerian Lecture. Some phenomena of the upper atmosphere, *Proc. R. Soc. Lon. - Ser. A*, *132*, 353–374, 1931.

Chappuis, J., Etude spectroscopique sur l'ozone, *Annales Scientifiques de l'E.N.S.*, *2*, 137–186, 1882.

Cornu, A., Sur l'absorption atmospherique des raies ultra-violettes, *Journal de Physique*, *10*, 5, 1881.

Coy, L., E. Nash, and P. Newman, Meteorology of the polar vortex: spring 1997, *Geophys. Res. Lett.*, *24*, 2693–2696, 1997.

Degenstein, D. A., Private correspondence regarding the emissivity of tungsten, 2005.

Dobson, G. M. B., A photoelectric spectrometer for measuring the amount of atmospheric ozone, *Proc. Phys. Soc.*, *43*, 324–339, 1931.

Dobson, G. M. B., Forty years' research on atmospheric ozone at Oxford: a history, *Appl. Opt.*, *7*, 387–405, 1968.

Dobson, G. M. B., and D. N. Harrison, Measurements of the amount of ozone in the earth's atmosphere and its relation to other geophysical conditions, *Proc. R. Soc. Lon. - Ser. A*, *110*, 660–693, 1926.

Fabry, C., and H. Buisson, *Journal de Physique*, *2*, 196, 1913.

Fabry, C., and H. Buisson, L'absorption de l'ultraviolet par l'ozone et la limite du spectre solaire, *Journal de Physique*, *3*, 197, 1921.

Farman, J. C., B. G. Gardiner, and J. D. Shanklin, Large losses of total ozone in Antarctica reveal seasonal ClOx/NOx interaction, *Nature*, *315*, 207–210, 1985.

Fioletov, V., J. Kerr, D. Wardle, J. Davies, E. Hare, C. McElroy, and D. Tarasick, Long-term ozone decline over the Canadian Arctic to early 1997 from ground-based and balloon observations, *Geophys. Res. Lett.*, *24*, 2705–2708, 1997.

Gowan, E. H., The effect of ozone on the temperature of the upper atmosphere, *Proc. R. Soc. Lon. - Ser. A*, *120*, 655–669, 1928.

Griffin, R. E., The detection and measurement of telluric ozone from stellar spectra, *Publ. Astron. Soc. Pac.*, *117*, 885–894, 2005.

Hartley, W. N., On the probable absorption of solar radiation by atmospheric ozone, *Chem. News*, *42*, 268–270, 1880.

Hedin, A., Extension of the MSIS thermosphere model into the middle and lower atmosphere, *J. Geophys. Res.*, *96*, 1159–1172, 1991.

Hopkins, R. E., *Geometrical and Instrumental Optics*, vol. 25 of *Methods of Experimental Physics*, chap. 2. Geometrical Optics, pp. 7–58, Academic Press, inc., Toronto, 1988.

IPCC, *Climate Change 2001: The Scientific Basis. Contribution of Working Group I to the Third Assessment Report of the Intergovernmental Panel on Climate Change*, Cambridge University Press, Cambridge, UK and New York, NY, USA, 2001.

Jenkins, F. A., and H. E. White, *Fundamentals of Optics*, fourth ed., McGraw-Hill, London, 1976.

Kipp and Zonen, Brewer MkIII Service Manual, 2000.

Lide, D. R. (Ed.), *CRC Handbook of Chemistry and Physics*, 85 ed., CRC Press, New York, 2004.

Liou, K. N., *An Introduction to Atmospheric Radiation*, vol. 84 of *International Geophysics Series*, 2 ed., Academic Press, London, 2002.

Meade Instruments Corporation, Instruction Manual: 10" LX200GPS Schmidt-Cassegrain Telescope, 2003.

Molenti, F., R. Buizza, T. N. Palmer, and T. Petroliagis, The ECMWF ensemble prediction system: Methodology and validation, *Q. J. R. Meteor. Soc.*, *122*, 73–119, 1996.

Ochsenbein, F., P. Bauer, and J. Marcout, The VizieR database of astronomical catalogues, *Astron. Astrophys., Suppl Ser.*, *143*, 23–32, 2000.

Oikarinen, L., *Measurement of Atmospheric Ozone Columns by a Star-Pointing Imaging Spectrometer*, no. 41 in Geophysical Publications, Finnish Meteorological Institute, Helsinki, 1996.

Petelina, S. V., E. J. Llewellyn, N. D. Lloyd, and D. A. Degenstein, Statistical comparisons of Odin/OSIRIS limb-measured stratospheric ozone profiles with satellite and ozonesonde data, in *Proceedings of the Quadrennial Ozone Symposium*, edited by C. S. Zerefos, pp. 496–497, Kos, Greece, 2004.

Raeber, J. A., An automated dobson spectrophotometer, *Pure Appl. Geophys.*, *106*, 947–949, 1973.

Solomon, S., R. R. Garcia, F. S. Rowland, and D. J. Wuebbles, On the depletion of Antarctic ozone, *Nature*, *321*, 755–758, 1986.

United Nations Environment Programme, *Funding situation with regard to ozone-related monitoring activities in developing countries*, Sixth Meeting of the Conference of the Parties to the Vienna Convention for the Protection of the Ozone Layer, 2002.

World Meteorological Organization, *Assessment of Trends in the Vertical Distribution of Ozone*, Global Ozone Research and Monitoring Project - Report No. 43, Geneva, 1998.

World Meteorological Organization, *Scientific Assessment of Ozone Depletion: 2002*, Global Ozone Research and Monitoring Project - Report No. 47, Geneva, 2003.

Zellner, R., *Global Aspects of Atmospheric Chemistry*, vol. 6 of *Topics in Physical Chemistry*, chap. 4, pp. 181–254, Springer, New York, 1999.

Appendix A

Design Drawings

Design drawings used in the manufacture of the prism spectrometer are shown in Figures A.1 to A.6. It should be noted that these are not as-built drawings, as some changes were made to these designs during the manufacture of the instrument.

The aluminum base plate that serves as the optical bench for the spectrometer, including the required bend in the optic axis and the separation of the lens mounts, is shown in Figure A.1. The designed telescope-spectrometer mechanical interface is shown in Figure A.2. A tube and a threaded ring were added to the telescope interface during the manufacturing phase to facilitate the mounting of the spectrometer on the telescope. The required vertical arrangement of the lens mounts is shown in Figure A.3. The positioning of the diagonal prism, which was used to fold the optic axis by 90°, is depicted in Figure A.4. The concept drawing of the counterbalance system is shown in Figre A. The assembly of the instrument is shown in Figure A.6.

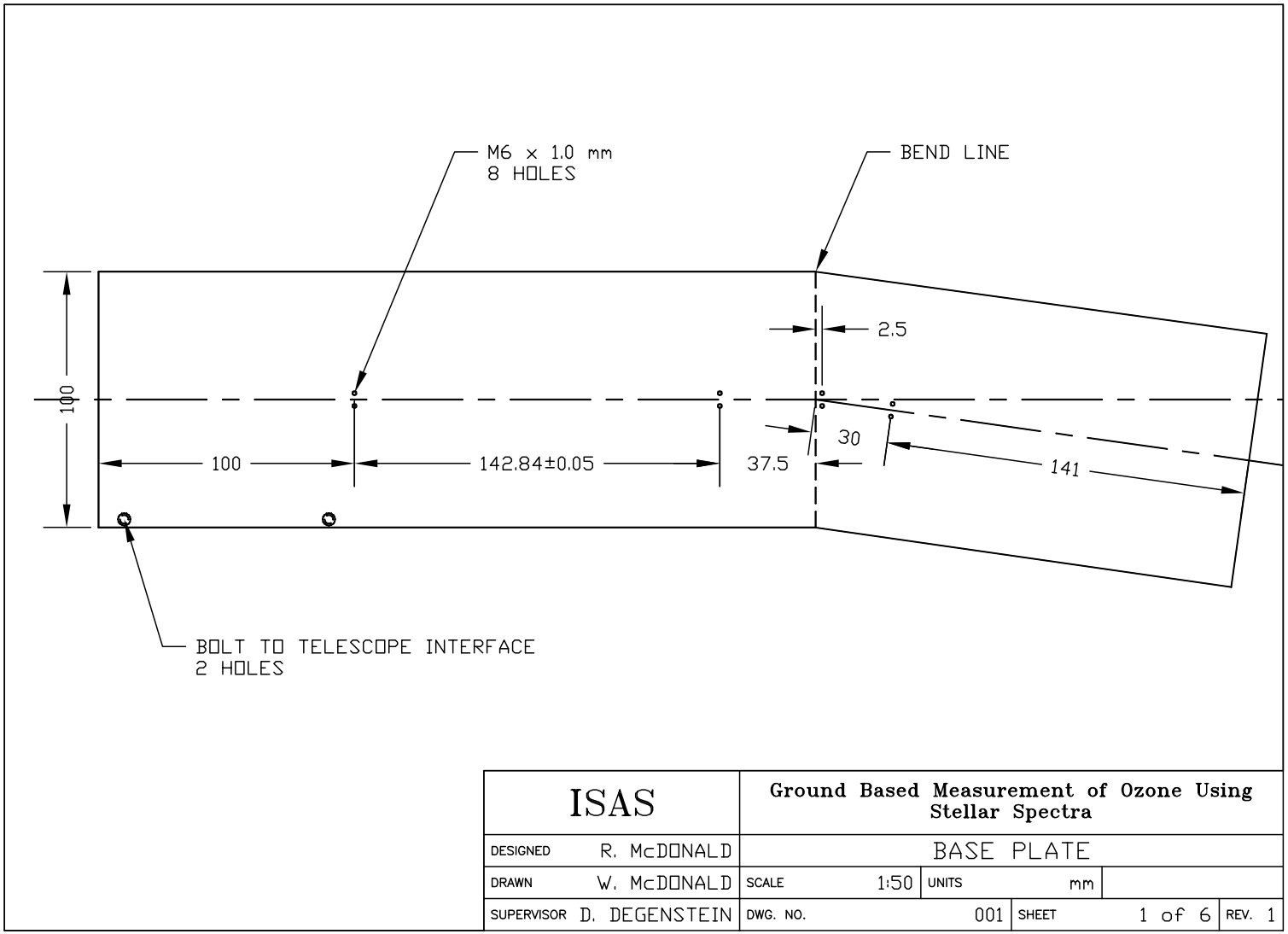
M6 x 1.0 mm
8 HOLES
BEND LINE
2.5
100
100
142.84±0.05
37.5
30
141
BOLT TO TELESCOPE INTERFACE
2 HOLES
ISAS
Ground Based Measurement of Ozone Using Stellar Spectra
DESIGNED R. McDONALD
BASE PLATE
DRAWN W. McDONALD
SCALE 1:50
UNITS mm
SUPERVISOR D. DEGENSTEIN
DWG. NO. 001
SHEET 1 of 6
REV. 1

Figure A.1

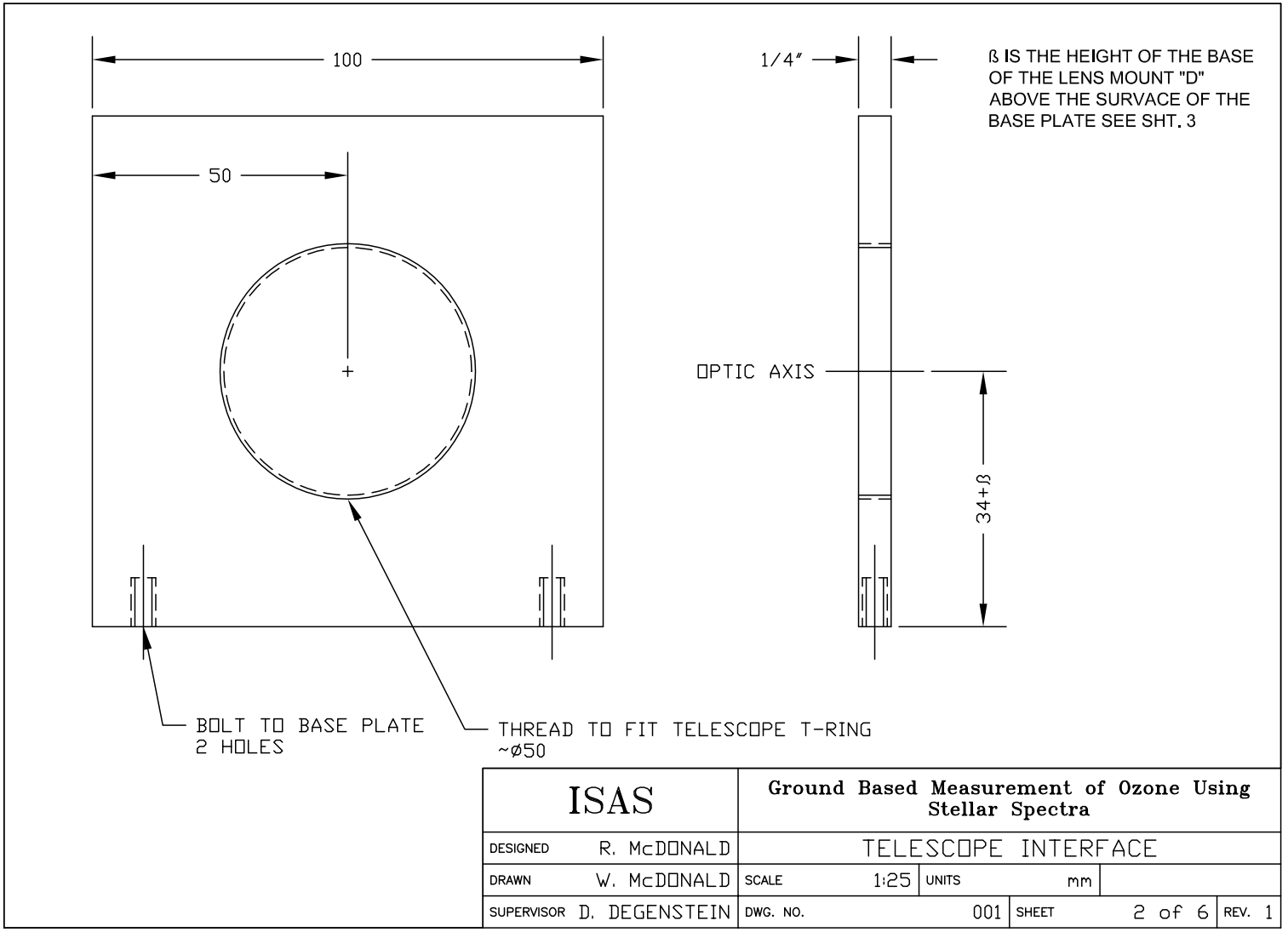
100
50
1/4″
ß IS THE HEIGHT OF THE BASE OF THE LENS MOUNT "D" ABOVE THE SURVACE OF THE BASE PLATE SEE SHT. 3
OPTIC AXIS
34+ß
BOLT TO BASE PLATE
2 HOLES
THREAD TO FIT TELESCOPE T-RING
~ø50
ISAS
Ground Based Measurement of Ozone Using Stellar Spectra
DESIGNED R. McDONALD
TELESCOPE INTERFACE
DRAWN W. McDONALD
SCALE 1:25
UNITS mm
SUPERVISOR D. DEGENSTEIN
DWG. NO. 001
SHEET 2 of 6
REV. 1

Figure A.2

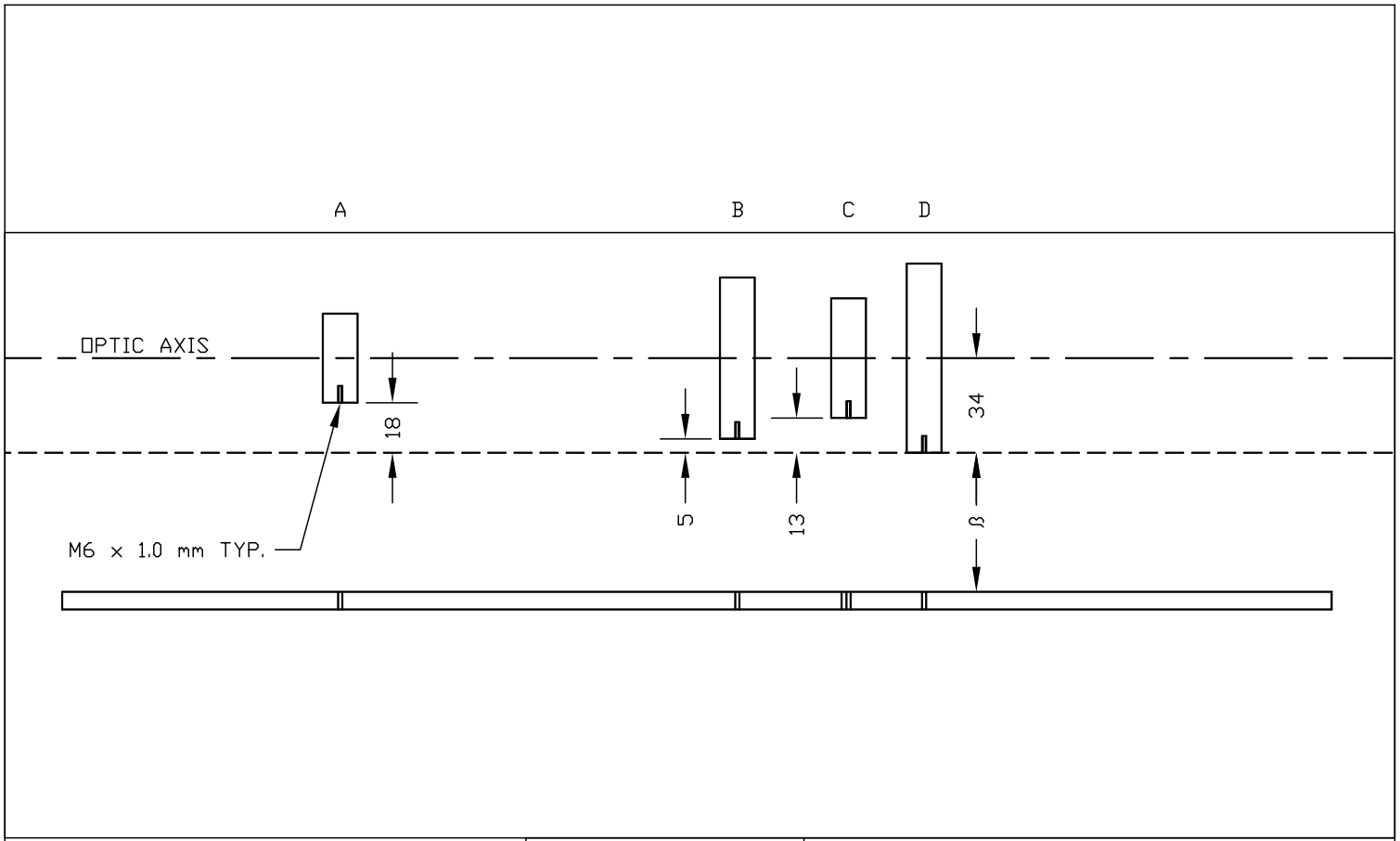

	ISAS	Ground Based Measurement of Ozone Using Stellar Spectra			
	DESIGNED R. McDONALD	LENS MOUNT ARRANGEMENT			
	DRAWN W. McDONALD	SCALE 1:50	UNITS mm		
	SUPERVISOR D. DEGENSTEIN	DWG. NO. 001	SHEET 3 of 6	REV. 1	

Figure A.3

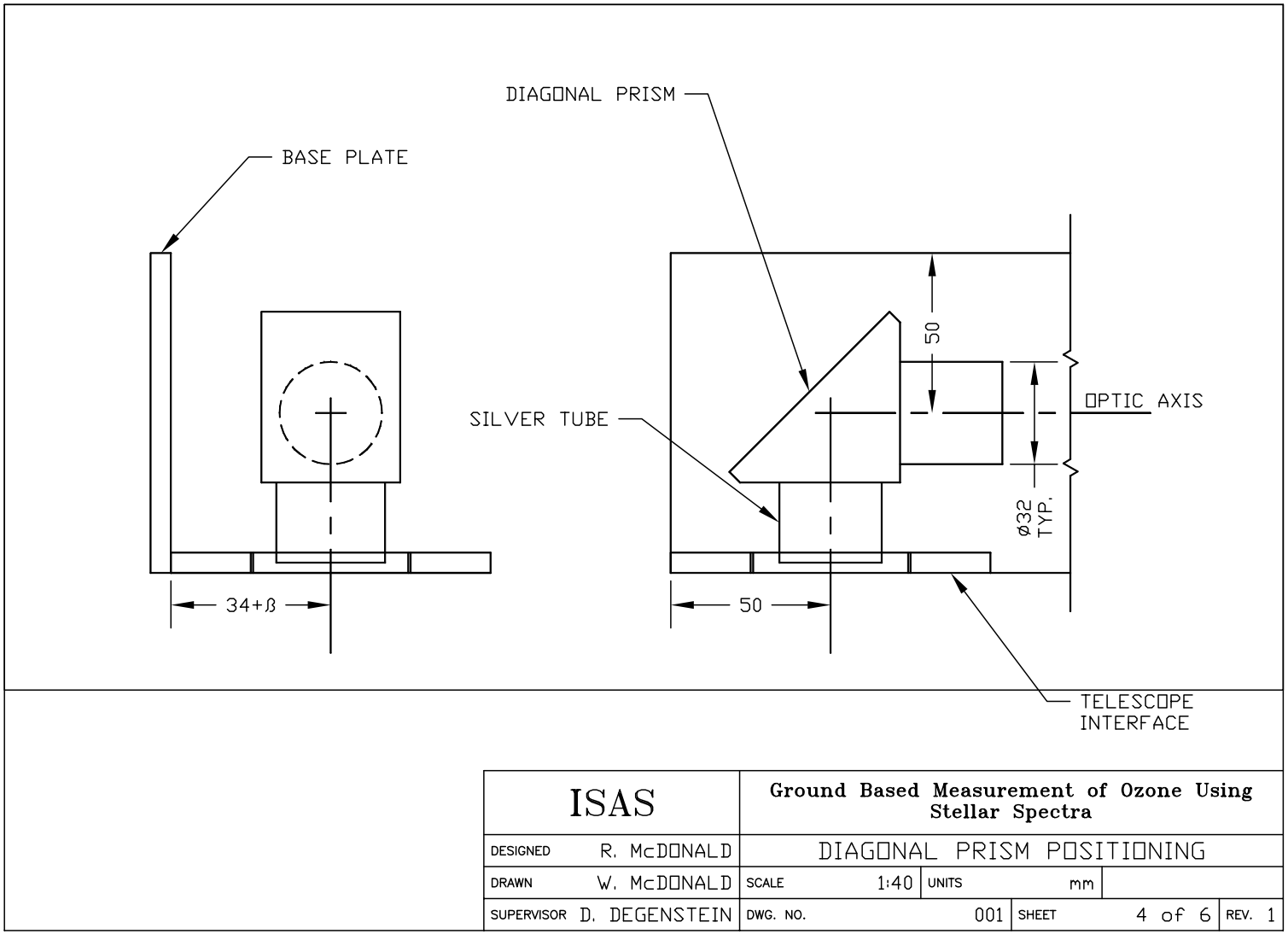

ISAS	Ground Based Measurement of Ozone Using Stellar Spectra			
DESIGNED R. McDONALD	DIAGONAL PRISM POSITIONING			
DRAWN W. McDONALD	SCALE 1:40	UNITS mm		
SUPERVISOR D. DEGENSTEIN	DWG. NO. 001	SHEET 4 of 6	REV. 1	

Figure A.4

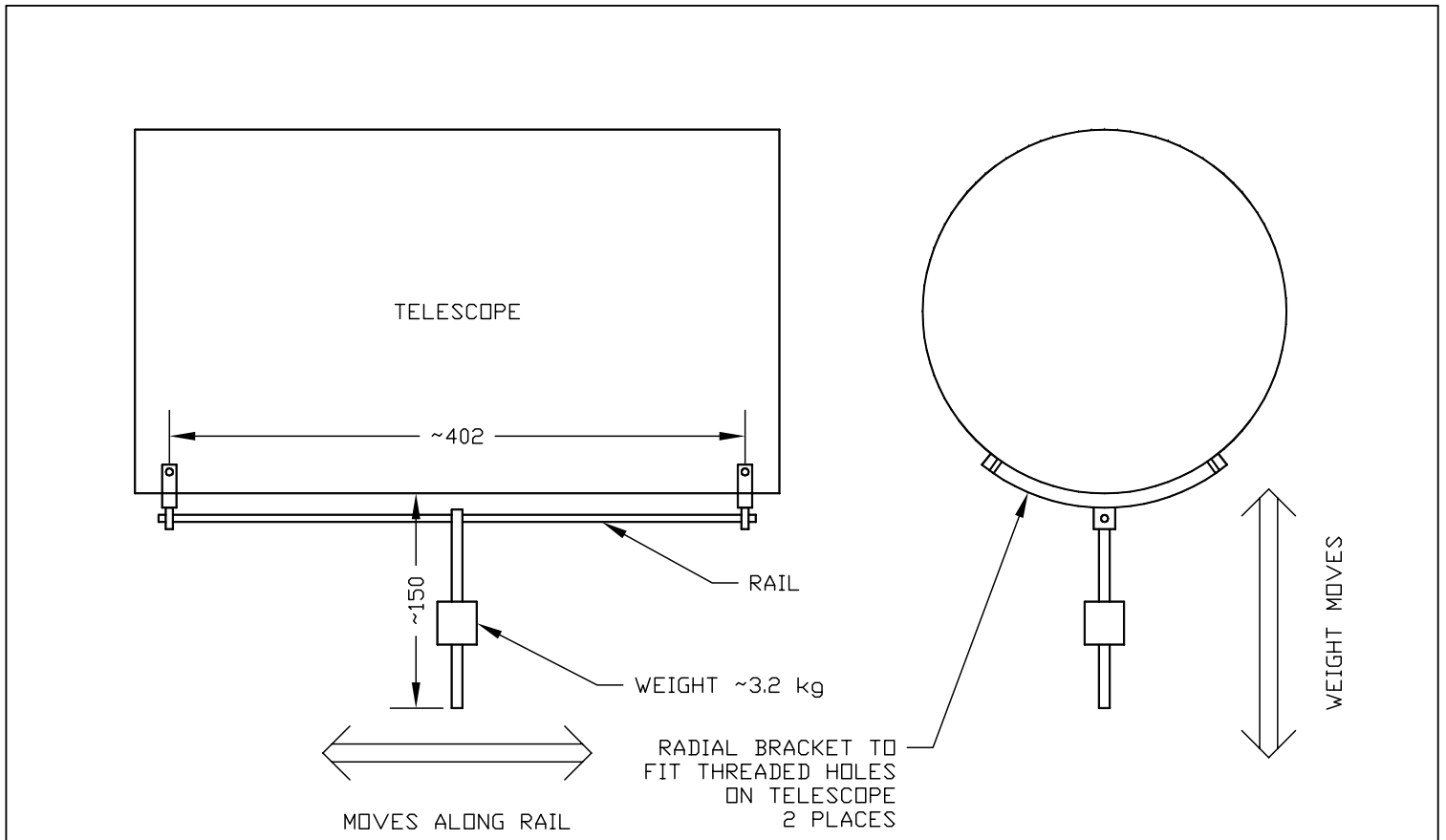

	ISAS	Ground Based Measurement of Ozone Using Stellar Spectra			
	DESIGNED R. McDONALD	COUNTER BALANCE SYSTEM CONCEPT			
	DRAWN W. McDONALD	SCALE NTS	UNITS mm		
	SUPERVISOR D. DEGENSTEIN	DWG. NO. 001	SHEET 5 of 6	REV. 1	

Figure A.5

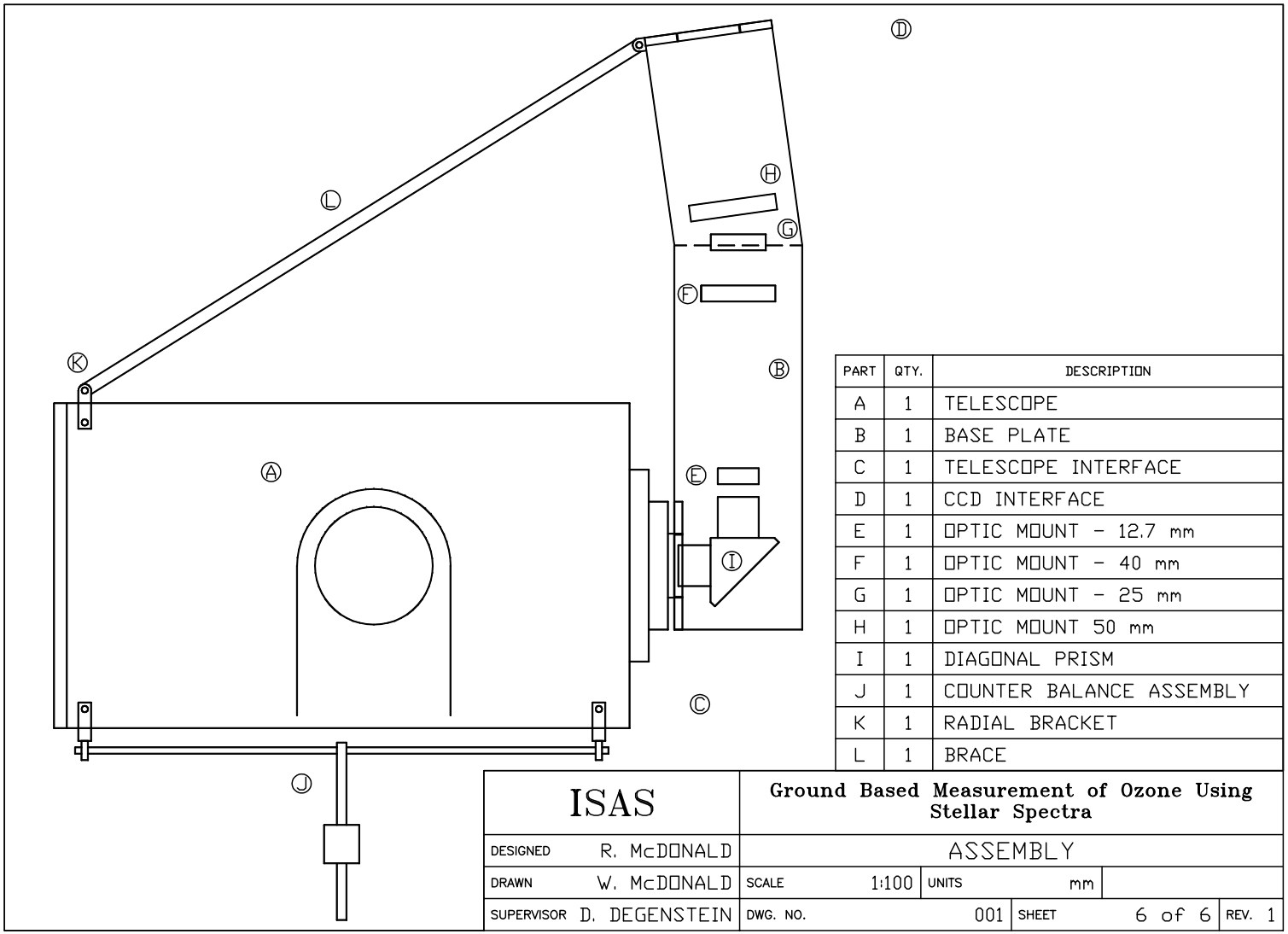

PART	QTY.	DESCRIPTION
A	1	TELESCOPE
B	1	BASE PLATE
C	1	TELESCOPE INTERFACE
D	1	CCD INTERFACE
E	1	OPTIC MOUNT - 12.7 mm
F	1	OPTIC MOUNT - 40 mm
G	1	OPTIC MOUNT - 25 mm
H	1	OPTIC MOUNT 50 mm
I	1	DIAGONAL PRISM
J	1	COUNTER BALANCE ASSEMBLY
K	1	RADIAL BRACKET
L	1	BRACE

ISAS		Ground Based Measurement of Ozone Using Stellar Spectra		
DESIGNED R. McDONALD		ASSEMBLY		
DRAWN W. McDONALD	SCALE 1:100	UNITS mm		
SUPERVISOR D. DEGENSTEIN	DWG. NO. 001	SHEET 6 of 6	REV. 1	

Figure A.6